

I LEVEL

APE 300 622

(12)

DNA 4873F-2

AD A 077621

BOUNDARY LAYER MEASUREMENT PROGRAM

Volume II - Aerodynamic Phenomena Transducer Development

Kaman Sciences Corporation
P.O. Box 7463
Colorado Springs, Colorado 80933

30 June 1978

Final Report for Period 1 August 1975-30 June 1978

CONTRACT No. DNA 001-76-C-0080

DDC FILE COPY

APPROVED FOR PUBLIC RELEASE;
DISTRIBUTION UNLIMITED.

DDC
RECEIVED
DEC 4 1979
A

THIS WORK SPONSORED BY THE DEFENSE NUCLEAR AGENCY
UNDER RDT&E RMSS CODE B342077464 N99QAXAA11206 H2530D.

Prepared for
Director
DEFENSE NUCLEAR AGENCY
Washington, D. C. 20305

79 11 01 003

Destroy this report when it is no longer
needed. Do not return to sender.

PLEASE NOTIFY THE DEFENSE NUCLEAR AGENCY,
ATTN: STTI, WASHINGTON, D.C. 20305, IF
YOUR ADDRESS IS INCORRECT, IF YOU WISH TO
BE DELETED FROM THE DISTRIBUTION LIST, OR
IF THE ADDRESSEE IS NO LONGER EMPLOYED BY
YOUR ORGANIZATION.



UNCLASSIFIED

SECURITY CLASSIFICATION OF THIS PAGE (When Data Entered)

REPORT DOCUMENTATION PAGE		READ INSTRUCTIONS BEFORE COMPLETING FORM
1. REPORT NUMBER DNA 4873F-2	2. GOVT ACCESSION NO.	3. RECIPIENT'S CATALOG NUMBER
4. TITLE (and Subtitle) BOUNDARY LAYER MEASUREMENT PROGRAM, Volume II. Aerodynamic Phenomena Transducer Development.	5. TYPE OF REPORT & PERIOD COVERED Final Report for Period 1 Aug 75-30 Jun 78,	6. PERFORMING ORG. REPORT NUMBER K-79-54(R)-106-2
7. AUTHOR(s) Vernon D. Peckham	8. CONTRACT OR GRANT NUMBER(s) DNA 001-76-C-0080	
9. PERFORMING ORGANIZATION NAME AND ADDRESS Kaman Sciences Corporation P.O. Box 7463 Colorado Springs, Colorado 80933	10. PROGRAM ELEMENT, PROJECT, TASK AREA & WORK UNIT NUMBERS Subtask N99QAXAA112-06	
11. CONTROLLING OFFICE NAME AND ADDRESS Director Defense Nuclear Agency Washington, D.C. 20305	12. REPORT DATE 30 June 1978	
13. MONITORING AGENCY NAME & ADDRESS (if different from Controlling Office) DNA, SEIF	14. NUMBER OF PAGES 144	
15. SECURITY CLASS (of this report) UNCLASSIFIED	16. DECLASSIFICATION/DOWNGRADING SCHEDULE	
17. DISTRIBUTION STATEMENT (of the abstract entered in Block 20, if different from Report) Approved for public release; distribution unlimited.		
18. SUPPLEMENTARY NOTES This work sponsored by the Defense Nuclear Agency under RDT&E RMSS Code B342077464 N99QAXAA11206 H2590D.		
19. KEY WORDS (Continue on reverse side if necessary and identify by block number) Aerodynamic Pressure Measurements Transducer Acoustic Monitor Arc Heater Test		
20. ABSTRACT (Continue on reverse side if necessary and identify by block number) An Aerodynamic Phenomena Transducer was developed to measure simultaneously surface pressure and high frequency pressure fluctuations in the boundary layer of ICBM reentry vehicles. The approach was that of using a plug in the RV heatshield to transmit pressure forces to a capacitively sensed diaphragm transducer in the protected environment behind the heatshield. After devel- opment, the transducer was tested in the AEDC 5 megawatt arc heater facility with good results. Z		

DD FORM 1 JAN 73 1473

EDITION OF 1 NOV 65 IS OBSOLETE

UNCLASSIFIED

SECURITY CLASSIFICATION OF THIS PAGE (When Data Entered)

387 119

45

and Lt. Col. R. Jackson of SAMSO/MNNR, in addition to Mr. Wally Grabowski of the Aerospace Corporation. Each of these individuals contributed significantly to the success of this overall program. The KSC program manager for these efforts was Mr. T. Meagher.

**CONVERSION FACTORS FOR U. S. CUSTOMARY TO METRIC (SI)
UNITS OF MEASUREMENT**

To Convert From	To	Multiply By
angstrom	meters (m)	1.000 000 X E -10
atmosphere (normal)	kilo pascal (kPa)	1.013 25 X E +2
bar	kilo pascal (kPa)	1.000 000 X E +2
barn	meter ² (m ²)	1.000 000 X E -28
British thermal unit (thermochemical)	joule (J)	1.054 350 X E +3
calorie (thermochemical)	joule (J)	4.184 000
cal (thermochemical)/cm ²	mega joule/m ² (MJ/m ²)	4.184 000 X E -2
curie	giga becquerel (GBq)*	3.700 000 X E +1
degree (angle)	radian (rad)	1.745 329 X E -2
degree Fahrenheit	degree kelvin (K)	$T_K = (T_F + 459.67)/1.8$
electron volt	joule (J)	1.602 19 X E -19
erg	joule (J)	1.000 000 X E -7
erg/second	watt (W)	1.000 000 X E -7
foot	meter (m)	3.048 000 X E -1
foot-pound-force	joule (J)	1.355 818
gallon (U.S. liquid)	meter ³ (m ³)	3.785 412 X E -3
inch	meter (m)	2.540 000 X E -2
jerk	joule (J)	1.000 000 X E +9
joule/kilogram (J/kg) (radiation dose absorbed)	Gray (Gy)**	1.000 000
kiloton	terajoules	4.183
kip (1000 lbf)	newton (N)	4.448 222 X E +3
kip/inch ² (ksi)	kilo pascal (kPa)	6.894 757 X E +3
klup	newton-second/m ² (N-s/m ²)	1.000 000 X E +2
micron	meter (m)	1.000 000 X E -6
mil	meter (m)	2.540 000 X E -5
mile (international)	meter (m)	1.609 344 X E +3
ounce	kilogram (kg)	2.834 952 X E -2
pound-force (lbf avoirdupois)	newton (N)	4.448 222
pound-force inch	newton-meter (N-m)	1.129 848 X E -1
pound-force/inch	newton/meter (N/m)	1.751 268 X E +2
pound-force/foot ²	kilo pascal (kPa)	4.788 026 X E -2
pound-force/inch ² (psi)	kilo pascal (kPa)	6.894 757
pound-mass (lbm avoirdupois)	kilogram (kg)	4.535 924 X E -1
pound-mass-foot ² (moment of inertia)	kilogram-meter ² (kg-m ²)	4.214 011 X E -2
pound-mass/foot ³	kilogram/meter ³ (kg/m ³)	1.601 846 X E +1
rad (radiation dose absorbed)	Gray (Gy)**	1.000 000 X E -2
roentgen	coulomb/kilogram (C/kg)	2.579 760 X E -4
shake	second (s)	1.000 000 X E -8
slug	kilogram (kg)	1.459 390 X E +1
torr (mm Hg, 0° C)	kilo pascal (kPa)	1.333 22 X E -1

*The becquerel (Bq) is the SI unit of radioactivity; 1 Bq = 1 event/s.

**The Gray (Gy) is the SI unit of absorbed radiation.

A more complete listing of conversions may be found in "Metric Practice Guide 2 380-74," American Society for Testing and Materials.

TABLE OF CONTENTS

	<u>Page No.</u>
1.0 INTRODUCTION	11
2.0 APT DEVELOPMENT	13
2.1 Background	13
2.2 Transducer Development	17
2.2.1 Concept Phase	17
2.2.2 APT Development	21
2.2.3 Circuit Design	26
3.0 ARC HEATER TEST	31
3.1 Test Planning	31
3.2 Test Hardware Design	35
3.2.1 Sample Block Layout	35
3.2.2 Thermal Sensor Designs	41
3.3 Test Results	45
3.3.1 Summary	45
3.3.2 Test Run No. 1 Data	50
3.3.3 Test Run No. 2 Data	64
3.3.4 Test Run No. 3 Data	74
3.4 Discussion of Arc Heater Test Results	84
4.0 SUMMARY AND CONCLUSIONS	87
REFERENCES	89
Appendix A - Force Analysis on APT Plug/ Diaphragm	91
Appendix B - Analysis of the APT Sensor Circuit	97
Appendix C - Flight Reentry Heating and Ablation	99

TABLE OF CONTENTS (CONT'D)

	<u>Page No.</u>
Appendix D - Test Run 1 Photographs	105
Appendix E - Test Run 2 Photographs	121
Appendix F - Test Run 3 Photographs	129

LIST OF ILLUSTRATIONS

	<u>Page No.</u>
FIGURE 1 Transducer Concept	14
FIGURE 2 Transducer Cross Section	18
FIGURE 3 Capacitance Sensor	20
FIGURE 4 Redesigned APT Configuration	22
FIGURE 5 APT Development Model	23
FIGURE 6 APT Cutaway Drawing	24
FIGURE 7 APT Circuit Block Diagram	28
FIGURE 8 APT Sensor Circuit	29
FIGURE 9 Mach 2 Arc Heater Conditions	32
FIGURE 10 Pressure Prediction	36
FIGURE 11 Test Block Interior Layout	37
FIGURE 12 Calibration Block Interior Layout	38
FIGURE 13 Typical Test Block Assembly	39
FIGURE 14 Typical Calibration Block Assembly	40
FIGURE 15 Insulated Test Sample	42
FIGURE 16 Copper Calorimeter	43
FIGURE 17 Predicted Calorimeter Output	44
FIGURE 18 Predicted Temperature History	46
FIGURE 19 Test Run 1 Calibration Data-Thermal	52
FIGURE 20 Test Run 1 Calibration Data-Thermal	53
FIGURE 21 Test Run 1 Calibration Data Pressure	55
FIGURE 22 Test Run 1 Calibration Data Pressure	56
FIGURE 23 Test Run 1 APT Data	57

LIST OF ILLUSTRATIONS (CONT'D)

	<u>Page No.</u>
FIGURE 24 Test Run 1 APT Data	58
FIGURE 25 Test Run 1 APT Data	59
FIGURE 26 Test Run 1 APT Data	60
FIGURE 27 Test Run 1 APT Data	61
FIGURE 28 Test Run 2 Calibration Data-Thermal	65
FIGURE 29 Test Run 2 Calibration Data-Thermal	66
FIGURE 30 Test Run 2 Calibration Data-Pressure	67
FIGURE 31 Test Run 2 Calibration Data-Pressure	68
FIGURE 32 Test Run 2 APT Data	70
FIGURE 33 Test Run 2 APT Data	71
FIGURE 34 Test Run 2 APT Data	72
FIGURE 35 Test Run 3 Calibration Data-Thermal	75
FIGURE 36 Test Run 3 Calibration Data-Thermal	76
FIGURE 37 Test Run 3 Calibration Data-Pressure	78
FIGURE 38 Test Run 3 Calibration Data-Pressure	79
FIGURE 39 Test Run 3 APT Data	80
FIGURE 40 Test Run 3 APT Data	81
FIGURE 41 Test Run 3 APT Data	82
FIGURE 42 Diaphragm Analysis Diagram	91
FIGURE 43 Diaphragm Flexure	92
FIGURE 44 Pressure Distribution	93
FIGURE 45 Constant K_p for Center Post Load	94
FIGURE 46 Constant K_D for Uniform Loading-Center Post Diaphragm	95

LIST OF ILLUSTRATIONS (CONT'D)

	<u>Page No.</u>
FIGURE 47 Total Ablation - 4 Trajectories	100
FIGURE 48 Char Depth	101
FIGURE 49 Peak Heating Rate	102
FIGURE 50 Total Heat	103
FIGURE 51 Test Run 1, Pre-Test Installation	106
FIGURE 52 Test Run 1, Pre-Test Sting 2	107
FIGURE 53 Test Run 1, Pre-Test Sting 3	108
FIGURE 54 Test Run 1, Pre-Test Sting 4	109
FIGURE 55 Test Run 1, Pre-Test Sting 5	110
FIGURE 56 Test Run 1, Pre-Test Sting 6	111
FIGURE 57 Test Run 1, Pre-Test Sting 7	112
FIGURE 58 Test Run 1, Post-Test Nozzle	113
FIGURE 59 Test Run 1, Post-Test Model Damage	114
FIGURE 60 Test Run 1, Post-Test Sting 2	115
FIGURE 61 Test Run 1, Post-Test Sting 3	116
FIGURE 62 Test Run 1, Post-Test Sting 4	117
FIGURE 63 Test Run 1, Post-Test Sting 5	118
FIGURE 64 Test Run 1, Post-Test Sting 6	119
FIGURE 65 Test Run 1, Post-Test Sting 7	120
FIGURE 66 Test Run 2, Sting 1 Negative Photo	122
FIGURE 67 Test Run 2, Sting 2 Negative Photo	123
FIGURE 68 Test Run 2, Sting 3 Negative Photo	124
FIGURE 69 Test Run 2, Sting 4 Negative Photo	125
FIGURE 70 Test Run 2, Sting 5 Negative Photo	126

LIST OF ILLUSTRATIONS (CONT'D)

	<u>Page No.</u>
FIGURE 71 Test Run 2, Post-Test Models	127
FIGURE 72 Test Run 2, Post-Test Model	128
FIGURE 73 Test Run 3, Sting 1 Negative Photo	130
FIGURE 74 Test Run 3, Sting 2 Negative Photo	131
FIGURE 75 Test Run 3, Sting 3 Negative Photo	132
FIGURE 76 Test Run 3, Sting 4 Negative Photo	133
FIGURE 77 Test Run 3, Sting 5 Negative Photo	134
FIGURE 78 Test Run 3, Post-Test Model 1	135
FIGURE 79 Test Run 3, Post-Test Model 2	136
FIGURE 80 Test Run 3, Post-Test Model 3	137

LIST OF TABLES

		<u>Page No.</u>
TABLE 1	APT Program - Development Goals	16
TABLE 2	APT Arc Heater Test	34
TABLE 3	Arc Heater Run Parameters	47
TABLE 4	Model Configurations	49
TABLE 5	Test Sequences	51
TABLE 6	Arc Heater Test - Simulation Comparison	85

SECTION 1.0

INTRODUCTION

The Aerodynamic Phenomena Transducer (APT) program had the primary objective of developing a transducer capable of measuring surface pressure on an ICBM reentry vehicle heatshield. Such a transducer could provide important data on wall pressure components during boundary layer transition on vehicles reentering the atmosphere. Prior techniques for flight measurements of surface pressure, both static and fluctuating components, utilized ports through the heatshield. Ports are known to cause errors due to uneven ablation or flow-responsive resonance phenomena, thus a technique was sought to obviate these errors. The approach proposed was that of transmitting surface pressure to a transducer through a small diameter heatshield plug which was separated by a small gap from the heatshield. The plug-to-gap area ratio if large, should in concept reduce errors due to flow perturbations around the plug edges. The thin gap is filled with a material with low shear strength which insulates the internal parts of the gage.

The AP transducer also includes an acoustic monitor measurement to high frequency pressure fluctuations generated by the turbulent boundary layer on the plug surface. To accomplish this measurement, a piezoelectric sensor is imbedded in the transducer on the rear surface of the plug.

The dual sensing concept of the APT permits a wider range of boundary layer pressure parameters to be measured than heretofore possible. The plug-force sensor responds to static pressure and fluctuations to approximately 5 kHz, while the acoustic monitor is responsive from 2 to over 300 kHz.

In addition to transducer and electronics development, a test was designed in which the APT was to undergo an exposure to a high temperature reentry environment simulation. The test was accomplished in the 5 Megawatt arc heater facility at AEDC, Tullahoma, Tennessee.

This report summarizes the contract effort, including the APT design, the development of the associated signal conditioning electronics and includes also details and results of the 5 MW arc heater test.

SECTION 2.0

APT DEVELOPMENT

2.1 BACKGROUND

The results of a preceding study¹ included the fact that asymmetric boundary layer transition on reentry vehicles caused incremental velocities lateral to the trajectory and sizable target miss distances. In this same study, it was noted that the basic force mechanism to which the RV reacted was differential pressures on the heatshield which were induced during transition.

A corollary literature survey for boundary layer measurement techniques was also included in the study. A primary result of this survey was that all boundary layer pressure measurements heretofore utilized techniques which displayed a mutual interference with the flow. For example, small pressure transducers mounted behind the heatshield were connected to the flow with a small port. This port reacted dynamically with the flow and resulting pressure readings were erratic. Additionally, the hole perturbed the surface flow and a higher rate of ablation was observed at its edge. Surface mounted transducers were not used for flight test measurements because of the extreme heat environment during transition, but were applied successfully in milder wind tunnel tests.

Because of the noticeable lack of an accurate measurement technique, the development of the Aerodynamic Phenomena Transducer (APT) was proposed. The APT was to be developed as a multi-purpose transducer which measured both static pressure with slow variations and boundary layer transition with high frequency (>100 kHz) pressure fluctuation. The original proposed concept is illustrated in Figure 1.

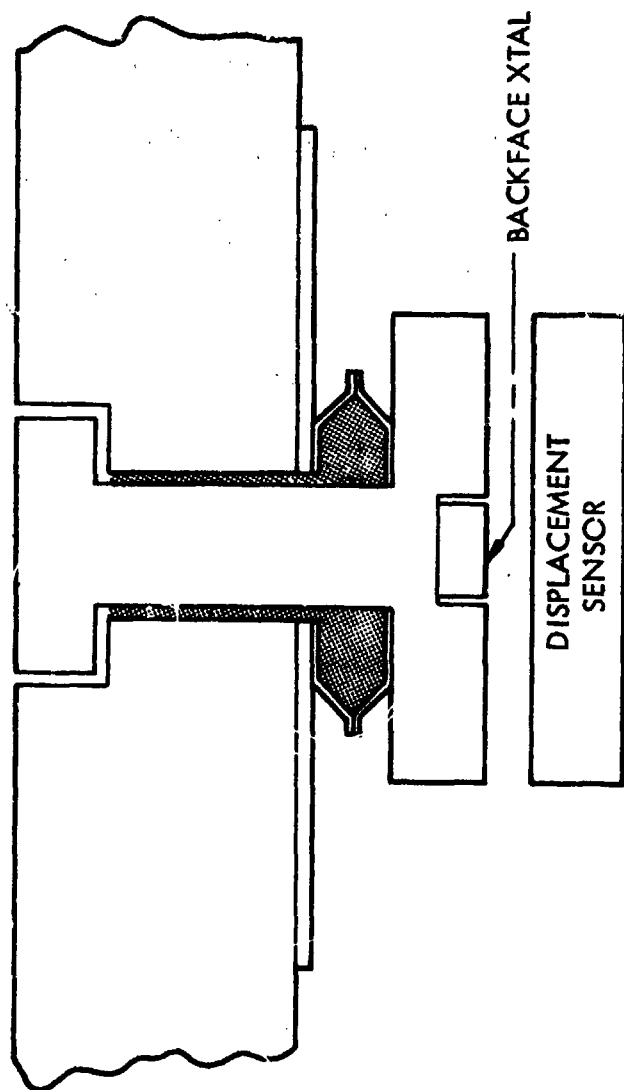


FIGURE 1 TRANSDUCER CONCEPT

As illustrated, static pressure on the heatshield surface is transmitted through a plug causing displacement of a spring which is measured by a displacement sensor, either capacitive or inductive. The plug is made of the heatshield material to provide thermal protection. The gap around the plug is narrow to minimize ablation around the edges and to reduce hot gas flow to the interior. The plug concept, while not free of flow field disturbances, minimizes them and provides an accurate pressure measurement due to the large averaging area of the plug on the surface; i.e., flow field eddies average across the plug surface.

Acoustic noise is monitored by a crystal mounted at the base of the plug; the crystal output is proportional to high frequency surface noise conducted by the plug. The surface acoustic noise has been shown to be an excellent indicator of the presence of turbulence on reentry vehicles².

Development goals for the transducer are listed in Table 1. These goals are based on a typical reentry vehicle application with maximum static pressure of $7 \times 10^4 \text{ N/m}^2$ occurring at the altitude of peak dynamic pressure. The very small resolution of 350 N/m^2 is required because the wall pressure change at transition is of this magnitude. The compensation for steady acceleration reduces errors due to RV spin which imposes a constant force on a plug and hence the transducer diaphragm. At 10 revolutions per second, a transducer mounted on the heatshield at a radius of 15 cm, experiences a constant acceleration of approximately 60 g's. Additional goals listed in Table I are those normally associated with pressure measurement.

Details of the gage development and results are given in following sections.

TABLE 1 APT PROGRAM - DEVELOPMENT GOALS

STATIC PRESSURE

2 to 4 ATM Full Scale
.0034 ATM Resolution
.2% F.S./°C Static Temperature Drift
2% F.S. Transient Temperature Drift
Operational Temperature Range (Ref. Cavity)
0 to 100°C
1.27 cm Plug Dia./2.54 cm Maximum Diameter
Compensated Acceleration Response
Calibratable in Absolute Units
0 to 1000 Hz Bandwidth

ACOUSTIC PRESSURE

Resonant Acoustic Monitor
.17 to .34 ATM Full Scale
 7×10^{-5} ATM Resolution
Operational Temperature Range 0 to 100°C
Co-Located with Static Gage

2.2 TRANSDUCER DEVELOPMENT

2.2.1 Concept Phase

During this part of the contract work, two techniques were considered for transmitting force from the surface to a sensor with a minimum of error and flow field interference. The two methods included a force transmitting plug with strain gage sensor and a plug mounted as an integral part of a capacitively sensed diaphragm. Experimental models of both types were design, fabricated and tested.

The strain gage type APT transducer was constructed as shown in Figure 2. In this configuration the strain gages respond to the static pressure, and the crystal responds to the high frequency acoustic signal. To obtain adequate sensitivity without resorting to a thin, fragile inner cylinder, semiconductor strain gages were used. Four strain gages were used - two mounted axially and two circumferentially. The use of these four gages, when connected to a bridge completion network, provided temperature compensation and insensitivity to sideward forces. The void within the transducer was to be evacuated to avoid a temperature coefficient due to changes in air pressure with temperature.

Although the transducer performed its function very well, much difficulty was encountered in obtaining temperature compensation. Since the four strain gages had unequal temperature coefficients and sensitivities, a complex bridge completion network was used to null the temperature effects as well as to obtain dc balance. The resulting output versus temperature was a nonlinear curve which could be corrected for any two specific temperatures but at no other temperatures. It was felt that this nonlinearity could be corrected with a more complex network using nonlinear elements. The complexity of the system is also doubled by the need for acceleration cancellation. This cancellation would be

STRAIN GAGE APT TRANSDUCER

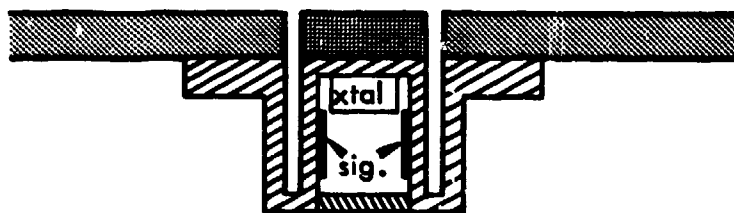


FIGURE 2 TRANSDUCER CROSS SECTION

accomplished by the addition of another section to the rear of the transducer which would serve only as an accelerometer. The two sections would require independent temperature compensation because of the front-to-back temperature gradient within the transducer. Another correction that is required in this design is to null the response of the transducer to static pressure within the annular slot. This correction can be accomplished varying the geometry at the expense of more difficult fabrication.

In the light of the above mentioned complications, the strain gage type transducer was tabled while the diaphragm and capacitive electrode design was investigated. An interior concept drawing of the capacitive sensor is shown in Figure 3, illustrating the principle. The exterior housing material is stainless steel or other metal and the plug is made from the heatshield material of the RV on which it is to be installed. With careful dimensioning, the top of the plug is flush with the exterior heatshield surface after installation. The APT is designed to be an absolute gage; that is, all air is evacuated from the interior of the transducer so that the reference force on the diaphragm is not a variable due to temperature.

In an installation, the mounting flange is sealed to the back surface of the heatshield so that boundary layer pressure does not penetrate interior spaces. Pressure on the plug and diaphragm cause the diaphragm to deflect inward and closer to the capacitance elements on the circuit board resulting in an output proportional to the applied pressure.

A design force analysis of the APT plug and diaphragm was completed and has been included in this report as Appendix A. An interesting feature of the APT plug geometry revealed by the analysis is that with proper dimensioning, pressure in the gap region produces no output from the transducer.

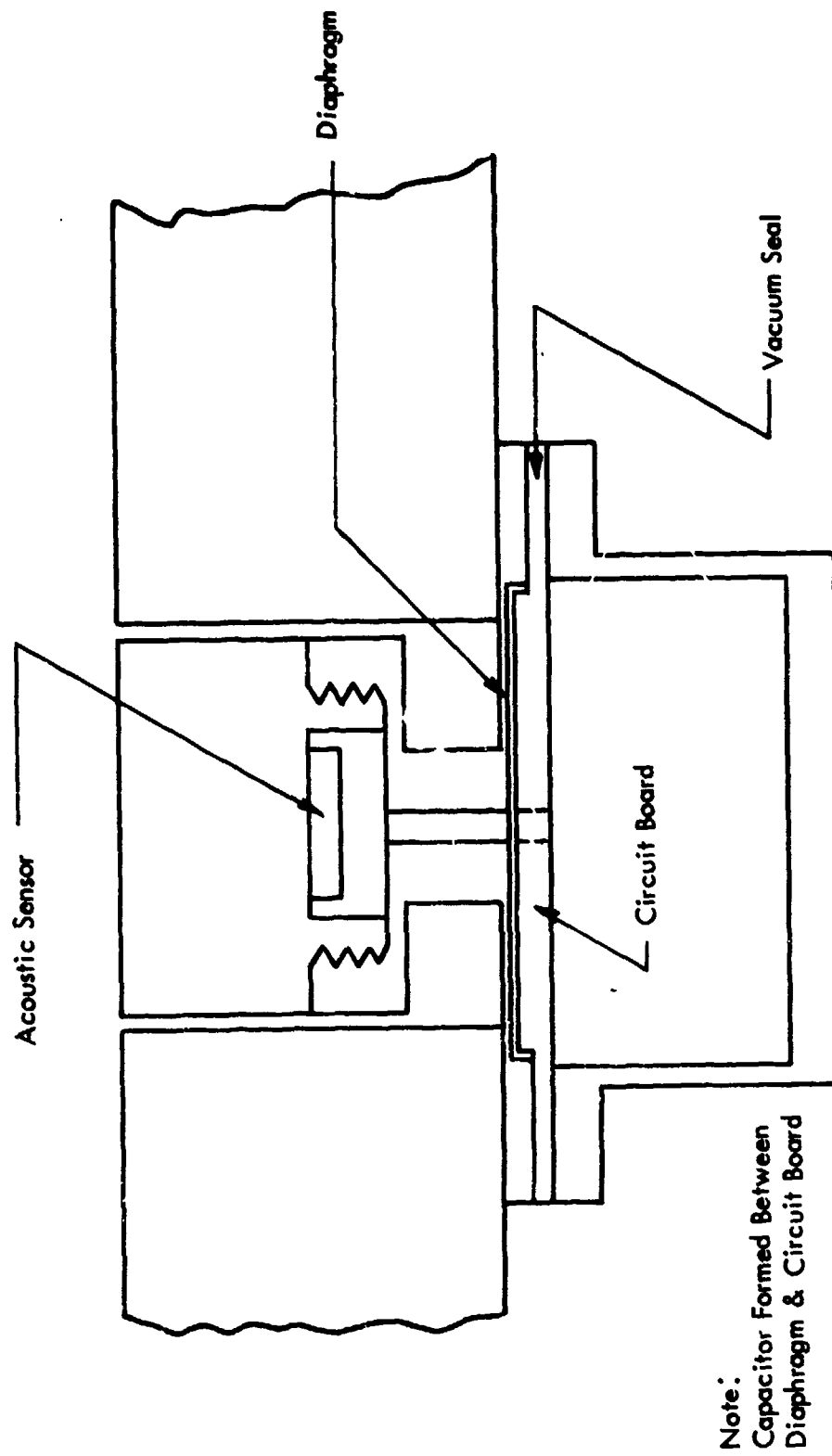


FIGURE 3 CAPACITANCE SENSOR

Several models were made from aluminum to test the feasibility of the concept. Early test results showed there to be a temperature drift problem with different thermal coefficients of expansion between the printed circuit board and the aluminum case. This resulted in a redesign of the interior mounting technique shown in Figure 4 where the p.c. board was held by a center post which in turn was bonded to an aluminum disk. This disk was part of the mounting flange sandwich. Satisfactory performance of this design with respect to temperature drift was obtained since it exhibited a temperature coefficient less than 0.07% F.S./°C. A photograph of the aluminum concept transducer is shown in Figure 5.

Based on temperature coefficient and ease of construction the capacitive transducer was chosen for additional development.

2.2.2 APT Development

Having selected a concept, work proceeded to design the transducer to be used in an arc heater test (reference Section 3.3). Design features included the following:

- Full Scale Pressure - 6.9×10^5 N/m²
- Plug Diameter - 1.27 cm
- Case Diameter - 2.54 cm
- Stainless Steel Case
- Laser Welding
- Vacuum Reference

Due to the higher pressure expected in the arc heater test, a fairly thick diaphragm (.038 cm) was used and the diaphragm-capacitor spacing was 0.0102 cm. Other critical dimensions of the final APT design are shown in the cutaway assembly drawing in Figure 6. The measured temperature drift of this model from room temperature to 71°C is .1% F.S./°C.

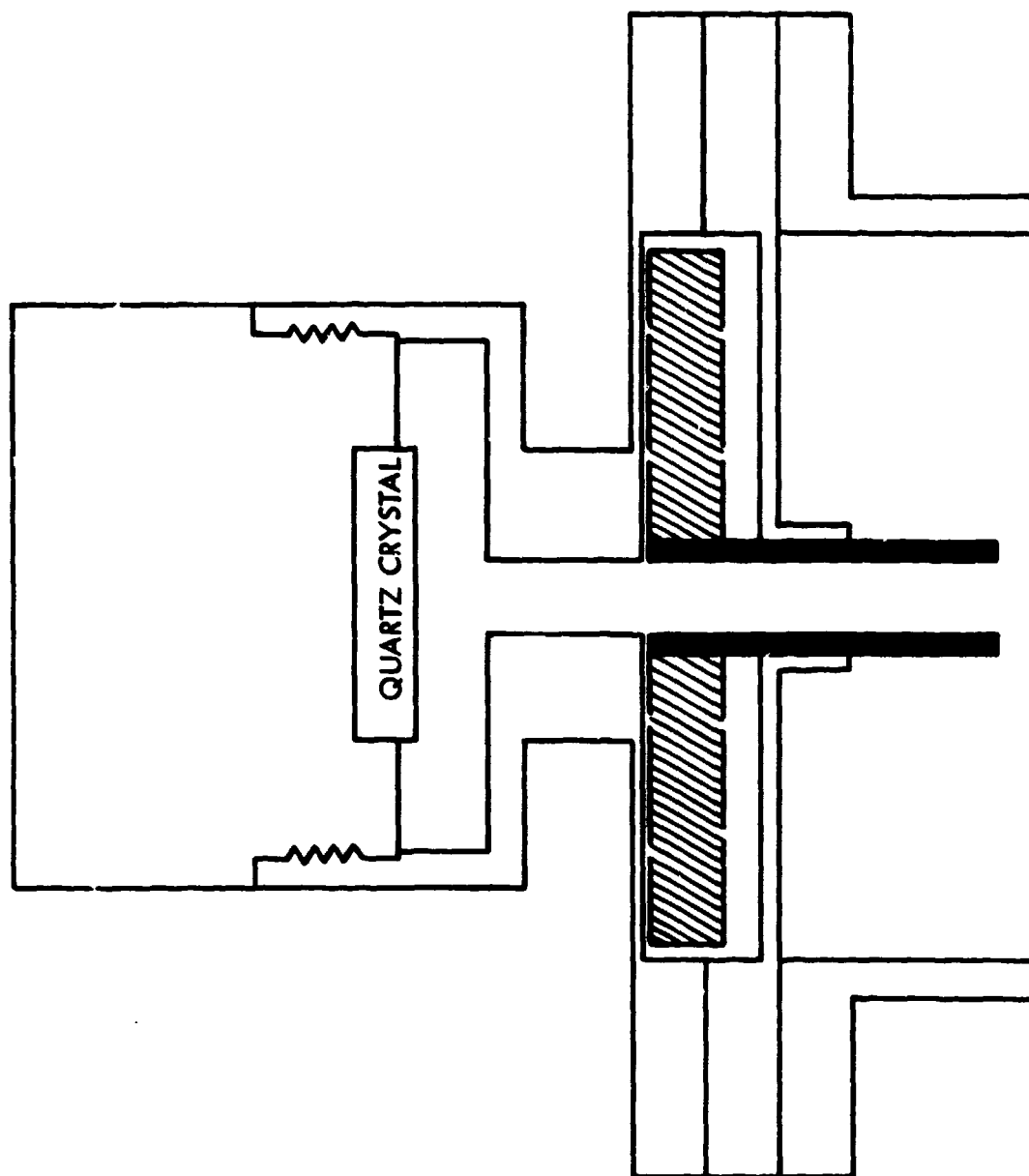


FIGURE 4 REDESIGNED APT CONFIGURATION



FIGURE 5 APT DEVELOPMENT MODEL

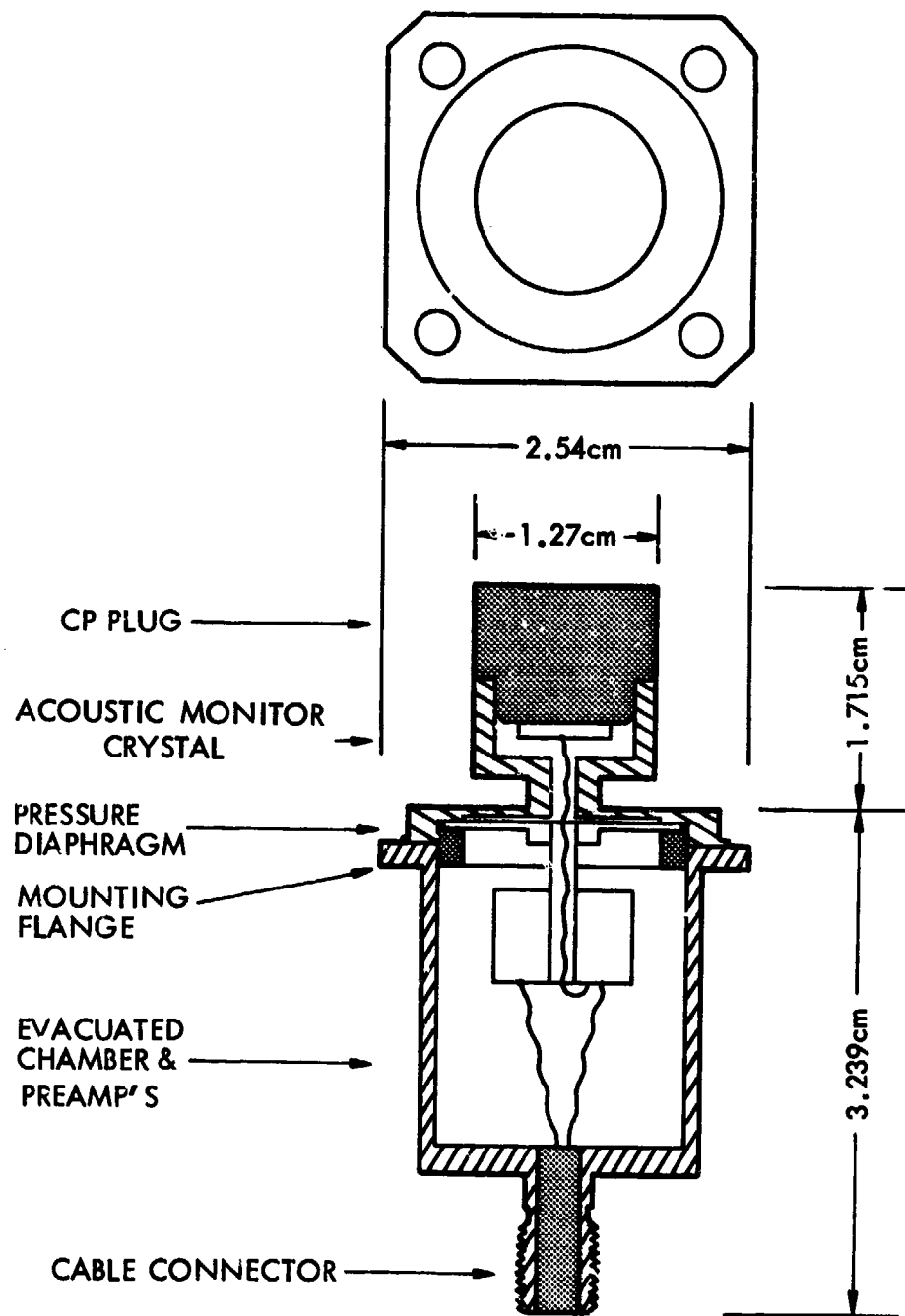


FIGURE 6 APT CUTAWAY DRAWING

Compensation for radial acceleration forces was included in the design via the circuit board acting as a diaphragm. Components are mounted on the p.c. board central area to increase the mass which causes the board to deflect when subjected to linear acceleration. The board thickness is selected to provide the same deflection as the pressure diaphragm when accelerated, thus obtaining a primary compensation for the potential error caused by acceleration. (Refer to Figure 6 for physical layout.)

Some difficulties were experienced in finding a stainless steel alloy which is both machinable and weldable with the laser. The more common stainless steel alloys 303 and 304 were used initially but both lacked either in machinability or weldability. After some experimentation the alloy 15-5PH was procured; satisfactory results were obtained. This alloy also has a lower temperature coefficient of expansion, reducing the temperature drift of the transducer.

The assembly procedure for the transducer includes the following steps:

- 1) Collect and clean all component parts.
- 2) Bond the BLAM crystal to the heatshield plug and attach wires to the crystal.
- 3) Assemble the plug to the diaphragm top, sealing thread joints. Seal cavity behind BLAM crystal.
- 4) Assemble in-sensor circuit components to circuit board diaphragm.
- 5) Bond the circuit board and retaining ring in place on the pressure diaphragm.
- 6) Assemble connector to housing and seal.
- 7) Wire connector to circuit board assembly.

- 8) Clamp housing in place and laser weld seam.
- 9) Place APT in welding vacuum fixture and laser weld evacuation hole.

2.2.3 Circuit Design

The circuit block diagram in Figure 7 is the signal conditioner which supplies drive power to the sensor and amplifies the signal which returns from the sensor carrying pressure information. The circuit consists of an amplitude stabilized FET linear oscillator. The oscillator output drives the bridge in the sensor through a connecting cable. Amplitude stabilization is achieved by gain control feedback to the input FET.

The frequency of oscillation is 5 MHz, at which frequency bridge components have approximately 3000 ohms reactive impedance.

The cable between the sensor and signal conditioner in addition to providing drive power, also conducts the direct current return signal to an amplifier. A single integrated circuit amplifier provides sufficient gain to drive a high level telemetry system. An offset control has also been provided to adjust the output to allow for negative swing if necessary.

Sensor bridge circuitry is shown in Figure 8. This is a relatively uncomplicated circuit in which the drive voltage is common to both sides of the bridge at the juncture of C_1 , C_2 , R_1 and R_2 . The drive voltage is divided between C_1 and the active diaphragm capacitance C_c and current is drawn through D_1

on the positive cycles sufficient to change C_c and C_1 to approximately one-half the drive voltage less the diode threshold of 0.6 volts. A similar situation exists on the other side of the bridge between C_2 and C_o except that the diode is reversed causing the current to flow in diode D_2 on negative half cycles.

A negative average dc voltage appears on C_c and a positive average dc voltage on C_o which cause current to flow through resistors R_1 and R_2 respectively toward the common summing junction. An analysis of the amplitude of the dc voltage at the cable and the sensitivity to diaphragm deflection is presented in Appendix B.

Having the results from Appendix B, the output from the APT designed for the arc heater test, for a $6.9 \times 10^4 \text{ N/m}^2$ pressure differential, may be calculated from

$$dv_s = \frac{E_D}{2} \frac{C_1 dC_c}{(C_c + C_s + C_1)^2} = .093 dC_c$$

E_D = peak bridge drive voltage = 9v

C_1 = 10 picofurads (pf)

C_c = 10 picofurads (pf)

C_s = 2 picofurads (pf)

The deflection of the diaphragm center for $6.9 \times 10^4 \text{ N/m}^2$ pressure is $2.08 \times 10^{-4} \text{ cm}$ while the initial spacing is .01016 cm, giving a relative capacitance change of approximately 1.96%. The change

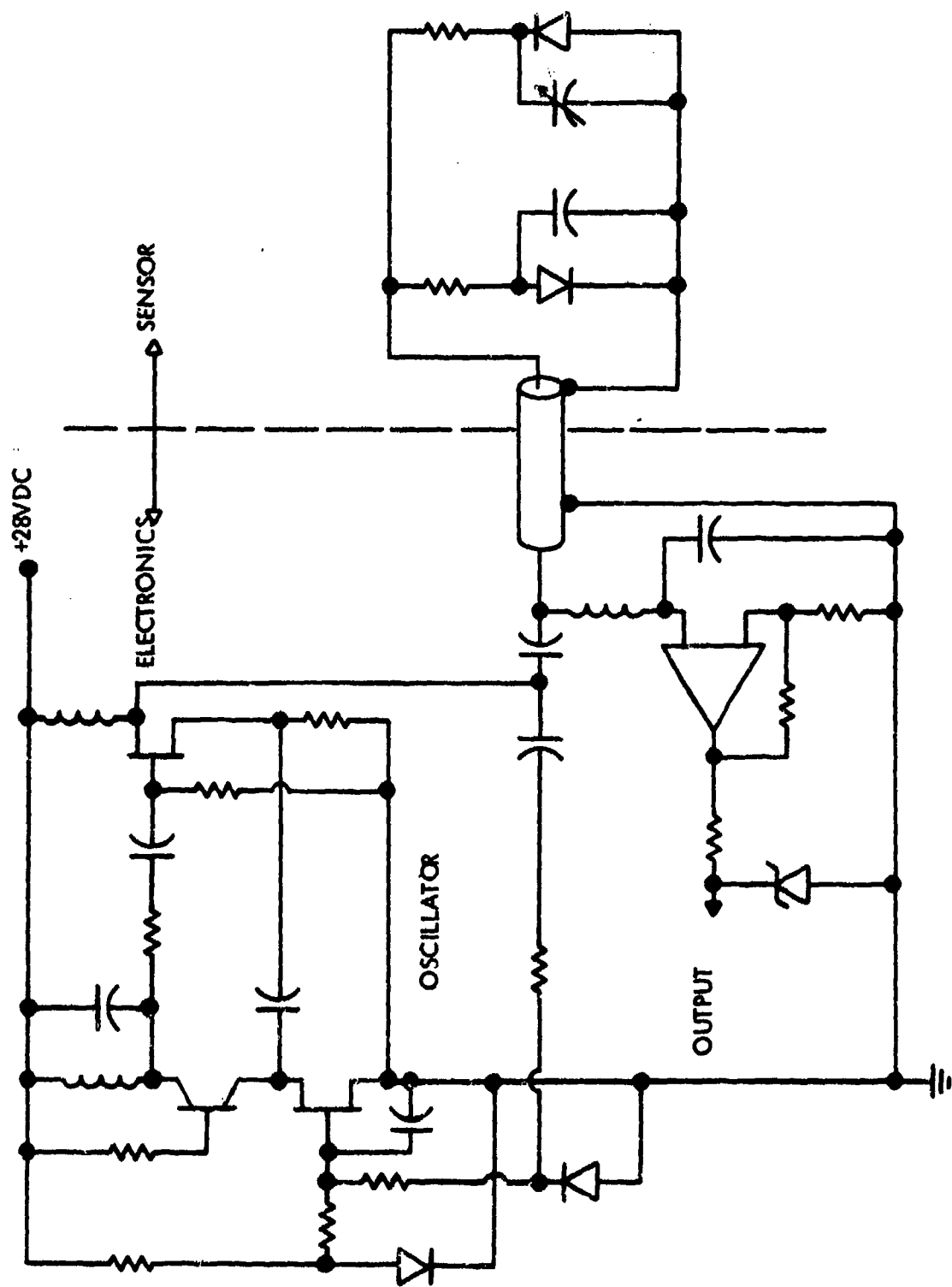


FIGURE 7 APT CIRCUIT BLOCK DIAGRAM

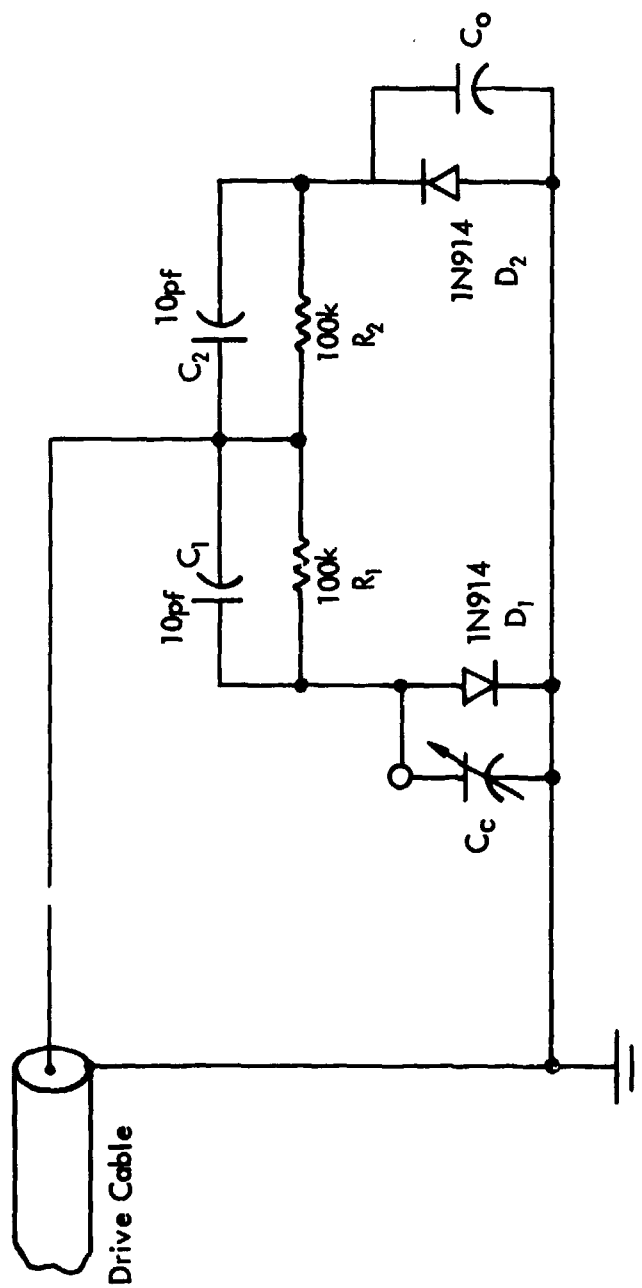


FIGURE 8 APT SENSOR CIRCUIT

in capacitance for this diaphragm displacement is .196 pf. The output voltage increment then becomes

$$dv_s = .093 \times .196 = 18.2 \times 10^{-3} \text{volts.}$$

This value correlates very well with the measured outputs of fifteen transducers made for the arc heater test described in Section 3.

SECTION 3.0

ARC HEATER TEST

3.1 TEST PLANNING

The arc heater test was proposed as an economical method to obtain data which would increase confidence that the APT performed properly in an environment close to that of an RV. An arc heater is a test facility in which high pressure gas is heated by an electric arc to extremely high temperatures. The hot gas flows from a nozzle which is shaped to produce supersonic flow. At its exit plane, the gas is underexpanded and after moving through the exit shock, accelerates very rapidly and forms a plume. Test samples placed in this plume or jet experience heating rates and flow conditions over a limited area which provides a reasonable reentry simulation.

After studying capabilities of several facilities, the 5 Megawatt Arc Heater at AEDC was selected for the test. A Mach number characterization of this facility with a Mach 2 nozzle is presented in Figure 9; this plot was provided by AEDC personnel. Further characterization of the flow is provided by Reference 3, which presented calculated and experimental data on this arc heater. Additional heating rate data from a similar test on carbon-carbon samples was also used to predict test conditions⁴. Calibration data in this latter document predicted centerline heating rates from 600 to 1700 $\frac{\text{joules}}{\text{cm}^2\text{-sec}}$ where the test sample was 4.4 cm from the heater jet exit plane. The face of the model in the cited test was at an angle from 75° to 90° with respect to the flow. Other data showed heating rates higher by a factor of 2 when the model was closer (2.9 cm) and lower by a factor of 3 with a model inclined at a 45° angle.

Radial Profiles

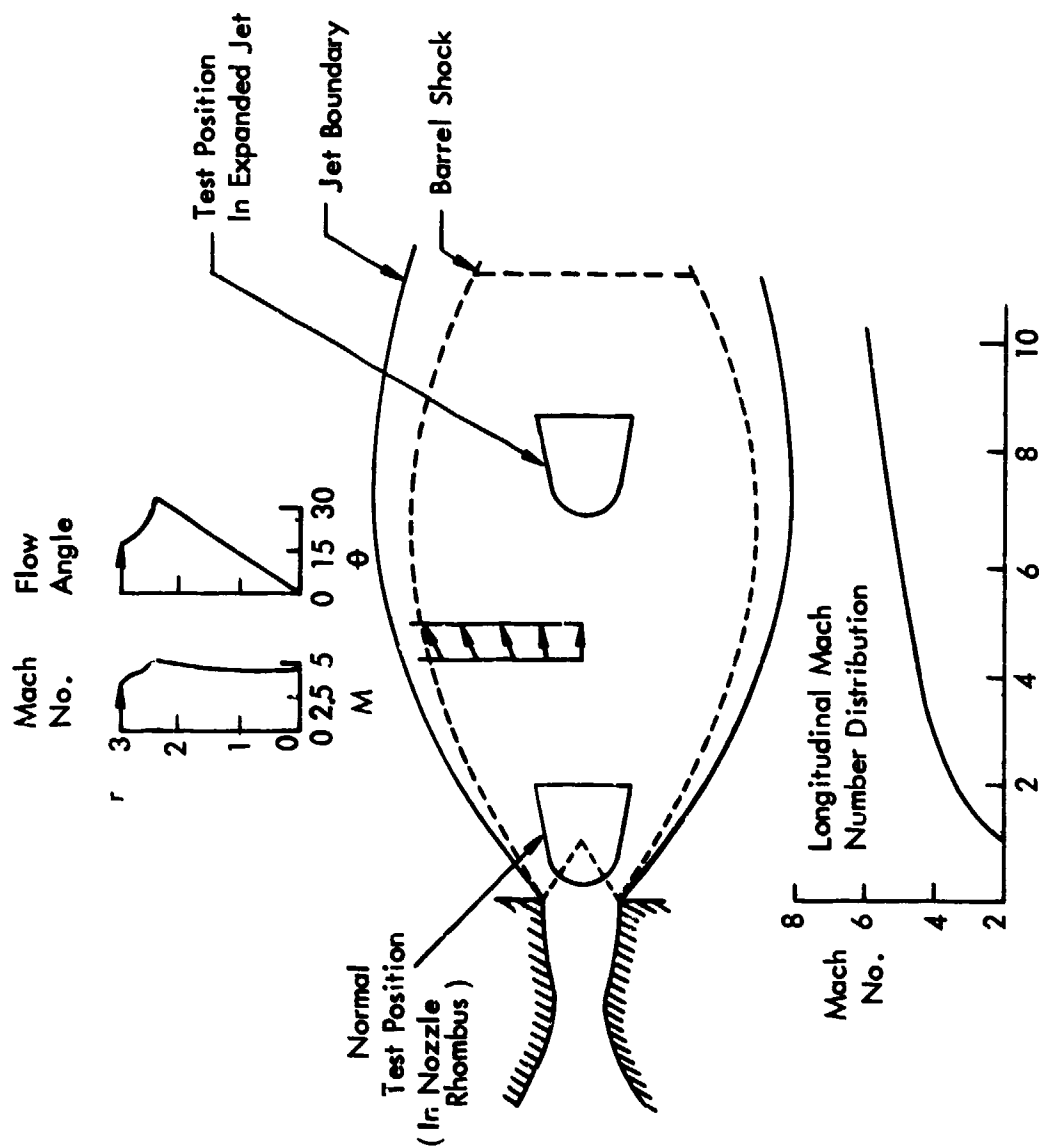


FIGURE 9 MACH 2 ARC HEATER CONDITIONS

Based on the data in these references a test plan was written and forwarded to AEDC providing the details of the test. The approach used in the test plan was to mount the APT's on carbon-phenolic blocks similar to a flight test installation. The C-P test blocks were mounted on steel boxes which protected the transducers, thermal sensors and cabling, and the front face of the test blocks were inclined at an angle of 75° to the flow at the centerline.

Parameter variations in the test matrix included gap dimension between the plug and the test block, gap filler material, and heating rate (proximity to nozzle exit plane). Five seconds duration was selected for the exposures. Four tests were planned with each succeeding test to provide greater severity in the total heat enthalpy. The final test was intended to be a "test-to-failure" in an attempt to determine failure modes. The test plan matrix is shown in Table 2.

After the test plan was submitted, it was decided at a meeting which included DNA, KSC and PDA that the angle of the face of the test block was too steep because the flow across the transducers would not be supersonic. As a result, the test block was redesigned to have a 45° front face angle. Due to the late date in the program, existing hardware could not be extensively redesigned but was modified to accept the face angle change. The test blocks had been fabricated, thus the thermocouple depth could not be changed.

Because of the shallower impact angle of the jet on the test block face, surface pressure and heating rate were expected to be significantly less than planned. Predictions were made of the pressure on the surface based on inviscid relationships and data found in NACA Report 1135⁵. The largest uncertainty with these predictions was that the angle of the flow varied radially in the jet, thus, non-ideal conditions existed with which to make the

TABLE 2 APT ARC HEATER TEST

TEST PLAN MATRIX

<u>TEST BLOCK NO.</u>	<u>TRANSDUCERS</u>	<u>GAP DIMENSIONS-CM</u>	<u>GAP FILLER</u>
1	APT	.0127	Air
	APT	.0127	Silicone
2	APT	.0127	Alumina
	APT	.0254	Alumina
3	APT, BLAM	.0254	Silicone
	APT	.0254	Air
4	APT	.0381	Alumina
	APT	.0381	Air
5	APT	.0381	Silicone
	Kistler	.0762 (Port)	
6 CAL	2 Kistler	.0762 (Ports)	
	3 Calorimeter		
7 CAL	2 Kistler	.0762 (Ports)	
	3 Calorimeter		

<u>RUN NO.</u>	<u>DISTANCE FROM NOZZLE-CM</u>	<u>EST. STAG. PRESSURE ATM</u>	<u>EST. HEAT RATE RANGE JOULES/CM²-SEC</u>	<u>DURATION SEC.</u>
1	5.08	5	570-800	5
2	4.45	6.6	910-1370	5
3	3.81	9	1700-2050	5
4	3.18	12	>2300	5

prediction. Curves of static pressure versus flow Mach number and deflection angle are presented in Figure 10. These curves assume a parallel uniform flow and a shock at some standoff distance from the surface. The estimated span of the angle of flow is also marked on the plot in Figure 10.

3.2 TEST HARDWARE DESIGN

3.2.1 Sample Block Layout

The original test block layout included a front face angle of 75° which was later changed to 45° . Drawings of the 45° test and calibration blocks are shown in Figures 11 and 12 respectively. Photographs of these same assemblies are shown in Figures 13 and 14.

In order to gain clearance for the connector at the back of the APT inside the housing, the centerline of the transducer was raised 1.27 cm from its position in the 75° housing. The jet centerline intersected the sample block below the transducer centerline by a corresponding amount.

The calibration block (Figure 12) was designed to contain five sensors: Two pressure and three thermal. Kistler pressure gages supplied by AEDC were installed in the calibration blocks. The thermal sensors were designed and fabricated by KSC and are described in Section 3.2.2.

Test sample instrumentation included two pressure transducers and an imbedded thermocouple in each CP block. Two APT's were mounted on four test blocks. One APT and one Kistler were installed on a fifth block. The thermocouple was centered between the two pressure transducers in all five test samples.

Unfortunately, test samples constructed as shown in Figure 11 were destroyed in the first test because the steel supports on the front face were uninsulated and melted rapidly. Prior to the

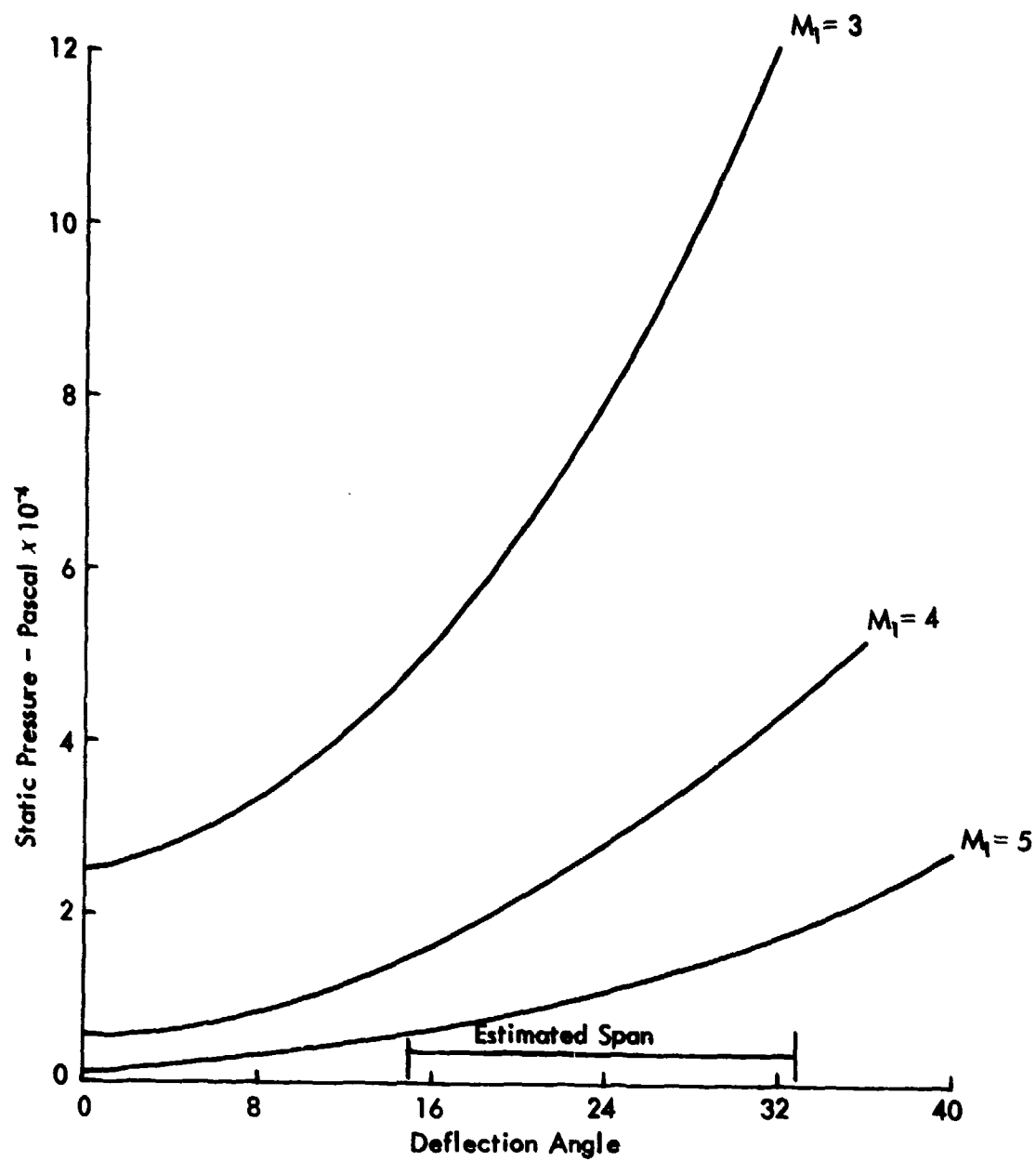


FIGURE 10 PRESSURE PREDICTION

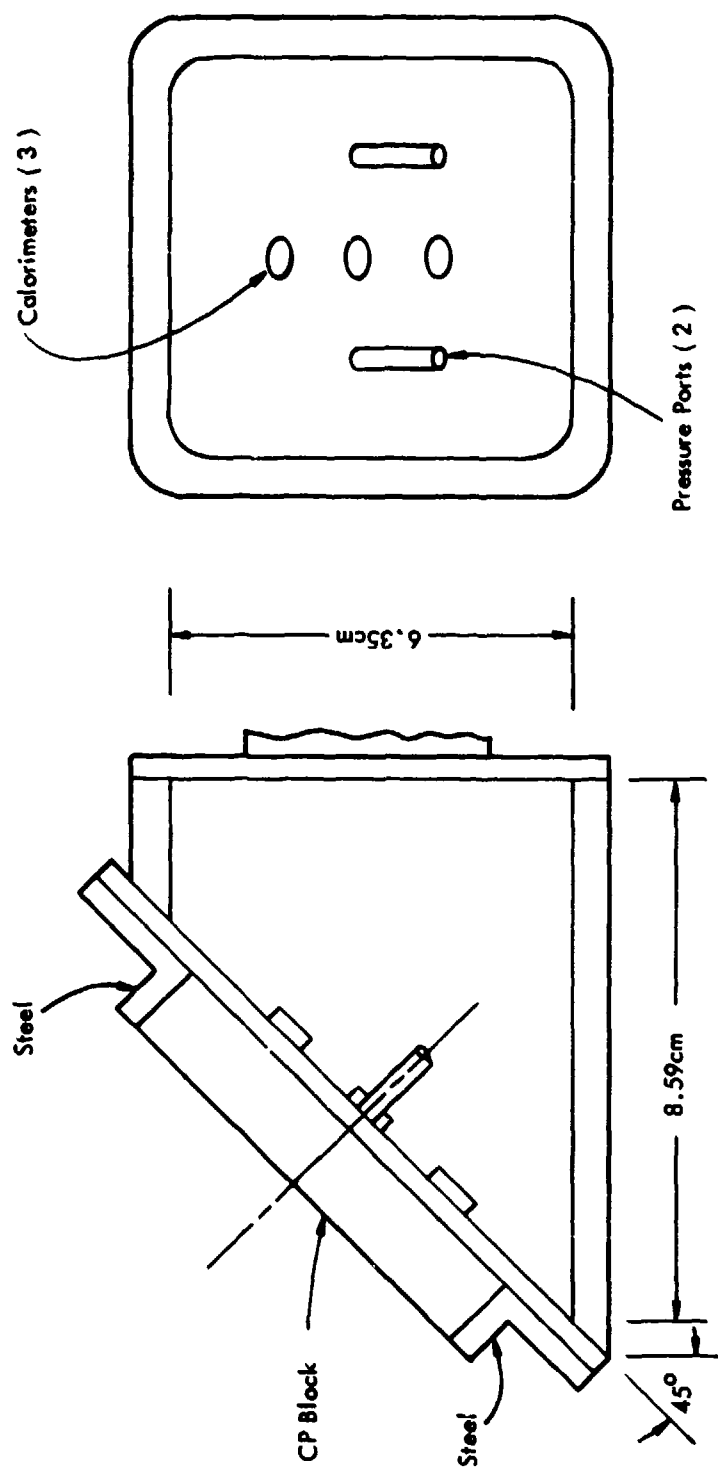


FIGURE 11 TEST BLOCK INTERIOR LAYOUT

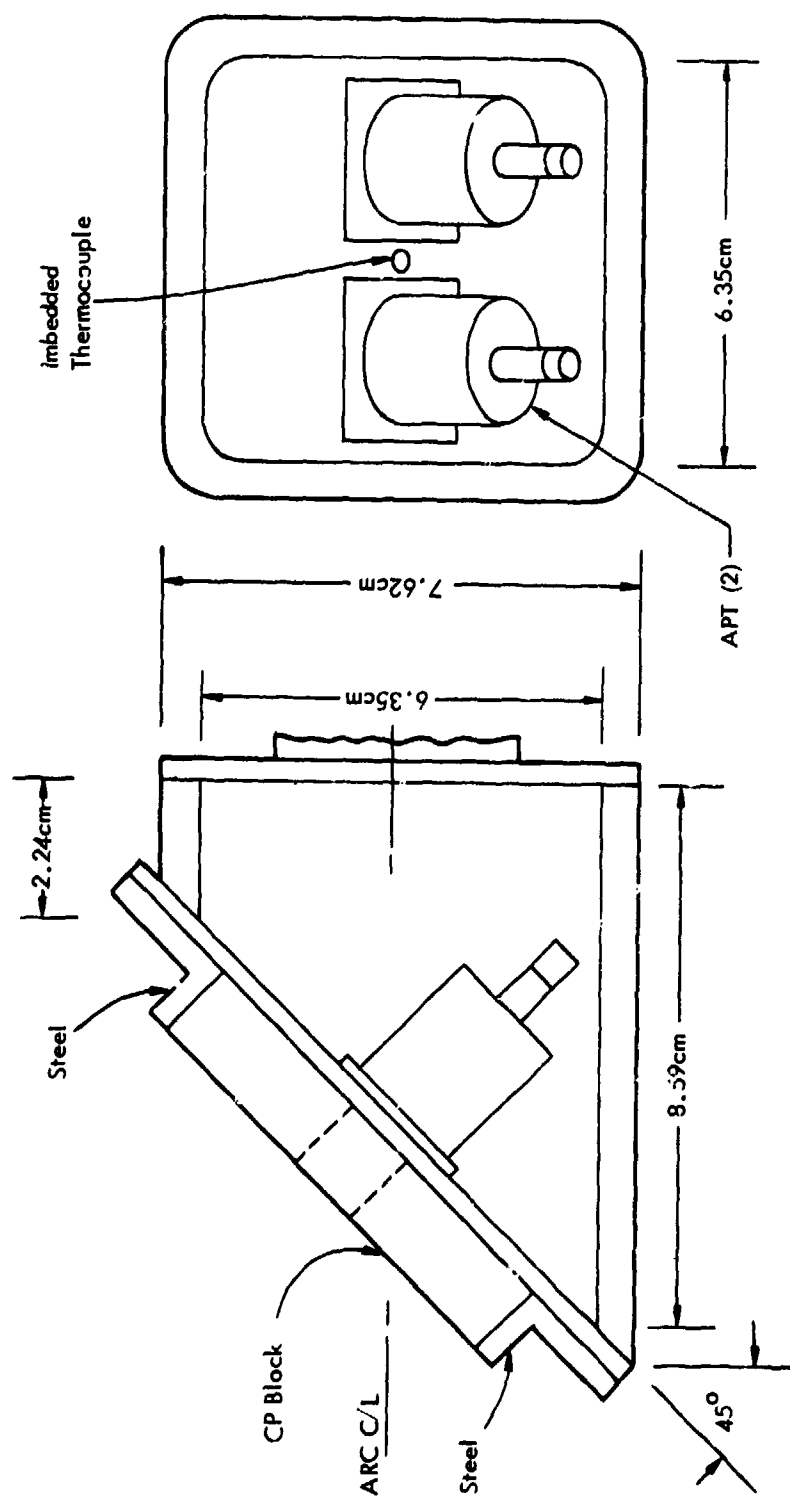


FIGURE 12 CALIBRATION BLOCK INTERIOR LAYOUT

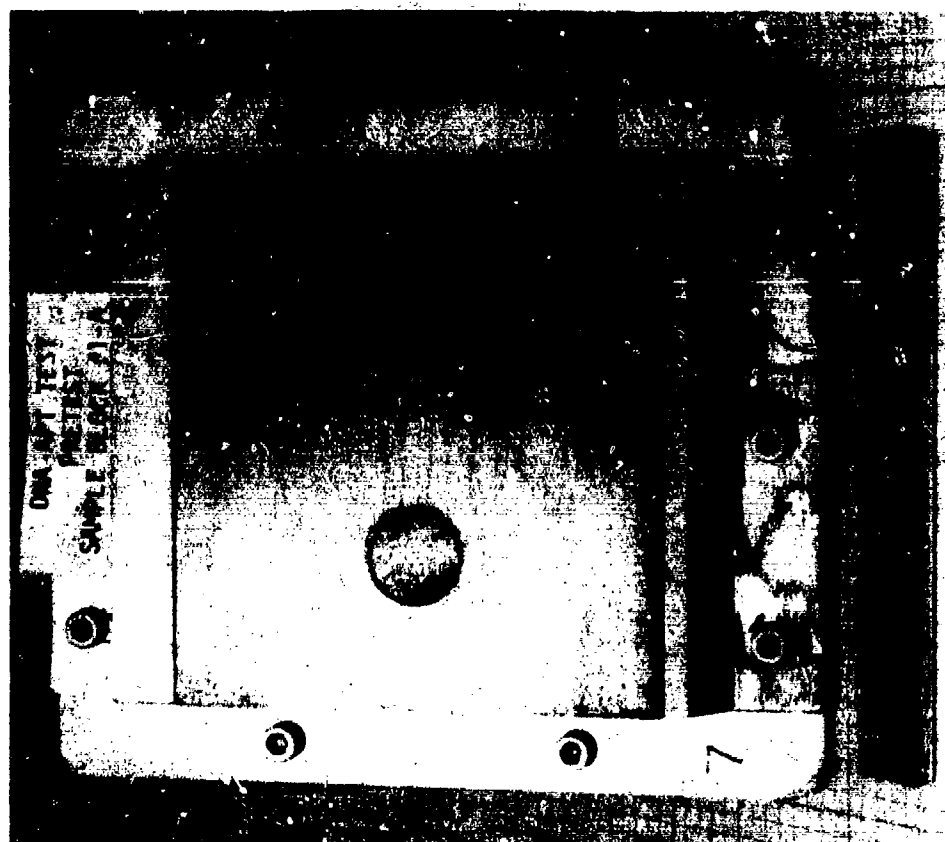


FIGURE 13 TYPICAL TEST BLOCK ASSEMBLY

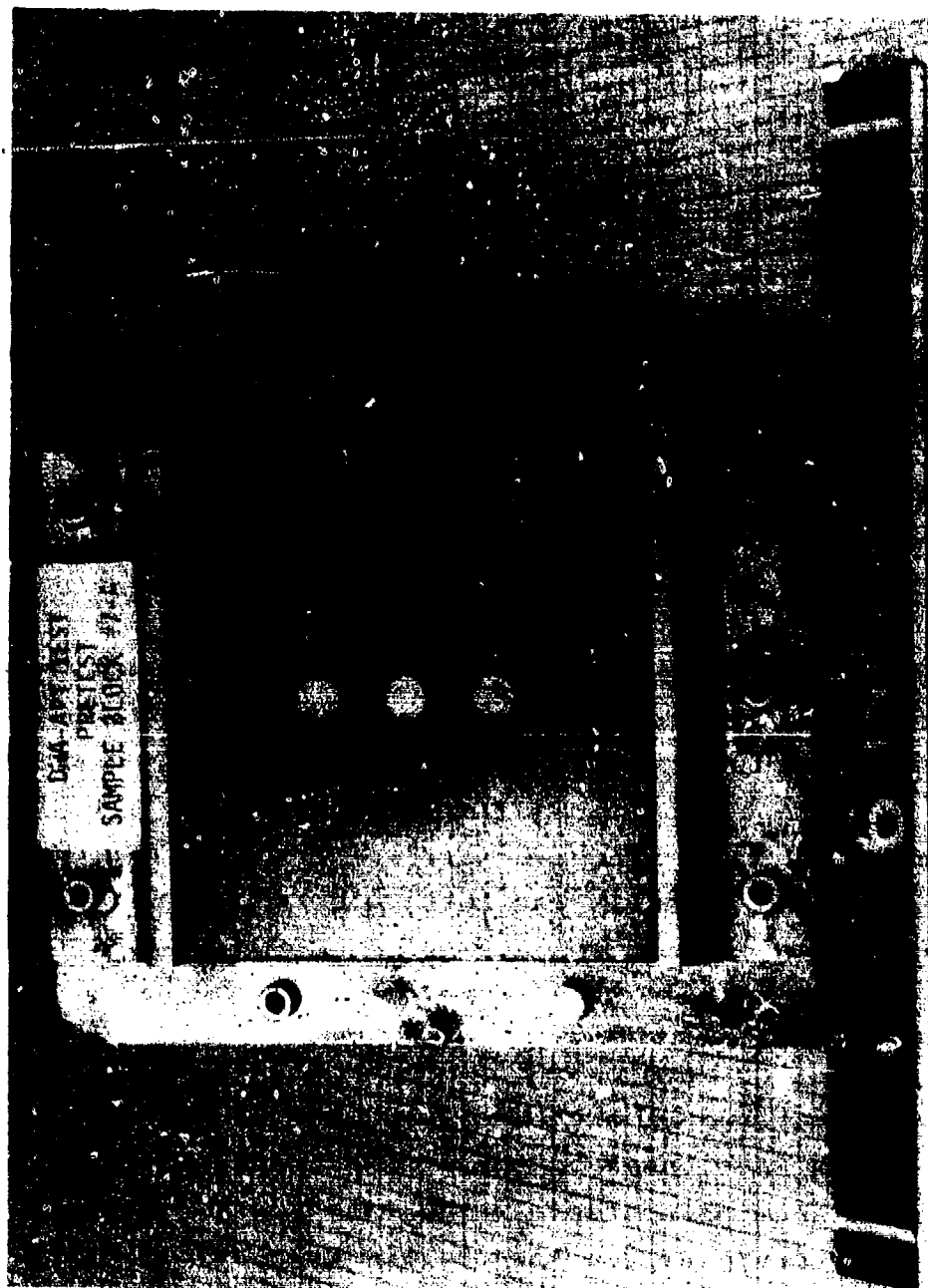


FIGURE 14 TYPICAL CALIBRATION BLOCK ASSEMBLY

second test, insulation was placed on the bottom part of the face as indicated in Figure 15. The remainder of the tests were successful in that this added insulation survived the arc jet exposures.

3.2.2 Thermal Sensor Designs

Two types of thermocouple sensors were designed and built for the arc heater test. One type of these sensors was installed in the calibration test blocks and was intended to obtain heating rate measurements before and after test model exposure. As can be seen in Figure 12, three sensors were installed in each calibration block so that as the model was swept through the heater jet, a profile of surface heating conditions could be obtained which bracketed the position of the APT's within the arc heater plume.

The calibration sensors were copper slug calorimeter constructed as shown in Figure 16. A small diameter teflon insulated constantan wire was placed in a .0254 cm channel cut in the side of a copper rod and soldered at a point .025 cm from the top of the rod. The rod was inserted inside a close fitting copper tube and assembly was then soldered together. A thermocouple reference junction was made on the back surface of the slug to complete the calorimeter.

Predictions were made of the output of the calorimeter in the environment to be encountered in the arc heater test. The calculations were based on one-dimensional heat flow in an infinite slab with a step heating rate input. This approach is satisfactory provided the surface temperature of the slug is limited to several hundred degrees Celsius. Figure 17 is a plot versus time of the calorimeter output for several heating rate

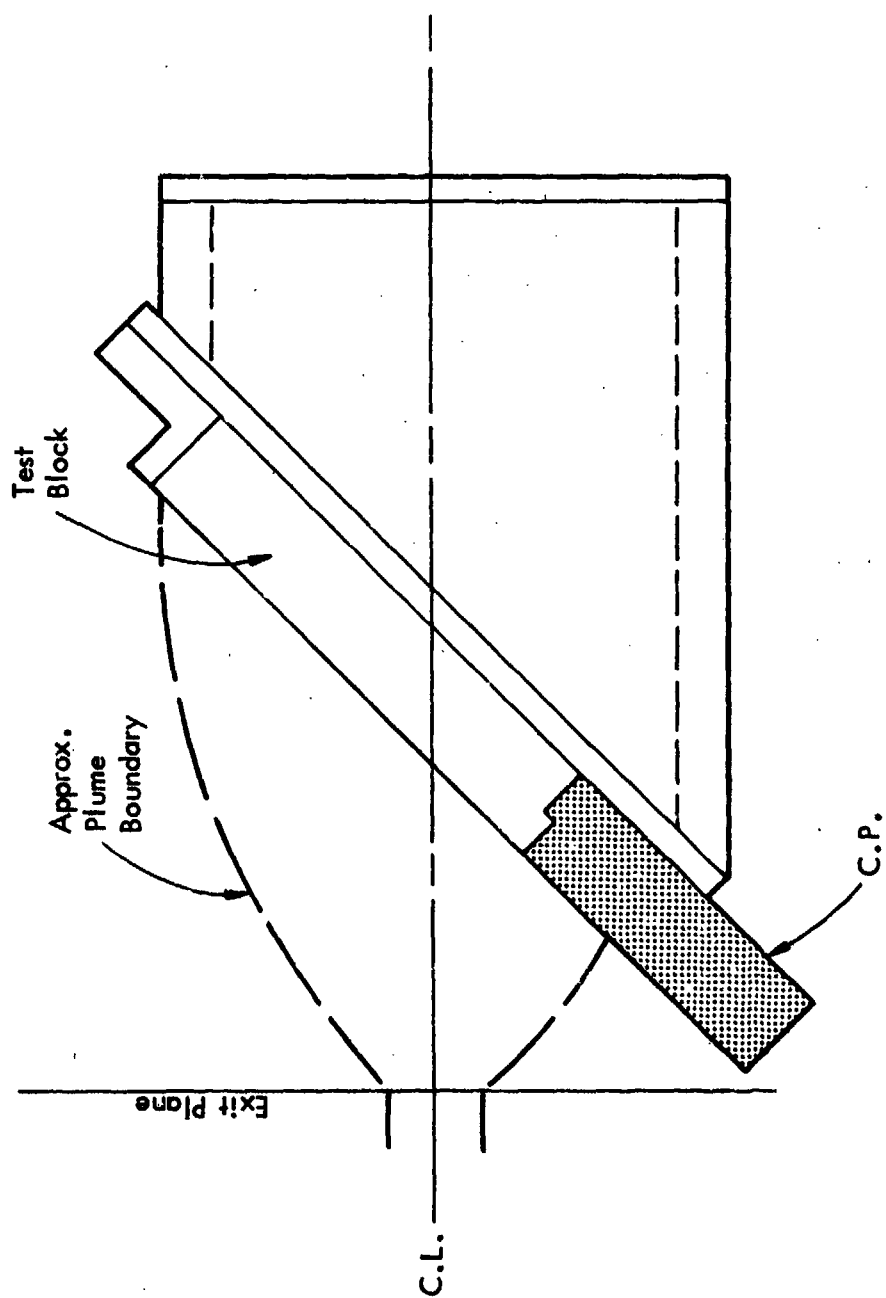


FIGURE 15 INSULATED TEST SAMPLE

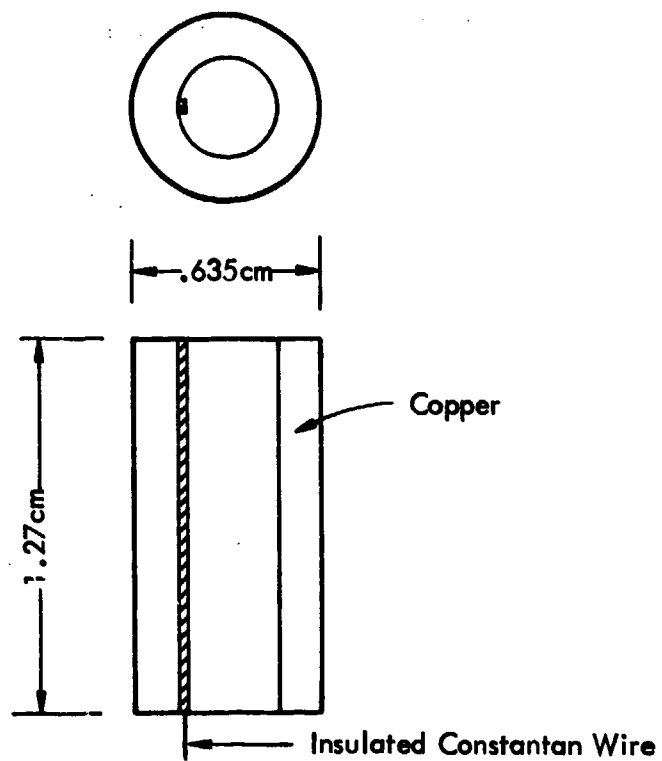


FIGURE 16 CUPPER CALORIMETER

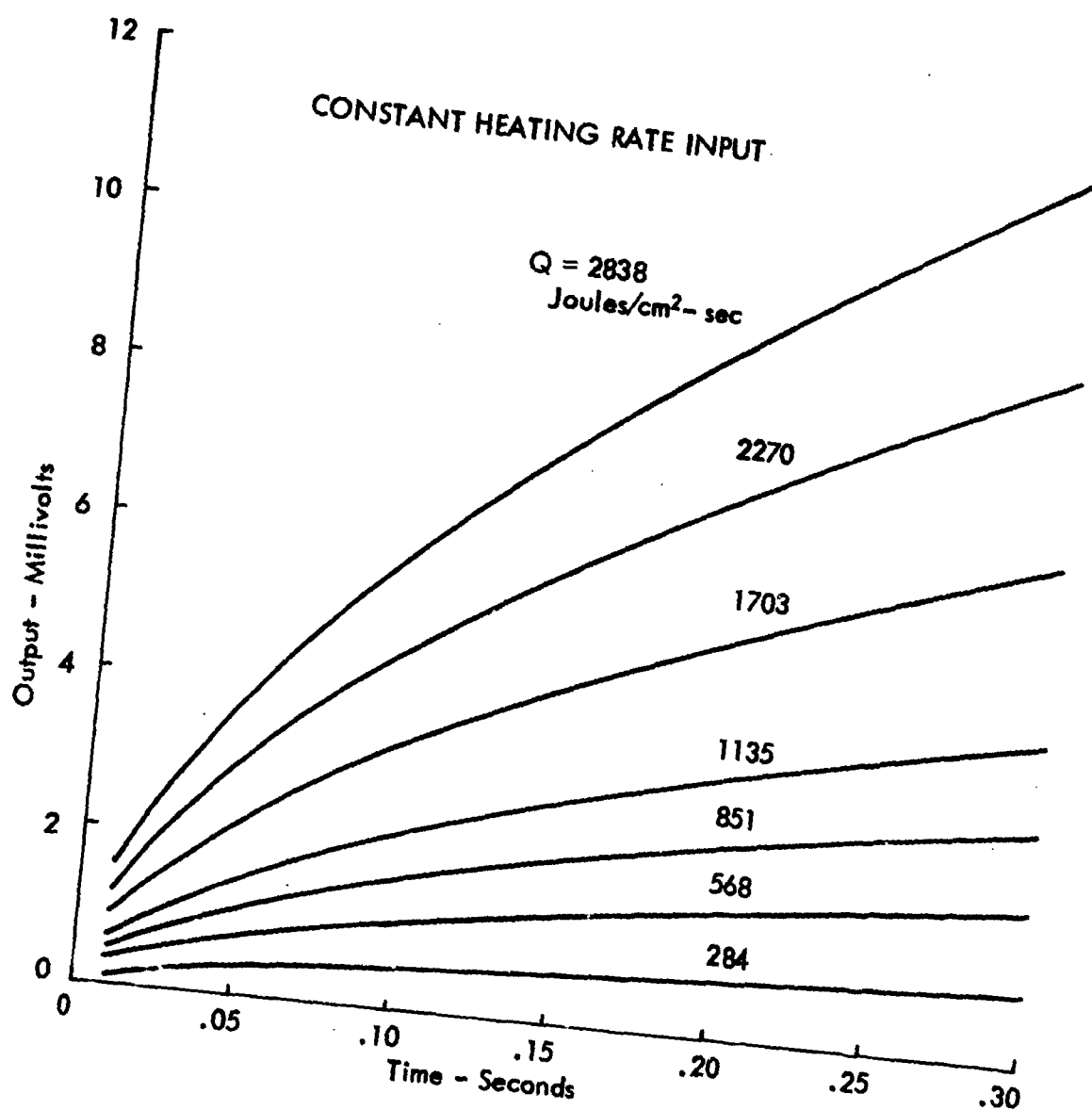


FIGURE 17 PREDICTED CALORIMETER OUTPUT

levels. These data were used to set amplifier levels for signal recording in the first test in which it was estimated that the heating rate would be approximately $700 \text{ joules/cm}^2\text{-sec}$.

Thermal sensors imbedded in each of the test blocks were intended to provide data on the indepth temperature and uniformity of exposure from sample to sample. Using heat characteristics of carbon-phenolic, the temperature distribution at depth was calculated for several surface heating rates. These curves are presented in Figure 18. Installation depth of .38 cm was selected based on the estimate that the surface heating rate would be between 340 and $570 \text{ joules/cm}^2\text{-sec}$. This range of heating rate was used for the design prior to the first trial run in the arc heater.

The test sample thermocouples were beaded junctions of fine chromel-alumel wire held in small diameter twin bore ceramic tube. A hole was drilled in the CP from the back to the proper depth. The tube was inserted so that the thermocouple bead was touching the CP; this assembly was bonded in place. The reference junction was placed on a terminal strip mounted on the back of the CP block.

3.3 TEST RESULTS

3.3.1 Summary

A total of six arc heater runs were completed during the APT test series, three check and three test runs. Table 3 is a compilation of test parameters for the six runs, showing both model conditions and purpose.

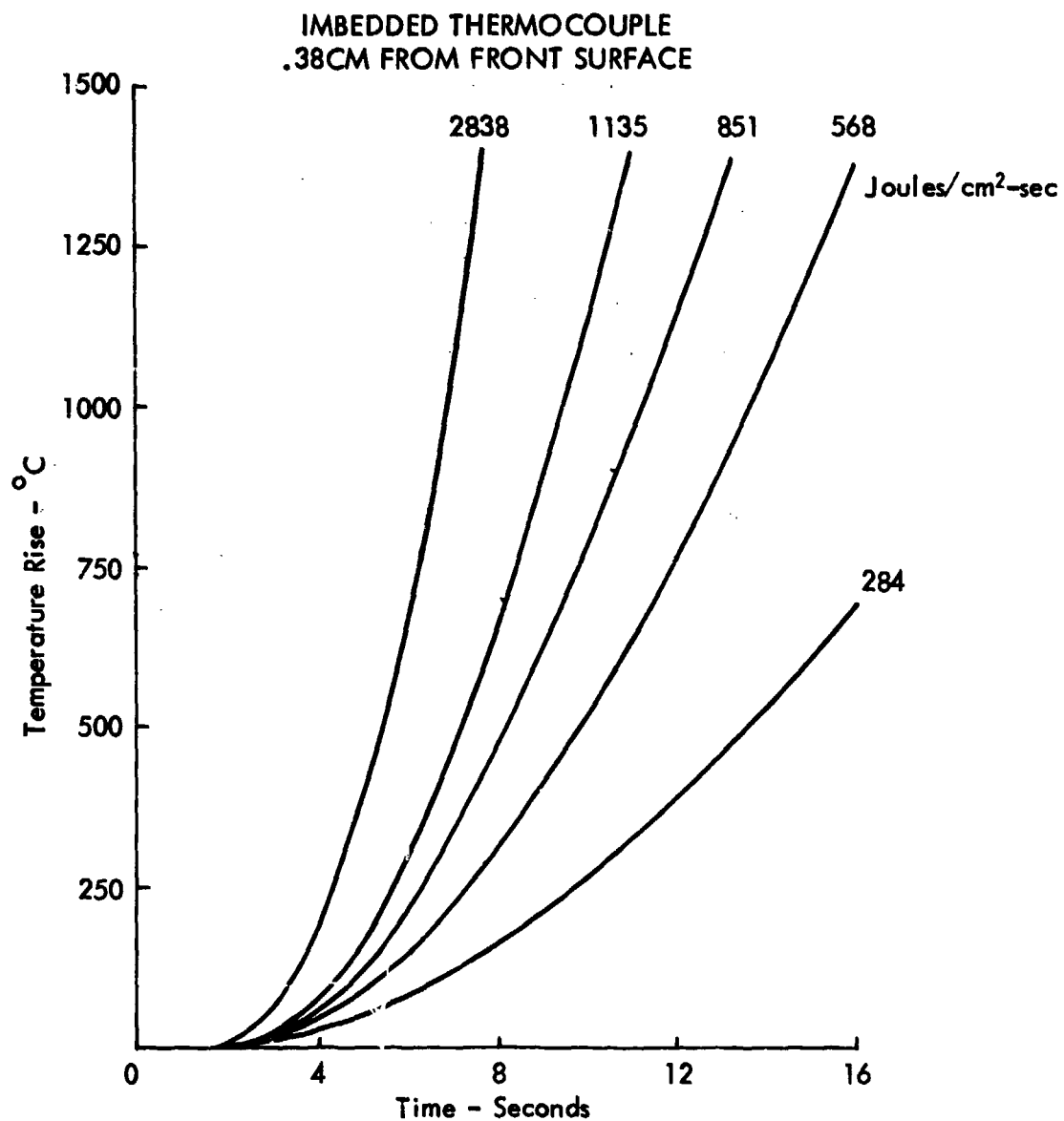


FIGURE 18 PREDICTED TEMPERATURE HISTORY

TABLE 3 ARC HEATER RUN PARAMETERS

<u>RUN NO.</u>	<u>PURPOSE</u>	<u>HEATER CONDITIONS</u>	<u>RESULTS</u>
Check 1	Facility checkout	HOB = 5.57 kJ/kg	Noise on digital system
	Recording system test	P _O = 164.7 atm 16.27 MW	
Check 2	Recording system test		Heat rate on cal model high
	Arc calibration		
Test 1	APT test	HOB = 4.91 kJ/kg P _O = 168 atm 6.14 MW	Good data, damage to models
Check 3	Test additional model insulation	HOB = 5.84 kJ/kg P _O = 168 atm 6.88 MW	Insulation held
Test 2	APT test	HOB = 5.26 kJ/kg P _O = 168.6 atm 6.61 MW	Good data
Test 3	APT test	HOB = 5.27 kJ/kg P _O = 168.8 atm 6.47 MW	Good data

HOB = Heater gas enthalpy

KJ = Kilojoules

kg = kilograms

MW = Megawatt

Data success was high for the three test runs in that usable records were obtained on all channels with the exception of the thermocouples imbedded in the centers of the test blocks. In the first run, hot gas entered the inside of the test blocking housing and raised the temperature of the reference junction, thus eliminating any possibility of data. In the second and third tests, the duration was too short to raise the thermocouple output to a recordable level (reference Section 3.2.2). Fortunately, data from the imbedded thermocouples were not primary for test purposes.

Test model instrumentation parameters are given in Table 4 for the three test runs. Parameters varied were the gap width and gap filler material. The gap width was varied to determine if aerodynamic flow causes pressure indication differences such as is encountered in the use of ported pressure gages. The gap filler materials - air, high temperature fibers, and viscous silicone compound - were used to obtain a comparison of reduction of flow around the plug as well as to determine if insulation is needed around the transducer.

Outputs from all sensors were recorded on oscillographs, the calibration model thermocouples and pressure sensors on a Honeywell 1612 which used fast-developing strip chart paper and the test model sensor outputs on a CEC oscillograph with permanent type strip chart. Strip chart speeds were 406.4 cm/sec on the Honeywell and 63.5 cm/sec on the CEC recorder. Resolution of the data on the strip charts was approximately one millisecond for all records.

Photographs, both still and motion, were taken. The still pictures were taken pre- and post-test of each of the models.

TABLE 4 MODEL CONFIGURATIONS

<u>RUN NO.</u>	<u>CP BLOCK NO.</u>	<u>STING POSITION</u>	<u>APT SERIAL NO.</u>	<u>GAP WIDTH (CM)</u>	<u>GAP FILLER</u>
1	16R	2	6	.0127	Silicone Compound
	16L		7	.0127	Air
	15R	3	12	.0127	Alumina Fiber
	15L		11	.0254	Alumina Fiber
	9R	4	9	.0254	Air
	9L		1	.0254	Silicone Compound
	8R	5	15	.0381	Alumina Fiber
	8L		8	.0381	Air
	4R	6	10	.0381	Silicone Compound
2	10R	2	2	.0127	Silicone/Alumina Fiber
AND	10L		5	.0127	Silicone Compound
3	12R	3	4	.0254	Silicone/Alumina Fiber
	12L		13	.0254	Silicone Compound
	7R	4	3	.0254	Silicone/Alumina Fiber
	7L		14	.0127	Silicone/Alumina Fiber

Motion pictures were taken from two directions during each test run, one with a profile view and one with a frontal view of the test block. Due to not knowing the surface brightness, motion pictures of the first test run were overexposed; pictures of the second and third test runs were excellent.

During each test, sequence of acquiring data was set by the cycling of stings into position in the heater jet. Table 5 lists the sequence used for each of the three tests, and test duration for each model. The calibration models were swept through at a circumferential velocity of 63.5 cm/sec and the time listed is the time taken for the model to reach the centerline from the edge of the flow. The test duration is the time during which the test model dwells in the flow.

3.3.2 Test Run No. 1 Data

Thermal data are plotted in Figures 19 and 20 from the calibration sweep models. Figure 19 is data from sting 1 which preceded the models and Figure 20 is from sting 7 which swept through after the models. Using the curves in Figure 16, heating rates for each of the thermocouple traces were estimated with results in the following table:

Thermocouple No.	Location	Heat Rate at Flow C/L
TC1	1.27 cm Up	1500 joules/cm ² -sec
TC2	Center	1330
TC3*	1.27 cm Down	2000
TC4	1.27 cm Up	1900
TC5	Center	1600
TC6*	1.27 cm Down	2640

* Approximately at arc center.

TABLE 5 TEST SEQUENCES

<u>TEST RUN NUMBER</u>	<u>STING SEQUENCE</u>	<u>TEST BLOCK</u>	<u>SENSOR SEQUENCE</u>	<u>DURATION (SECONDS)</u>	
1	1	1	K-1 TC1, TC2, TC3 K-2	0.1	
	2	16	APT 6 APT 7	4	
	3	15	APT 12 APT 11	4	
	4	9	APT 9 APT 1	4	
	5	8	APT 15 APT 8	4	
	6	4	APT 10 K-3	4	
	7	2	K-4 TC4, TC5, TC6 K-5	0.1	
2 AND 3				<u>Test 2</u>	<u>Test 3</u>
	1	1	K-1 TC1, TC2, TC3 K-2	0.1	0.1
	2	10	APT 2 APT 5	1.1	1.8
	3	12	APT 4 APT 13	1.1	1.8
	4	7	APT 3 APT 14	1.1	1.8
	6	2	K-4 TC4, TC5, TC6 K-5	0.1	0.1

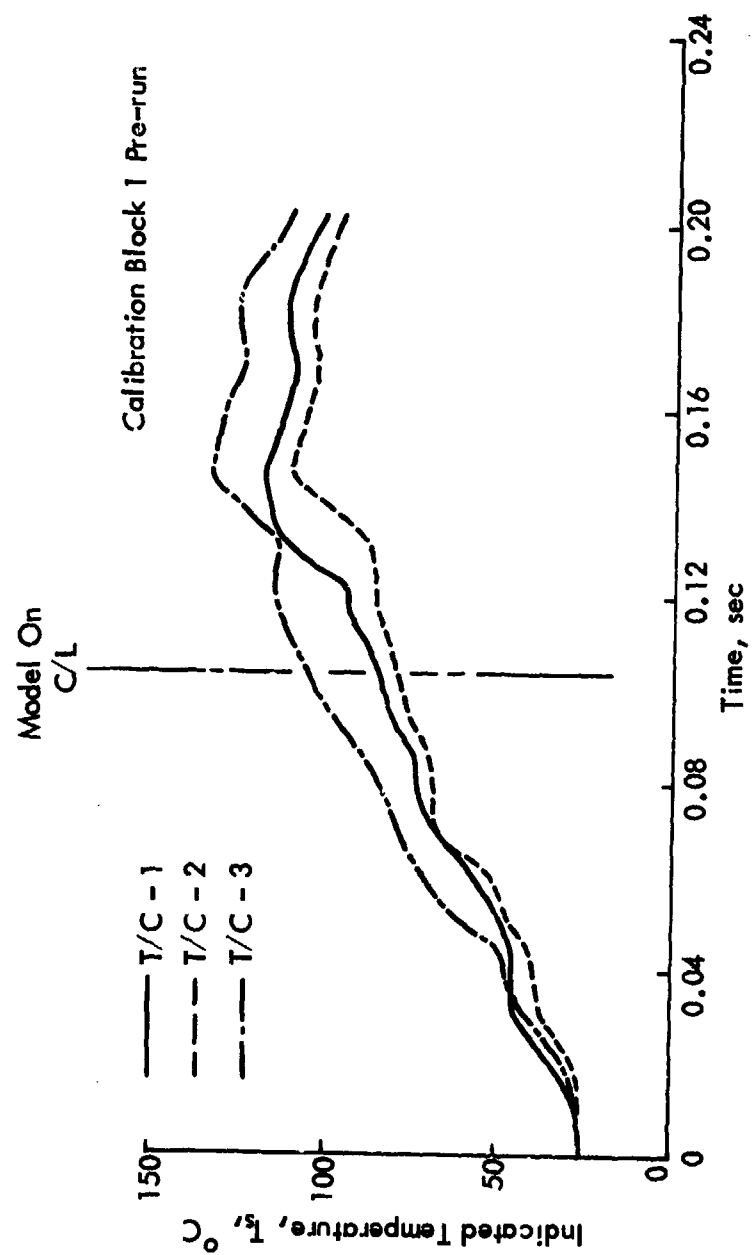


FIGURE 19 TEST RUN 1 CALIBRATION DATA-THERMAL

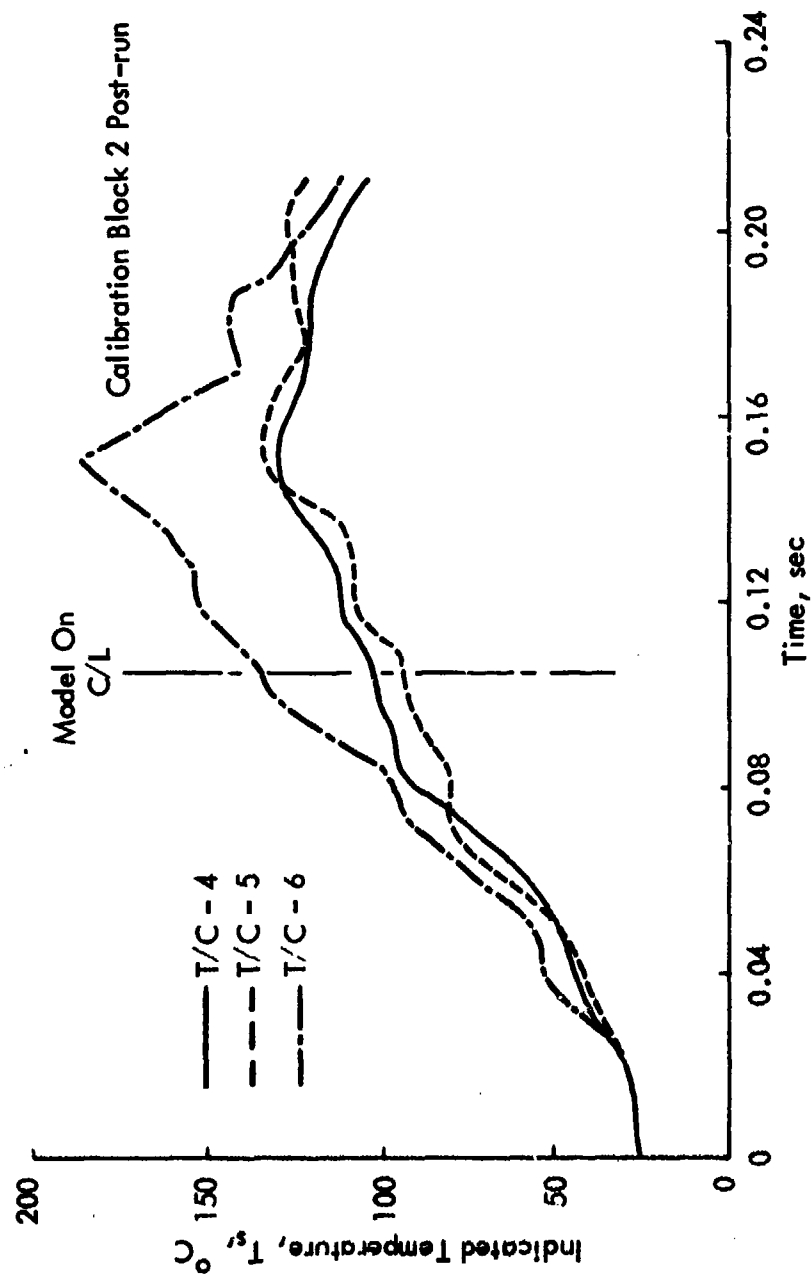


FIGURE 20 TEST RUN 1 CALIBRATION DATA-THERMAL

Heating rate decreased from the center of the arc out to the position of the barrel shock. The data show that TC1 and TC4 are located close to the barrel shock because the temperatures are higher than at the block centers near TC2 and TC5. This is verified by photos from Runs 2 and 3 which are presented later in the report.

Pressure data obtained by the Kistler transducers mounted in the calibration blocks are plotted in Figures 21 and 22. These traces are profiles of the pressure on the model face as the model is swept through the arc. The peaks at either end are characteristic of the pressure profile in arc heaters and indicate the presence of a barrel shock. The test region is inside the shock in the flatter shaped section where the figures are marked "Model on C/L." The pressure transducer is in the same position as the APT transducer in the test models, either right or left as the case may be.

A comparison of Figures 20 and 21 reveals that some inconsistencies exist; e.g., the flow centerline pressures differ by as much as 50% between transducers K4 and K5. Reasons for these differences may be the flow interaction with the port arc heater variations or transducer calibrations although the latter is the least suspect because of prior AEDC experience with this sensor. No firm reason has been established at this time.

Records of the APT outputs are plotted in Figures 23 through 27; the Kistler transducer K3 pressure trace is also seen in Figure 27. Recalling that the sample block holders in test number 1 burned through and that the transducers were destroyed, the following comments are offered on the data of Figures 23 through 27.

Calibration Block 1

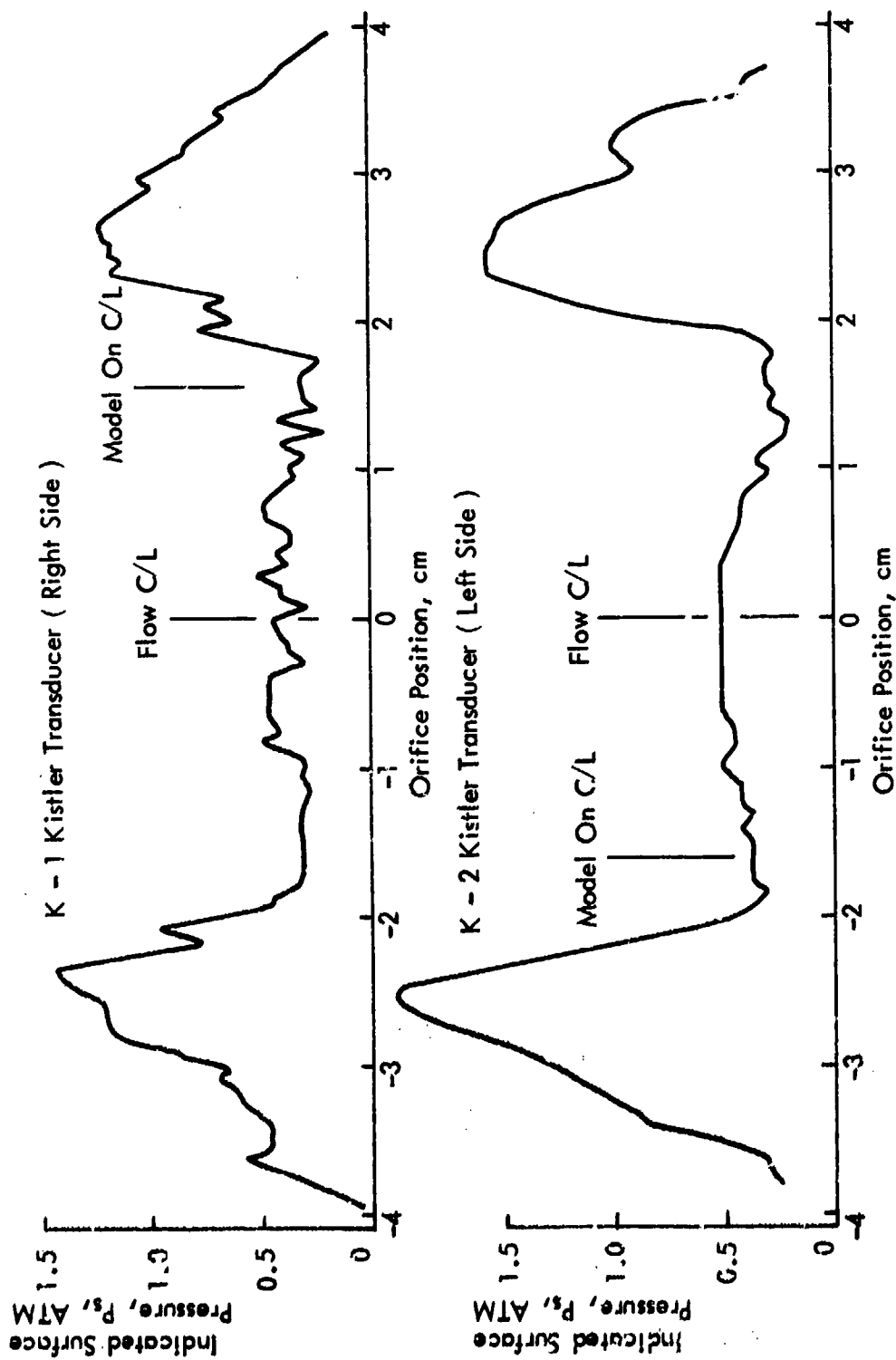


FIGURE 21 TEST RUN 1 CALIBRATION DATA PRESSURE

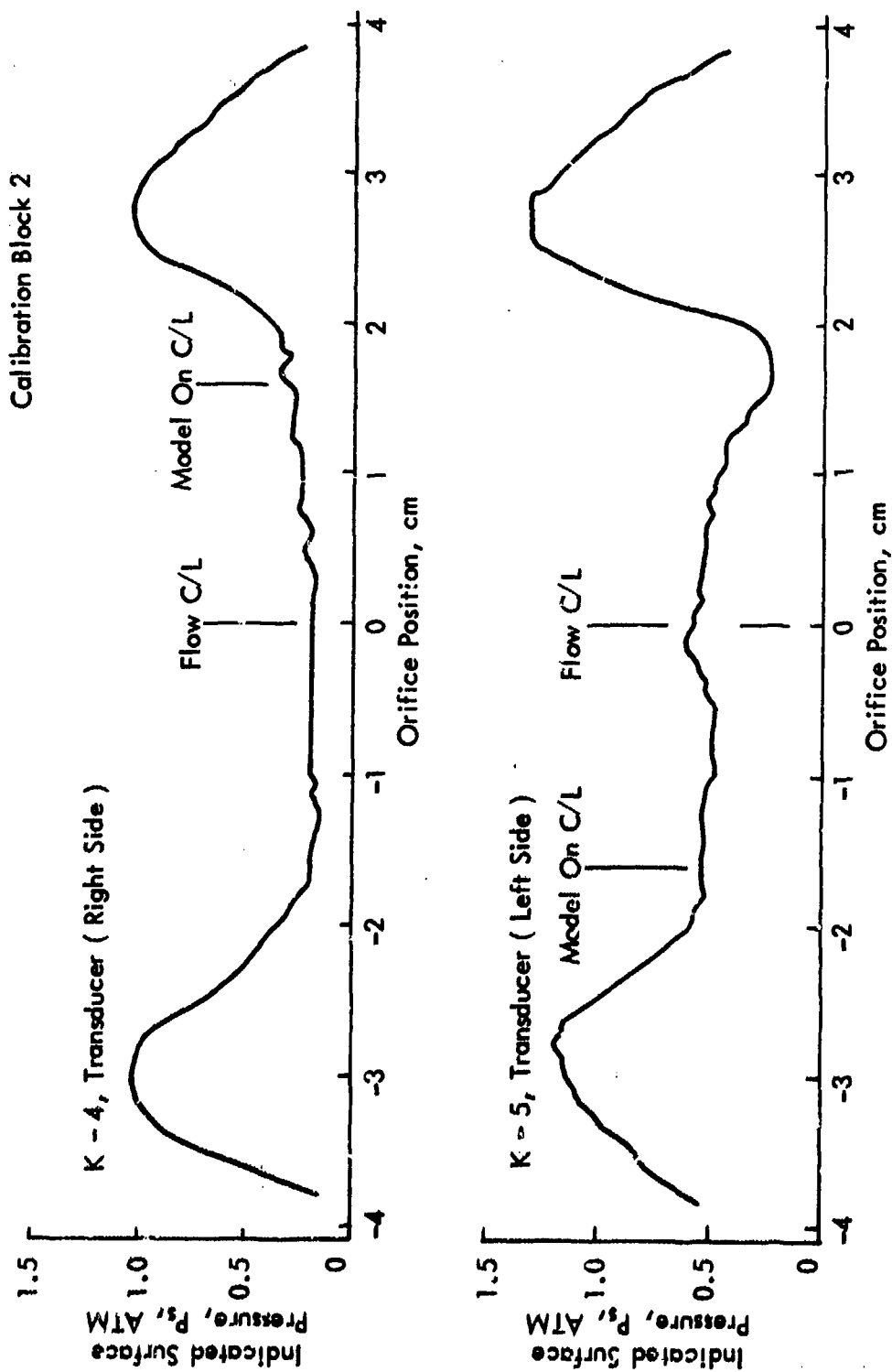


FIGURE 22 TEST RUN 1 CALIBRATION DATA PRESSURE

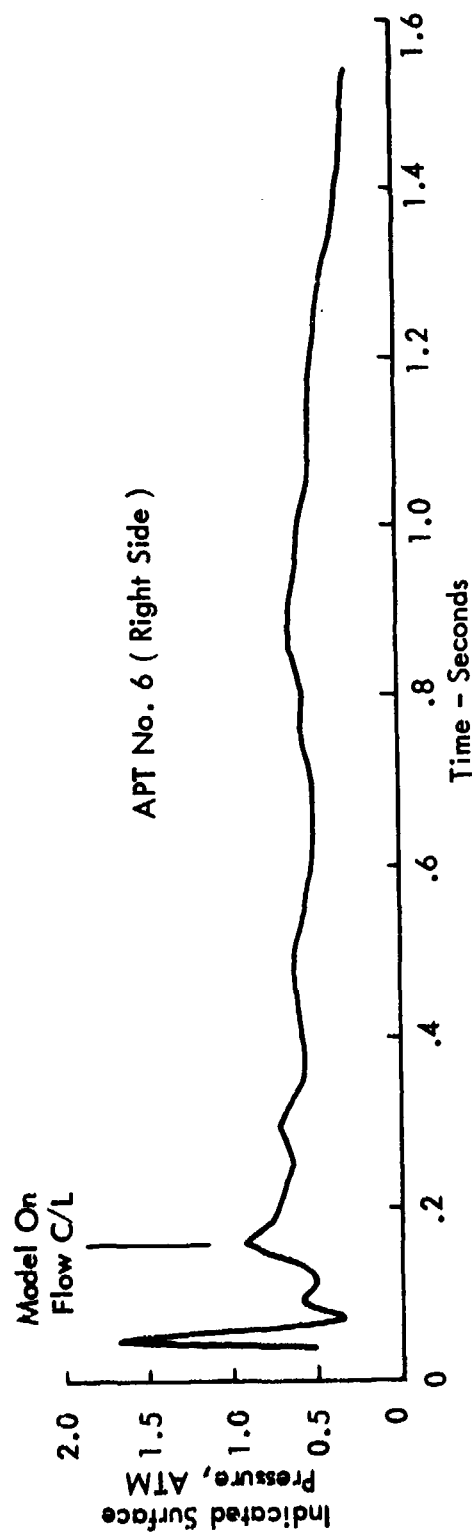
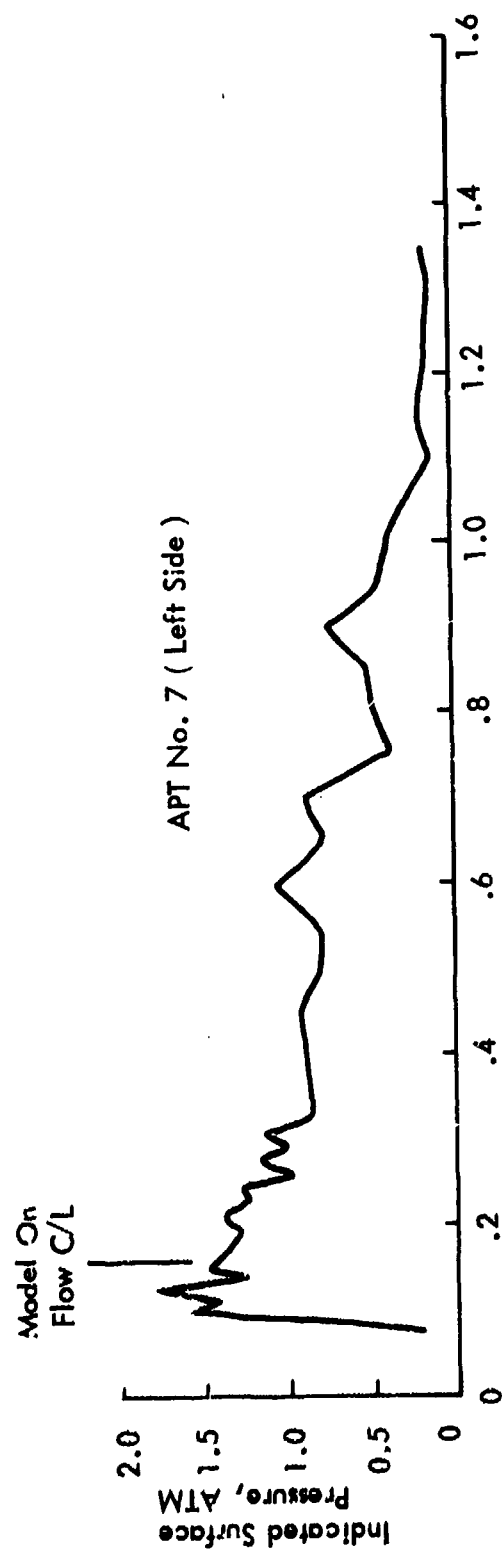


FIGURE 23 TEST RUN 1 APT DATA

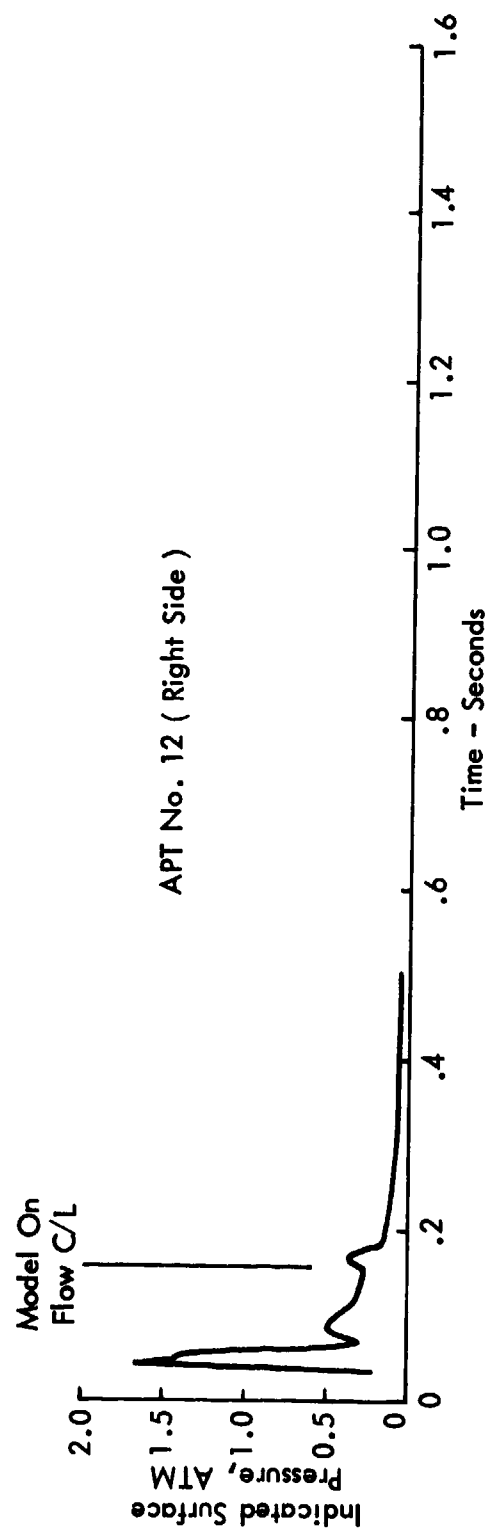
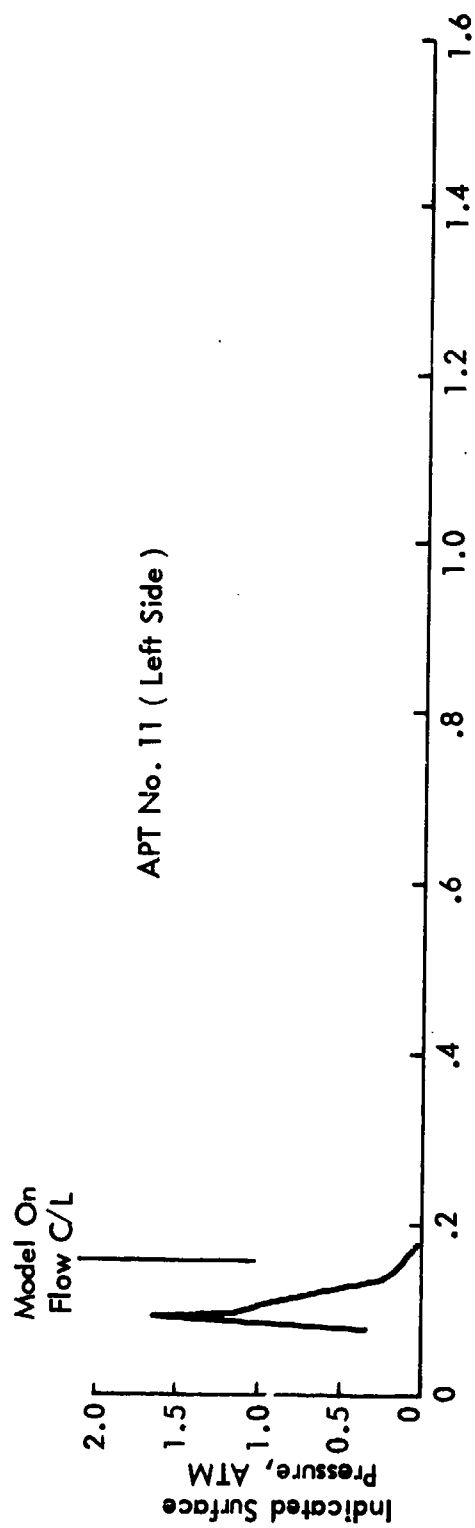


FIGURE 24 TEST RUN 1 APT DATA

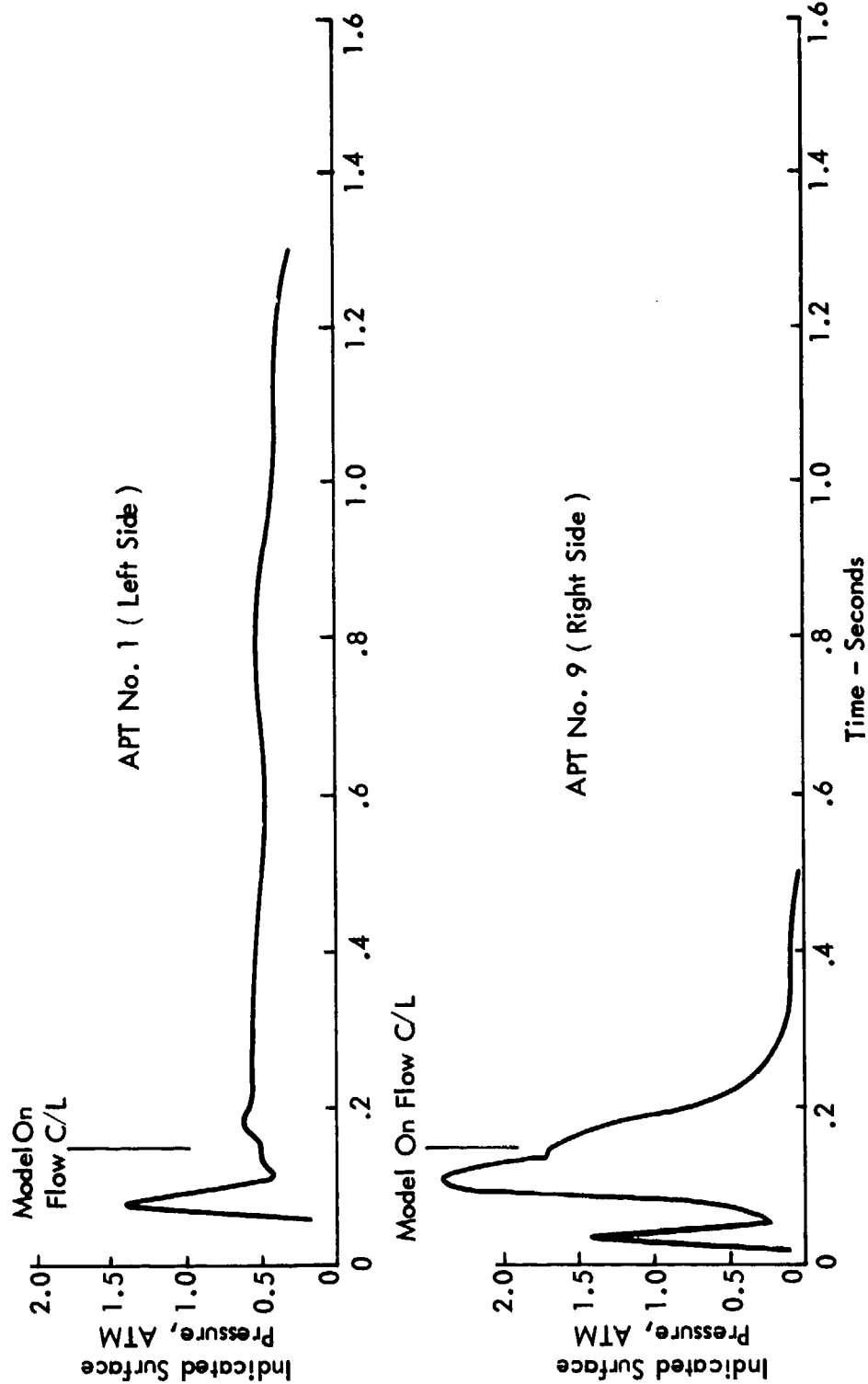


FIGURE 25 TEST RUN 1 APT DATA

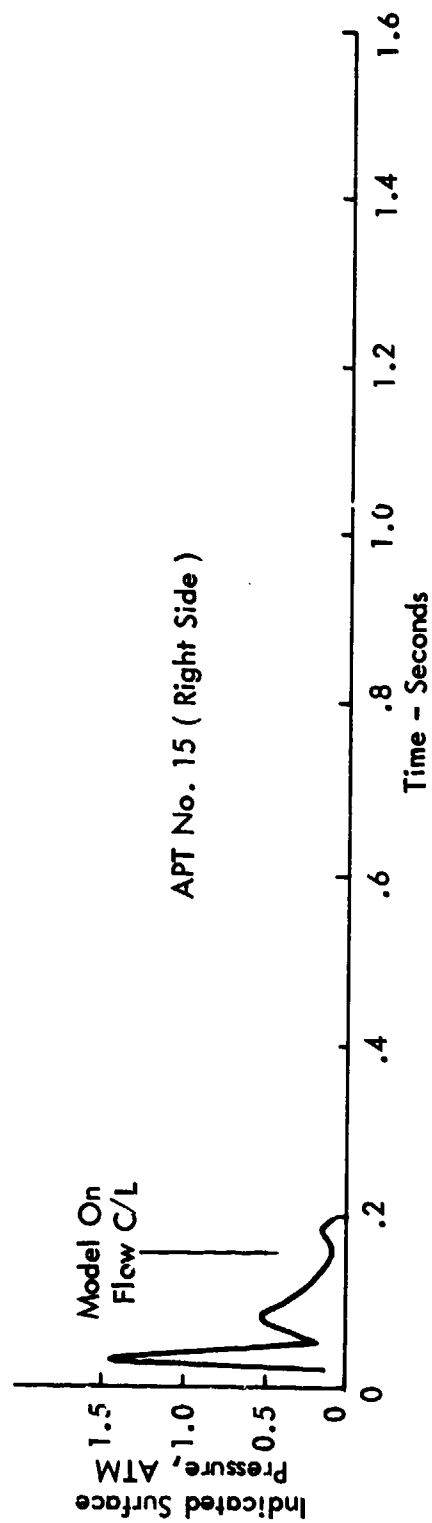
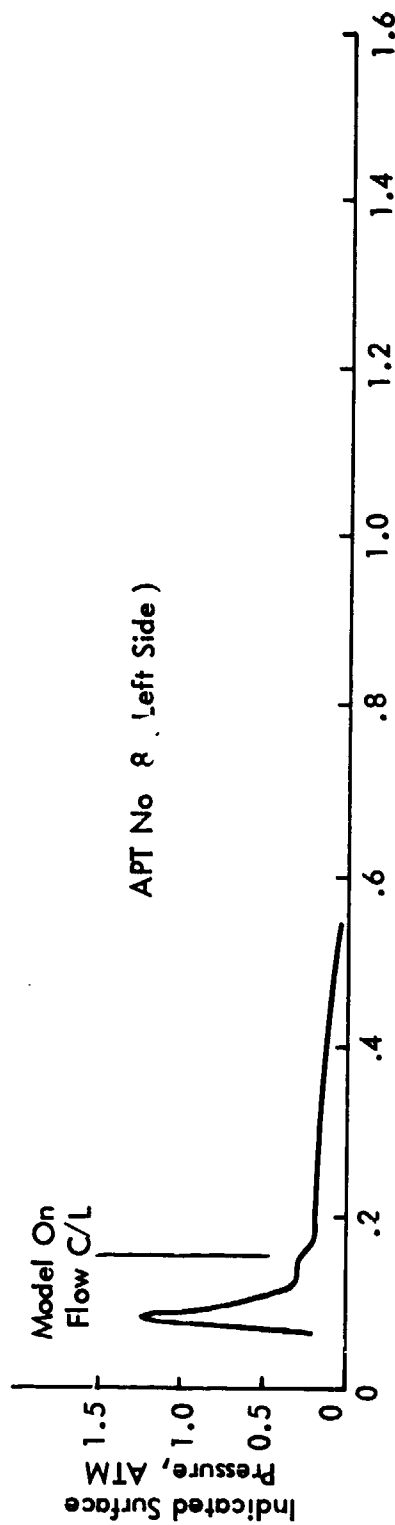


FIGURE 26 TEST RUN 1 APT DATA

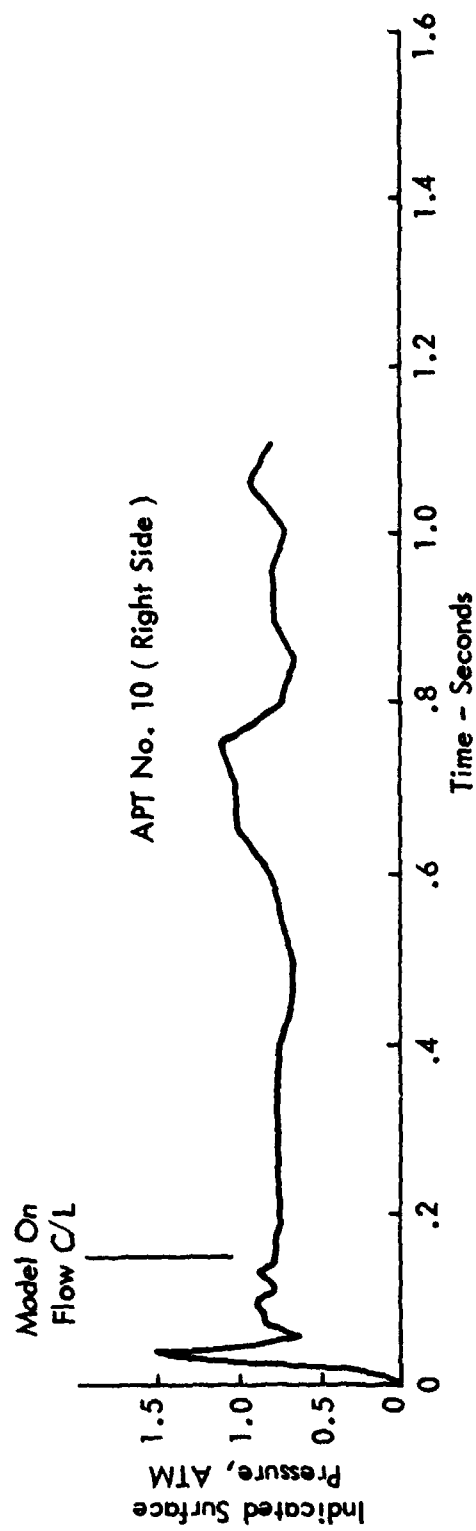
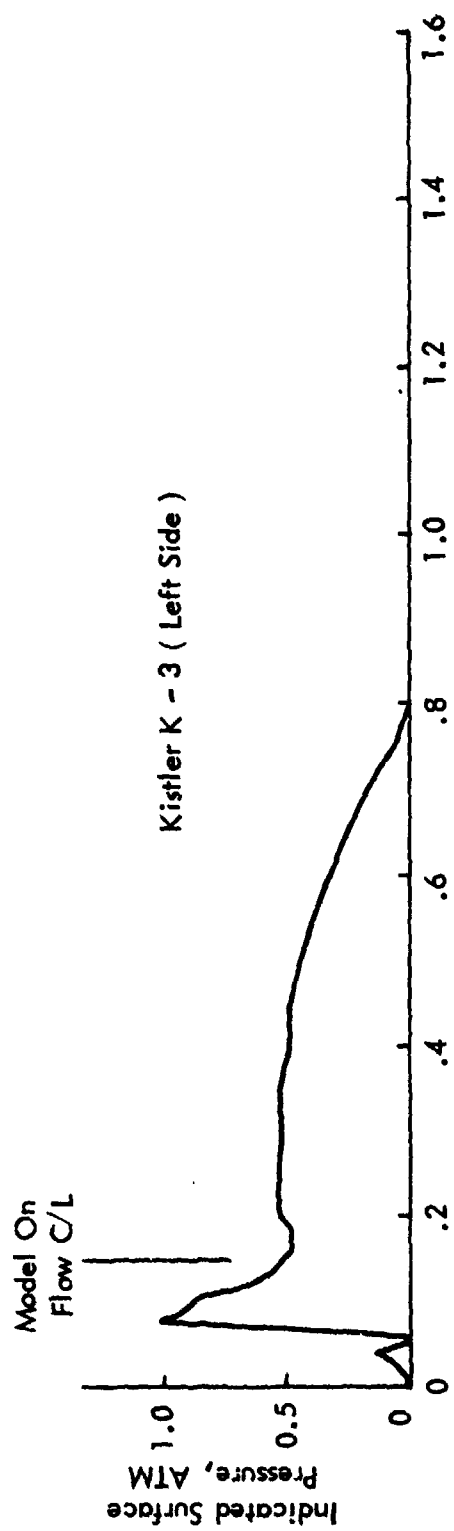


FIGURE 27 TEST RUN 1 APT DATA

- a) Maximum length data were obtained on APT numbers 6, 1, and 10 all of which had the silicone compound gap filler in common.
- b) All the other APT records exhibit a response to the barrel shock pressure spike followed by a rapid negative decrease in amplitude.
- c) Transducer number 7 (Figure 22) with air gap .0127 cm does not exhibit a rapid recovery from the barrel shock but has a the negative slope pressure trace as did the other air and fiber-filled gap APT's.
- d) The Kistler transducer K3 on sting 6 exhibits a normal chracteristic during the early portion of the test but also trails off with a negative slope caused by hot gases entering the housing.

The pressure traces of the three APT's with silicone gap filler are believed to be good representations of the model surface pressures. For a duration of approximately 0.6 seconds the level of these three records stays high and fairly steady. A comparison of the pressure measured by APT's 1, 6, and 10 plus Kistler K3 at 0.3 seconds in the run is shown in the following table. Kistler data from the calibration models are also listed.

<u>APT/Kistler No.</u>	<u>Pressure (atm)</u>	<u>Side of Holder</u>
1	.89	Right
6	1.16	Right
10	1.16	Right
K3	.51	Left
K1	0.29	Right
K2	0.34	Left
K4	0.29	Right
K5	0.52	Left

The APT's without the silicone compound insulating the diaphragm exhibited anomalous behavior, the principal feature being a negative slope. This characteristic is believed to be the result of the diaphragm being heated rapidly with a resulting deformation from mechanical expansion. The deformation was such as to cause the diaphragm to assume an arc which appeared in the output as a negative trending pressure. Figures 24 and 26 especially show this phenomenon. Two other transducers (numbers 7 and 9, Figures 23 and 26 respectively) showed a large positive pressure before going negative due to diaphragm heating. The cause of the large positive step is unknown at this time.

Additional insight into test conditions may be obtained by examination of still photographs taken at AEDC of the test hardware. These plots are included in Appendix D and show pre-test and post-test conditions. Of special interest is the gouging that occurred in the carbon-phenolic block at the center of the flow. The gouges appeared to exceed 0.25 cm in places but were non-uniform. Erosion on the plugs can also be seen and are an indicator of the wear which might be encountered in a flight test.

3.3.3 Test Run No. 2 Data

Thermal data obtained by the thermocouple calorimeters in cal blocks 1 and 2 are presented in Figures 28 and 29. From these data, heating rates were obtained with the models on flow centerline:

<u>Thermocouple No.</u>	<u>Heating Rate</u> <u>joules/cm²-sec</u>
T/C 1	1250
2	1450
3	2100
4	1450
5	1500
6	3300

Thermocouple locations were listed in the similar table in Section 3.3.2 for Test Run 1 data.

In this run the heating rate more uniformly increased from the point furthest from the center towards the center. T/C 3 and T/C 6 again demonstrated very high temperatures at the flame center having the highest heating rates.

Duration of the exposures was approximately 1.1 seconds and the resulting integrated heat on the APT plug center was 1650 ± 200 joules/cm² at a nominal 1500 joules/cm²-sec rate. The uncertainty is due to measurement inaccuracies.

Pressure calibration data obtained by the Kistler transducers are shown in Figures 30 and 31. Similar to the traces obtained during test run number 1, characteristic peak pressure lines were observed entering and leaving the flame. Flow centerline pressures also varied, having values as follows:

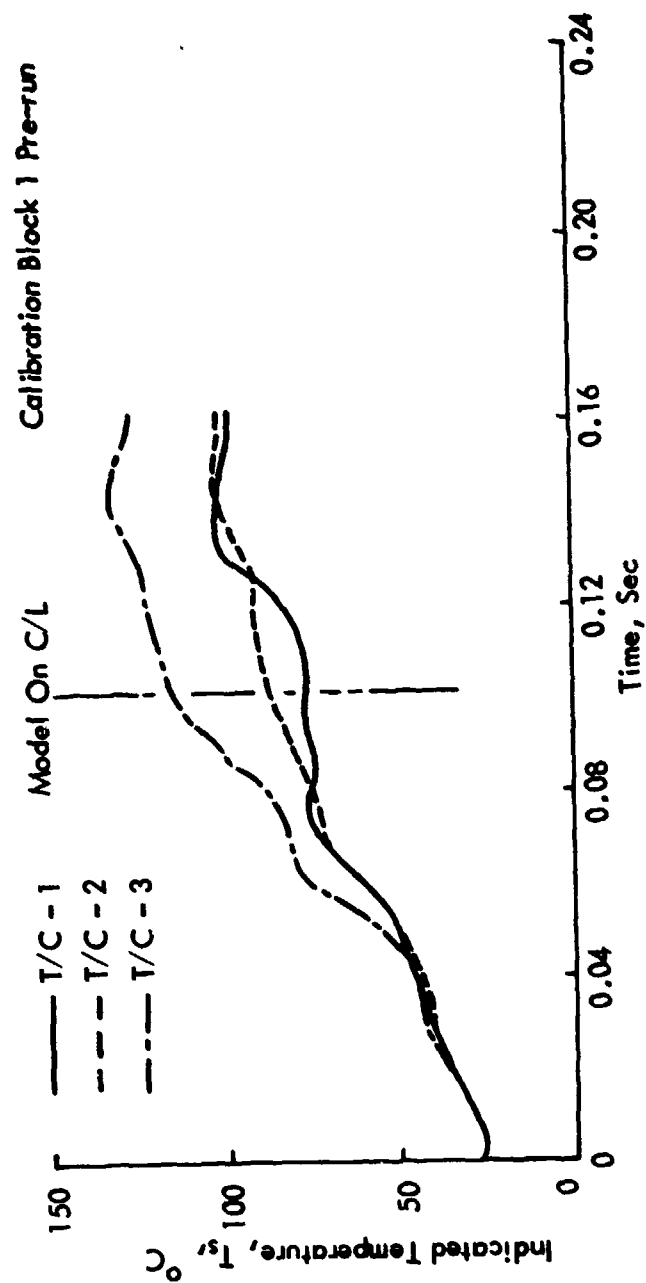


FIGURE 28 TEST RUN 2 CALIBRATION DATA-THERMAL

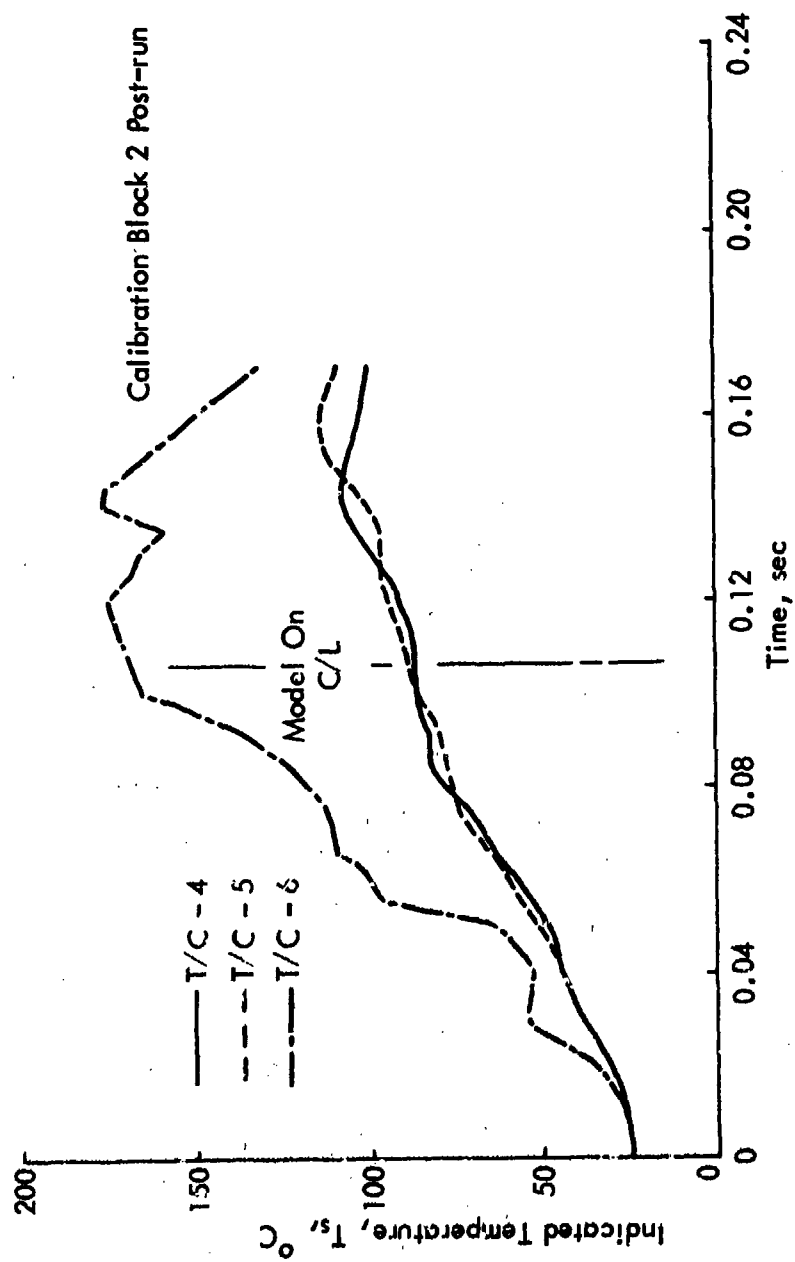


FIGURE 29 TEST RUN 2 CALIBRATION DATA-THERMAL

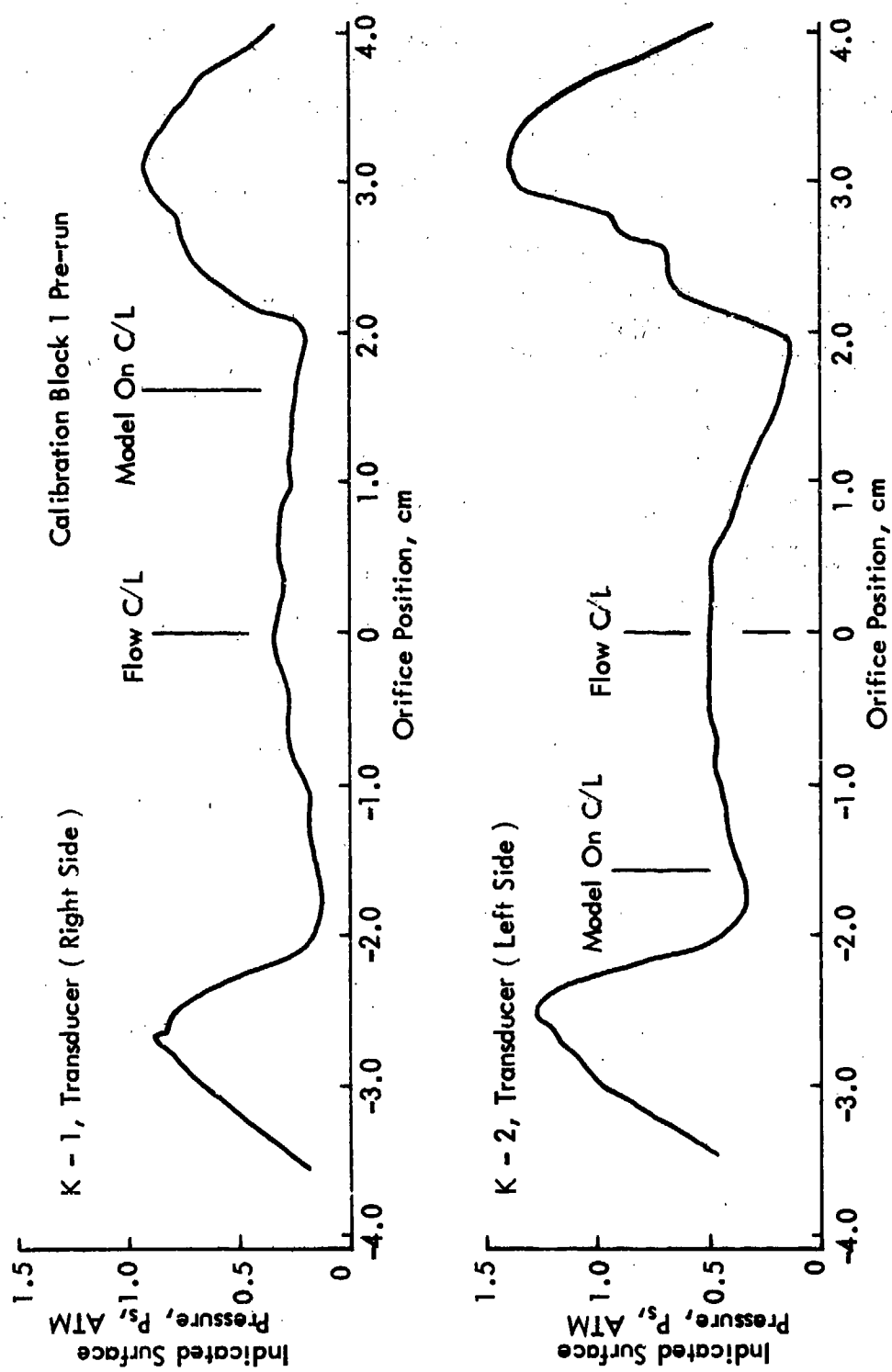


FIGURE 30 TEST RUN 2 CALIBRATION DATA - PRESSURE

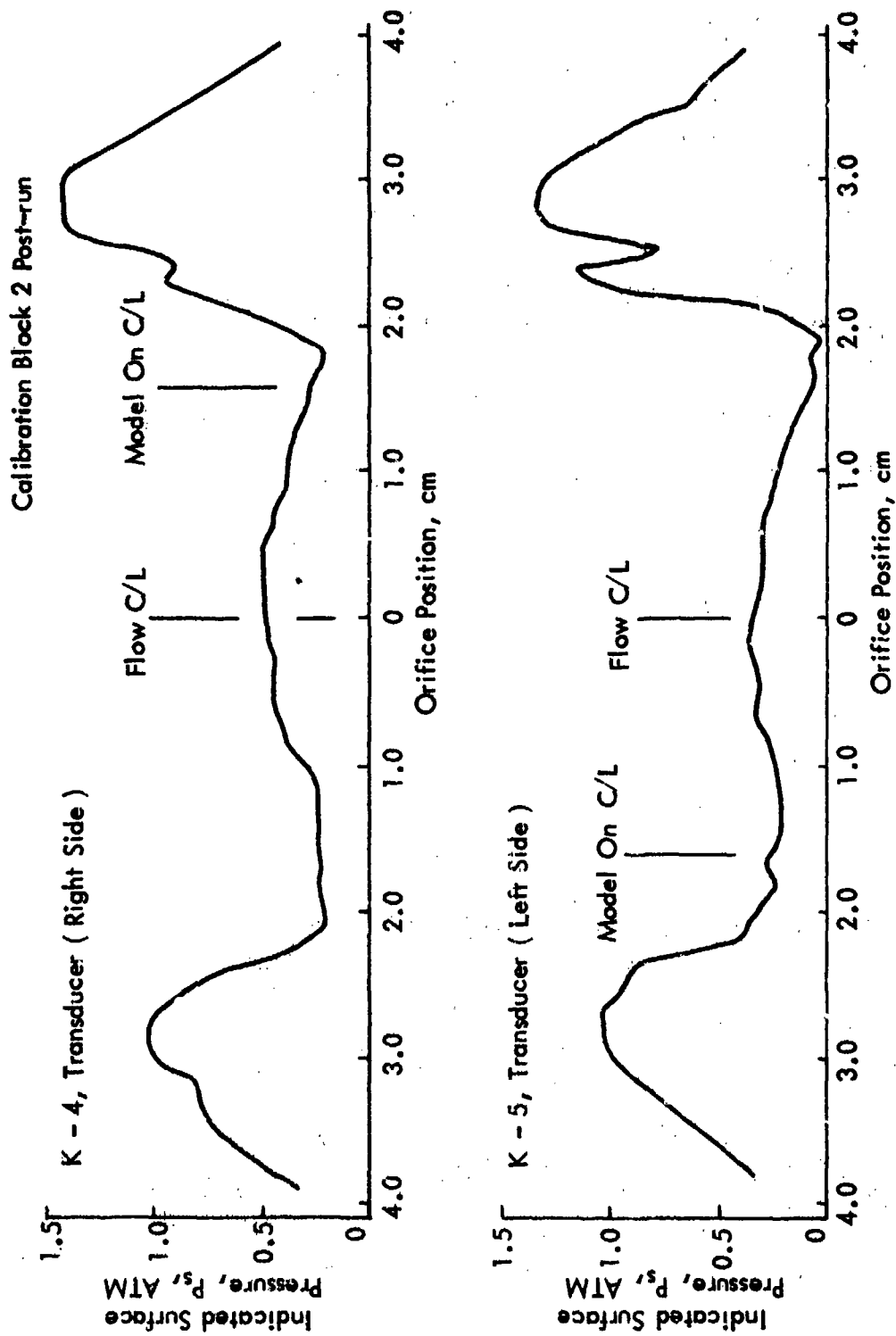


FIGURE 31 TEST RUN 2 CALIBRATION DATA - PRESSURE

K-1	.34 atm
K-2	.48
K-4	.50
K-5	.31

Plots of the APT data for Run 2 are shown in Figures 22, 33, and 34. These plots have the following features:

- a) An entrance and departure spike caused by the barrel shock around the heater flow.
- b) Amplitude levels holding nearly constant during the exposure duration of 1.1 seconds.
- c) Noise fluctuations which are correlated between channels and also to the arc current (not shown).

By obtaining a least squares fit to the portion of each trace between 0.2 and 1.2 seconds, the following parameters were obtained:

<u>Figure No.</u>	<u>Transducer No.</u>	<u>Slope (atm/sec)</u>	<u>Mean (atm)</u>	<u>Position</u>
32	2	.0172	0.83	R
32	5	.0308	0.75	L
33	4	-.0251	1.03	R
33	13	.136	0.87	L
34	3	.290	0.61	R
34	14	.0673	0.78	L

Comparable calibration data from the Kistler transducers is as follows:

30	K-1	0.24	R
30	K-2	0.37	L
31	K-4	0.31	R
31	K-5	0.21	L

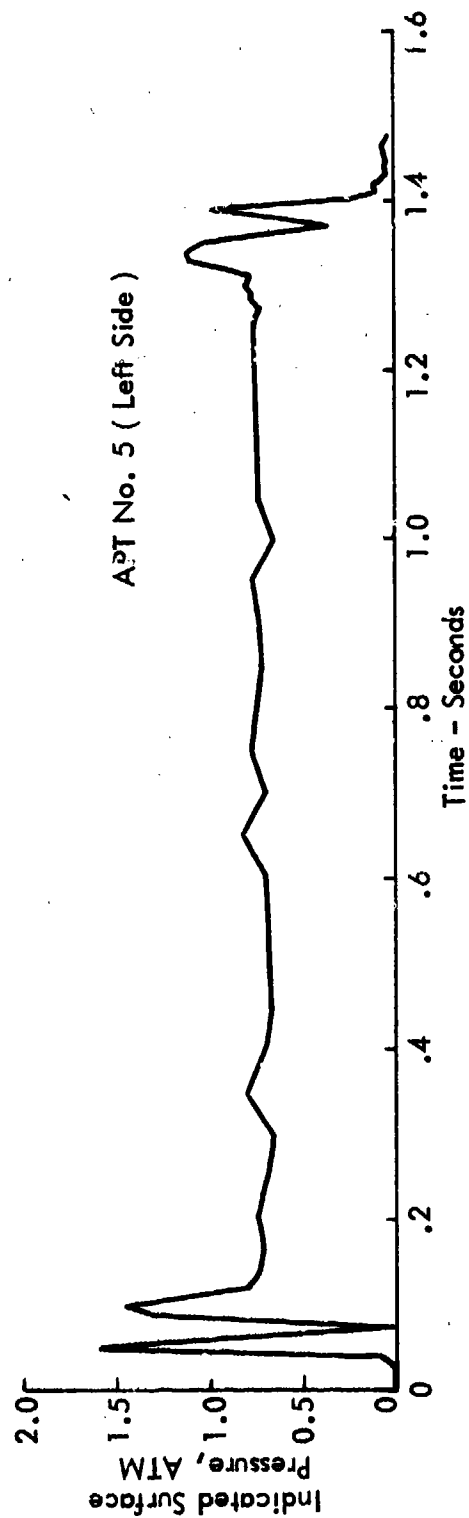
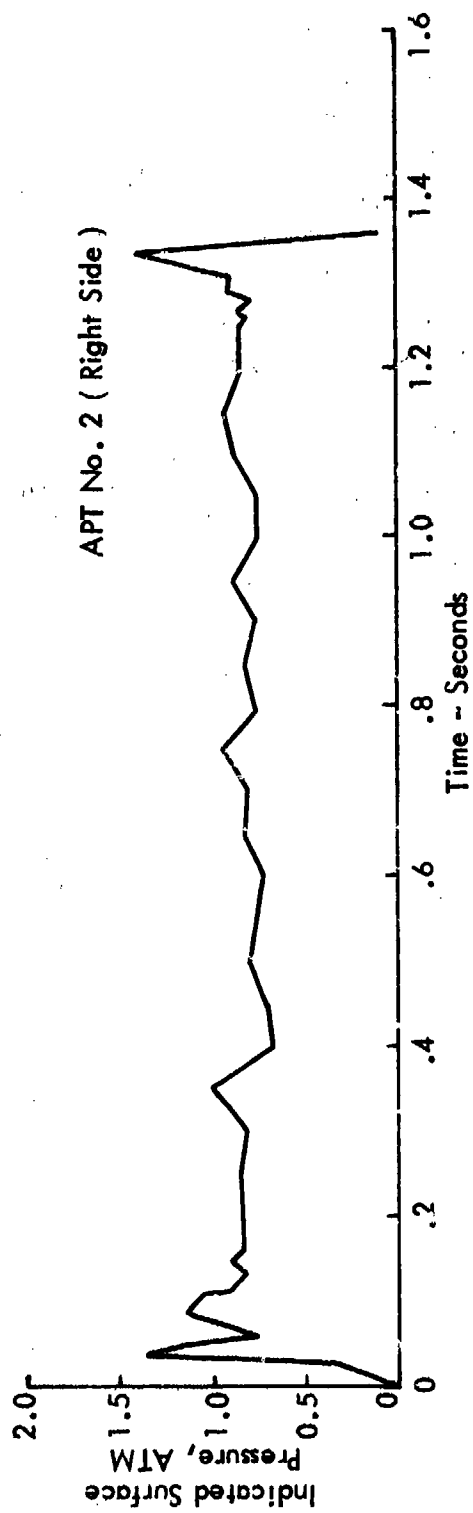


FIGURE 32 TEST RUN 2 APT DATA

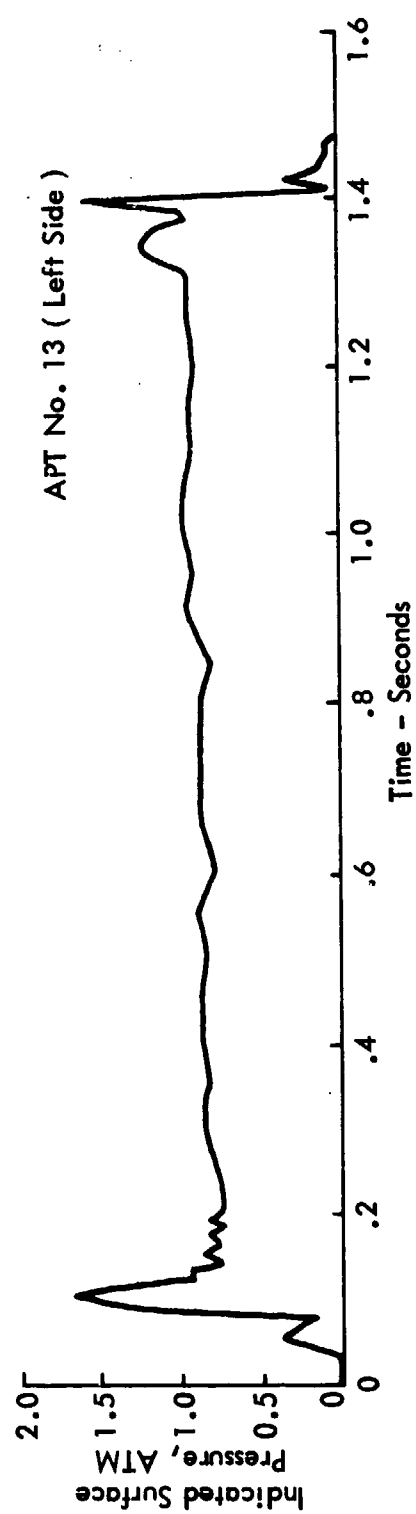
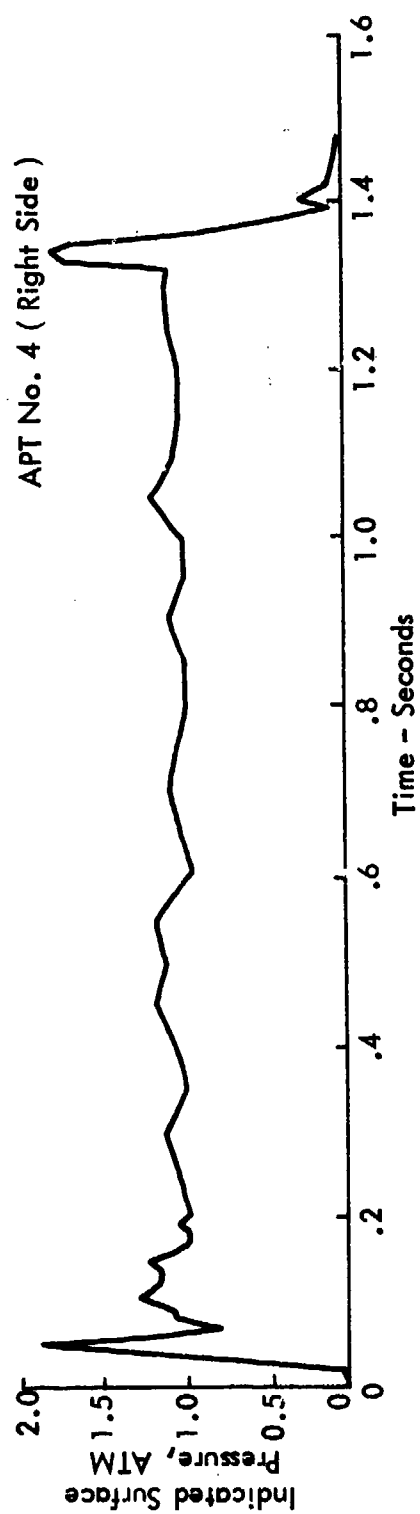
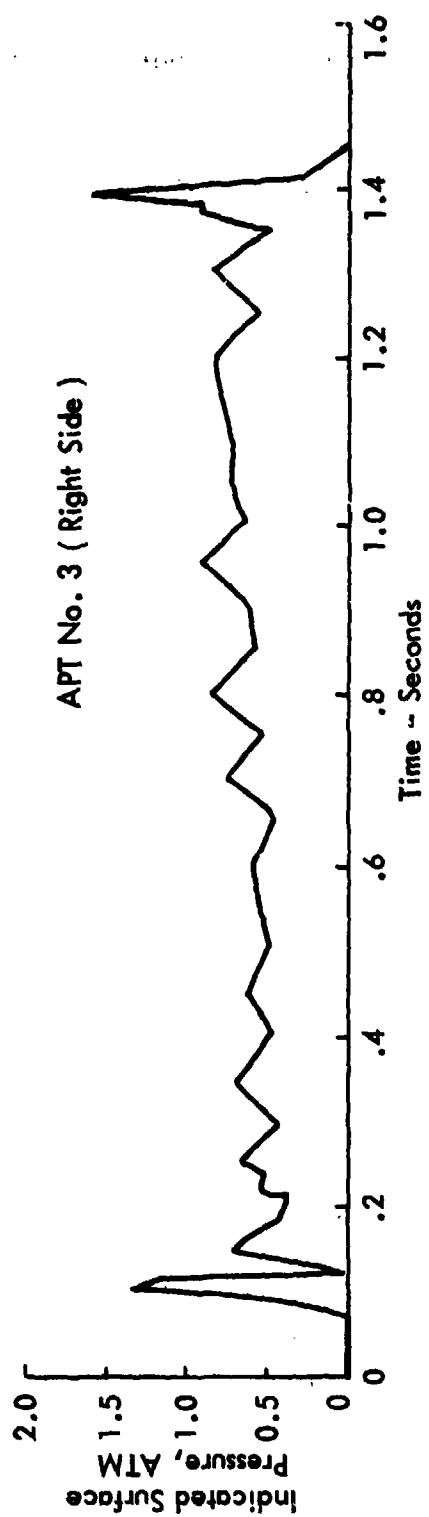


FIGURE 33 TEST RUN 2 APT DATA



72

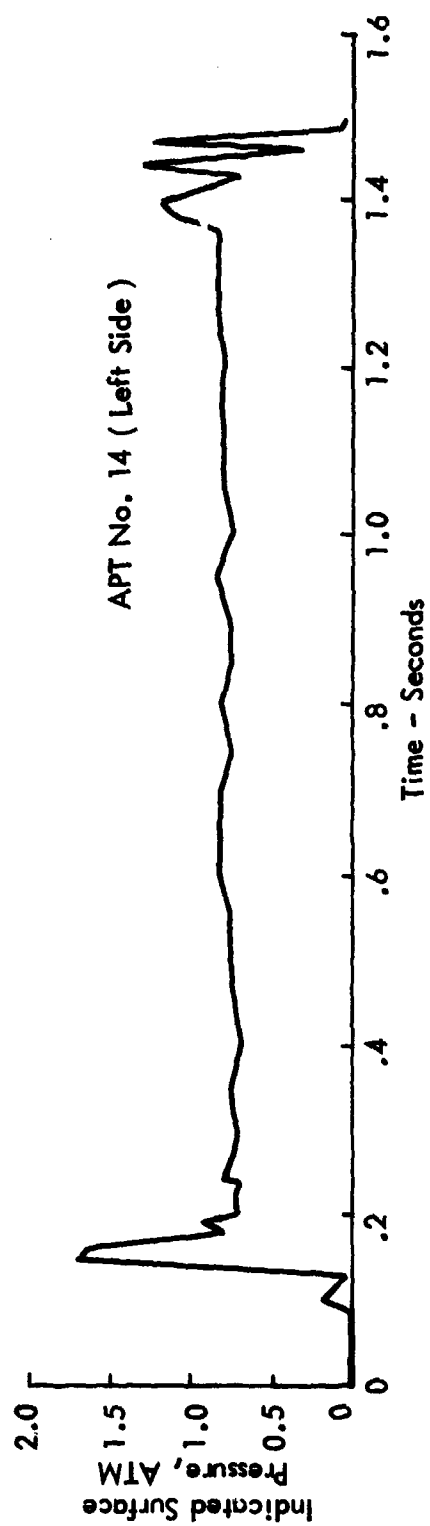


FIGURE 34 TEST RUN 2 APT DATA

The Kistler data are taken at the point where the model is on the flow centerline.

It is immediately noticeable that the amplitude between the calibration and APT's differ considerably but that the percentage spread within each group is similar. The calculated value of surface pressure due to this type of flow is closer to the lower pressures measured by the orifice transducers. This calculation, however, is dependent on knowledge of the flow incident angle on the surface, gas characteristics, and other factors which can only be approximated.

Several reasons can be advanced for the APT measurement being higher than the Kistler value:

- a) The APT responds to a pressure across a surface 1.27 cm in diameter. It can be noted from Figures 31 and 32 that the Kistlers are measuring the lowest pressure on the profile at the instant the model is on flow centerline. An APT centered the same position extends across the low pressure saddle and thus should record a higher pressure.
- b) Some uncertainty exists as to the net effects of pressure and flow in the gap because the dimensions of this APT gage are not ideal with respect to cancellation of pressure in the gap-diaphragm zone.
- c) The flow incident angle changes rapidly across the plug surface; i.e., the angle is larger at the edge of the gap closest the flow centerline. This leads to a very complex flow which cannot be estimated readily by straightforward aerodynamic calculations.

- d) The reading obtained by the Kistler gages is lower than the actual surface pressure due to the well known interaction of static pressure ports with boundary layer flows⁷.

The slopes during the test experienced by transducers 13 and 3 cannot be explained readily. The traces show a fairly sudden change in level during the test which might indicate plug ablation or flow change rather than transducer drift.

Photographs of test models both during and after the run are included in Appendix E.

3.3.4 Test Run No. . Data

Thermal calibration data are plotted in Figures 35 and 36 from which heating rate data to the centerline position were obtained as follows:

<u>Thermocouple No.</u>	<u>Heating Rate</u> <u>joules/cm²-sec</u>
1	1250
2	1450
3	2200
4	1350
5	1450
6	3100

As in the previous test runs, the heating rate was much higher closer to the center of the flow. Evidence of this higher rate is also evidenced by the gouging which occurred in the area on test models at the center of the arc flow (reference photos in Appendices D, E, F).

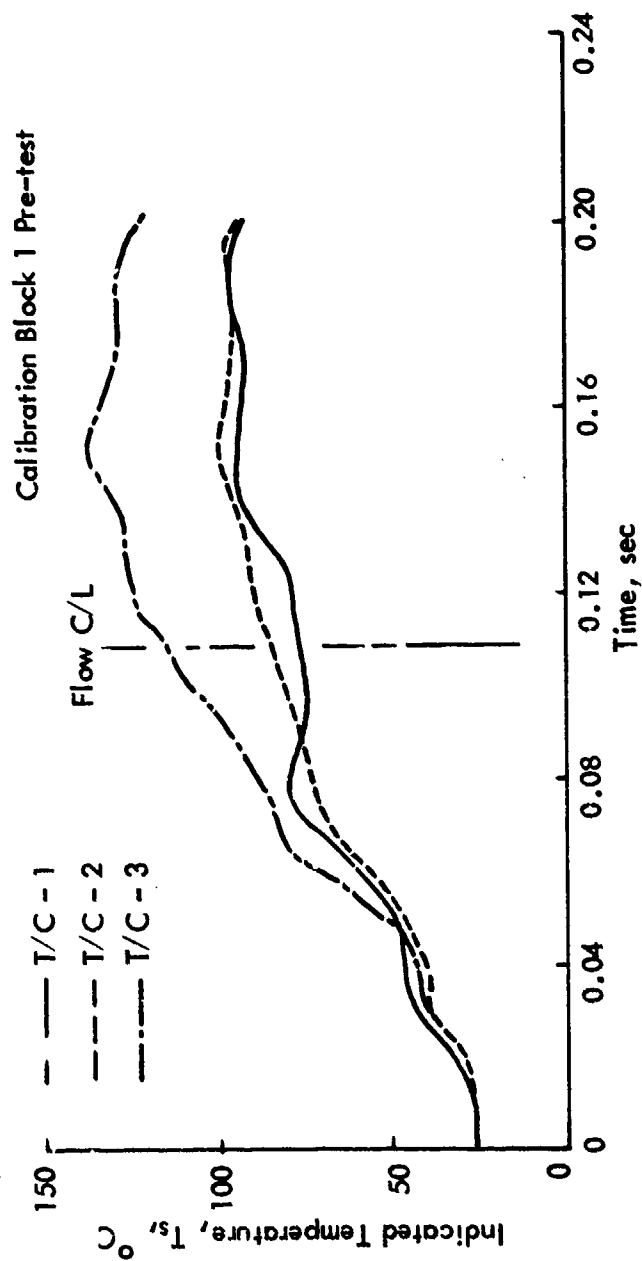


FIGURE 35 TEST RUN 3 CALIBRATION DATA-THERMAL

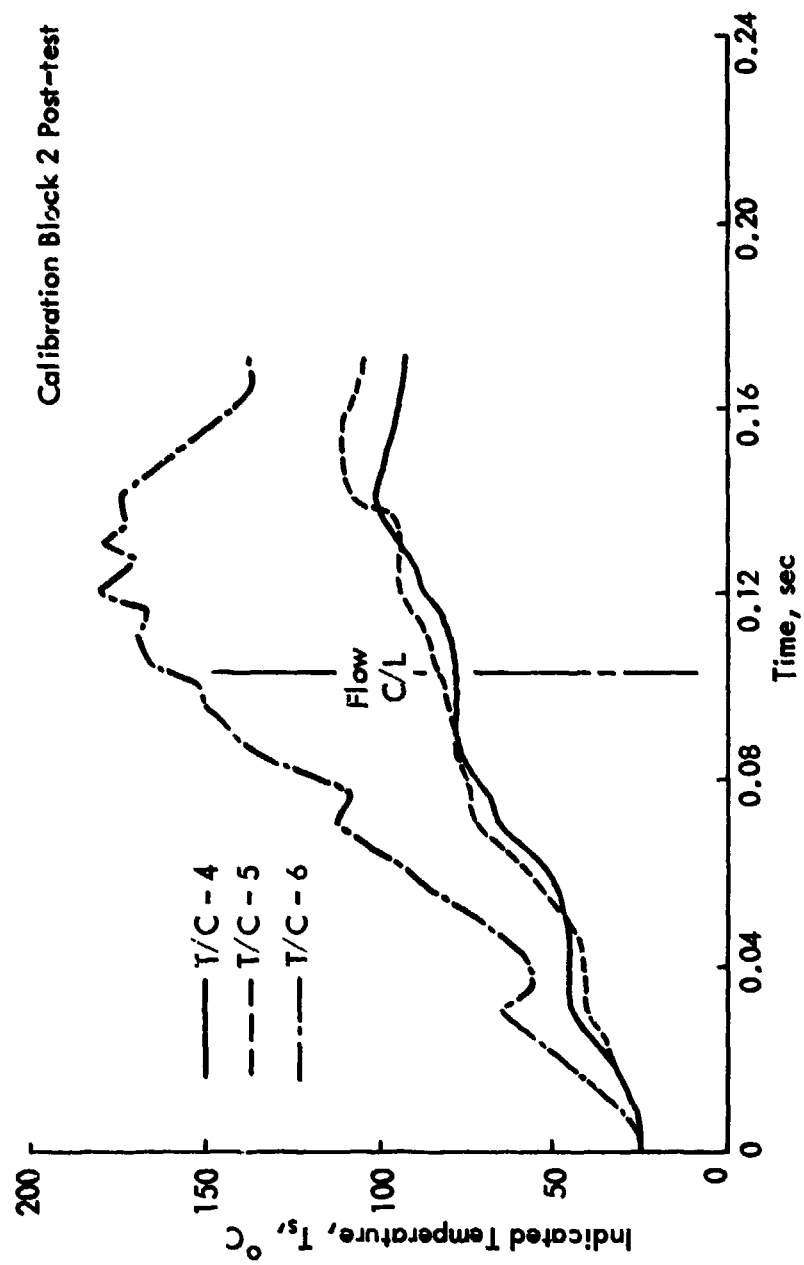


FIGURE 36 TEST RUN 3 CALIBRATION DATA-THERMAL

Pressure calibration data for Test 3 are given in the traces of Figures 37 and 38 which are similar to the comparable data from the previous two runs. Flow centerline pressure levels are as follows:

K-1	.34 atm
K-2	.37
K-4	.35
K-5	.34

These readings are much more uniform than those obtained in Tests 1 and 2.

Plots of the APT sensor readings are given in Figures 39, 40, and 41. These plots exhibit characteristics similar to those observed in the Test Run 2 data. APT No. 5 (Figure 38) amplitude dropped severely during the run. Afterward it was found that the transducer had not been sealed to the carbon phenolic block, thus allowing hot gas to leak past the diaphragm. The level during the first 0.4 seconds of the record is regarded to be good data.

Using a line which is a least-squares fit to the portion of each trace between 0.2 and 1.8 seconds, the following parameters were obtained:

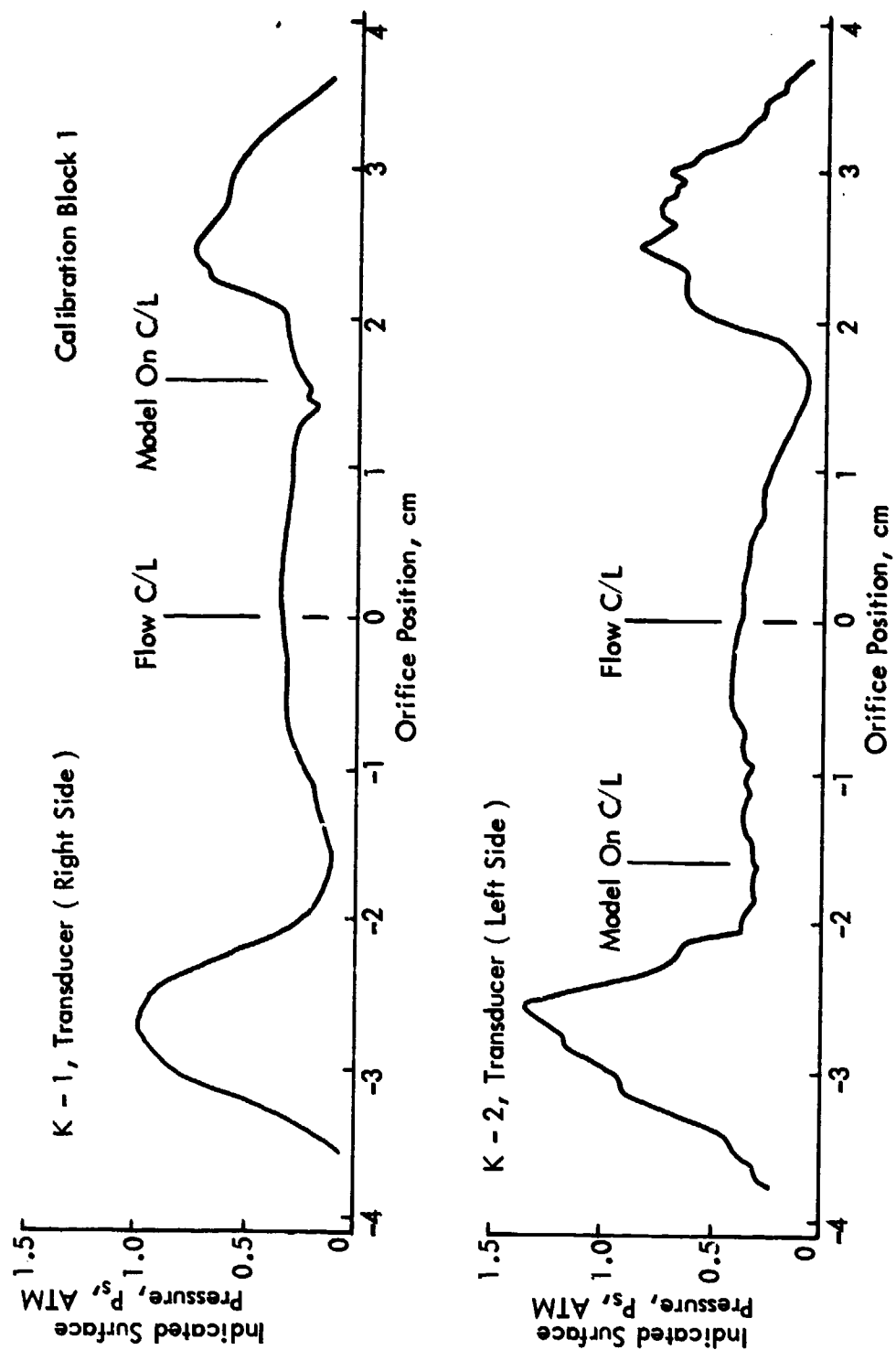


FIGURE 37 TEST RUN 3 CALIBRATION DATA-PRESSURE

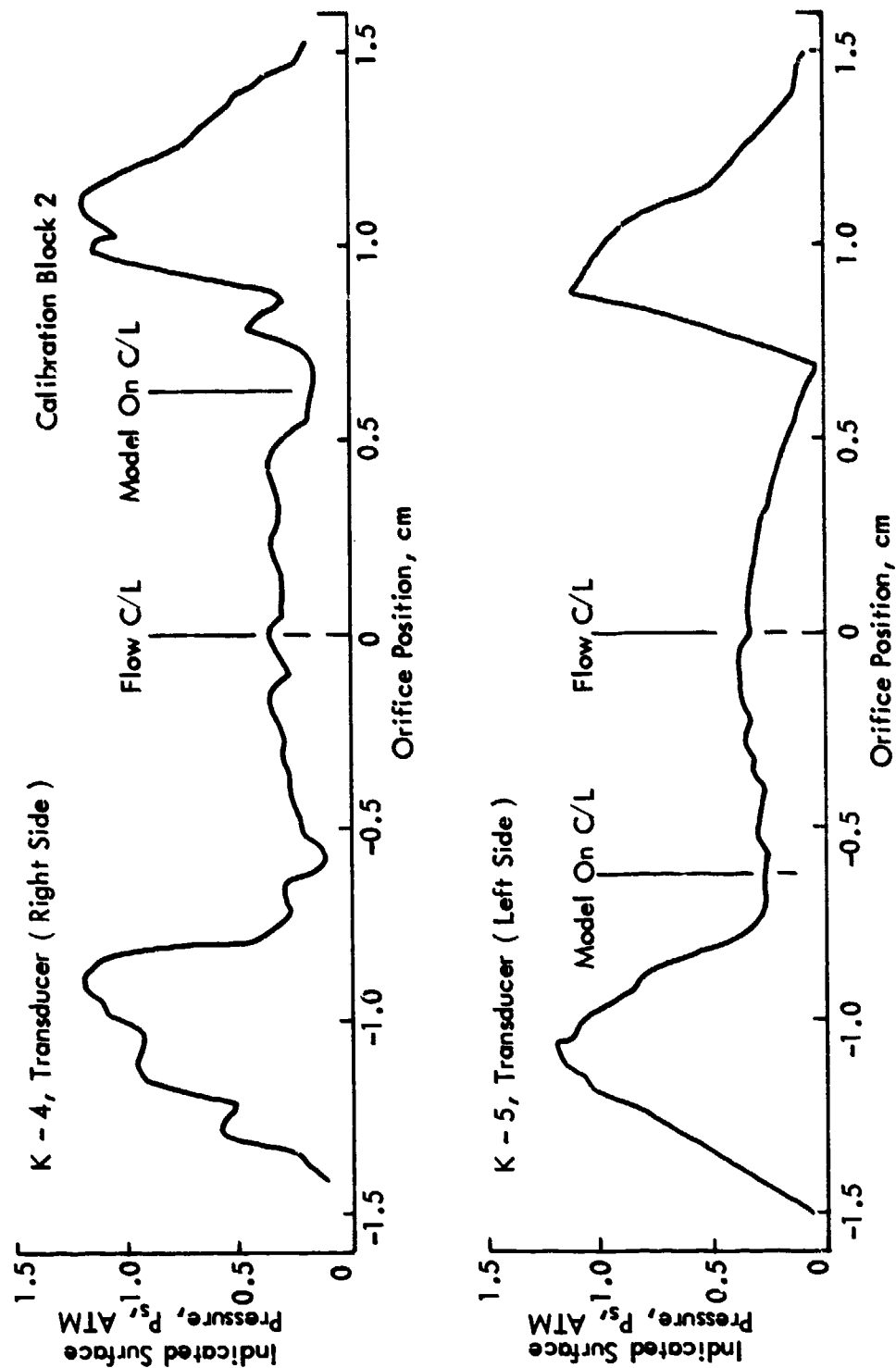


FIGURE 38 TEST RUN 3 CALIBRATION DATA-PRESSURE

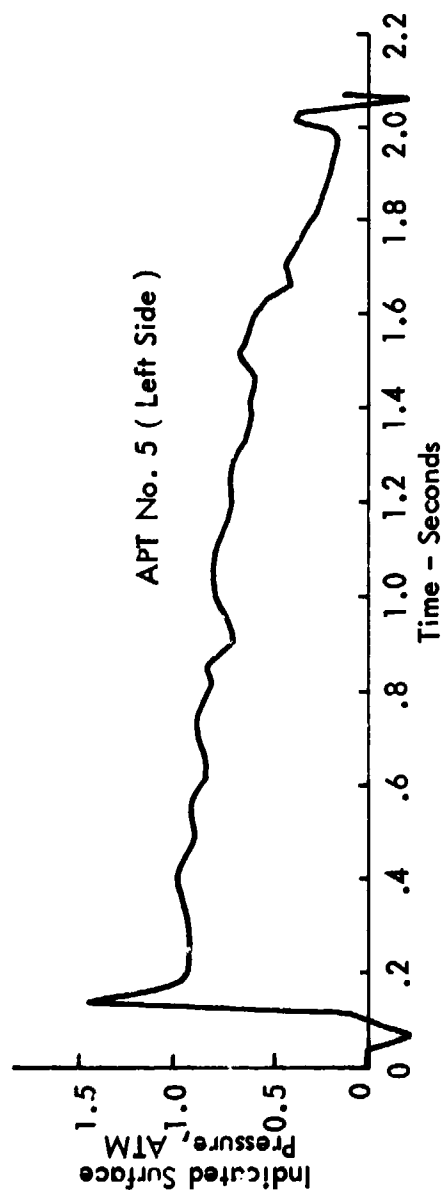
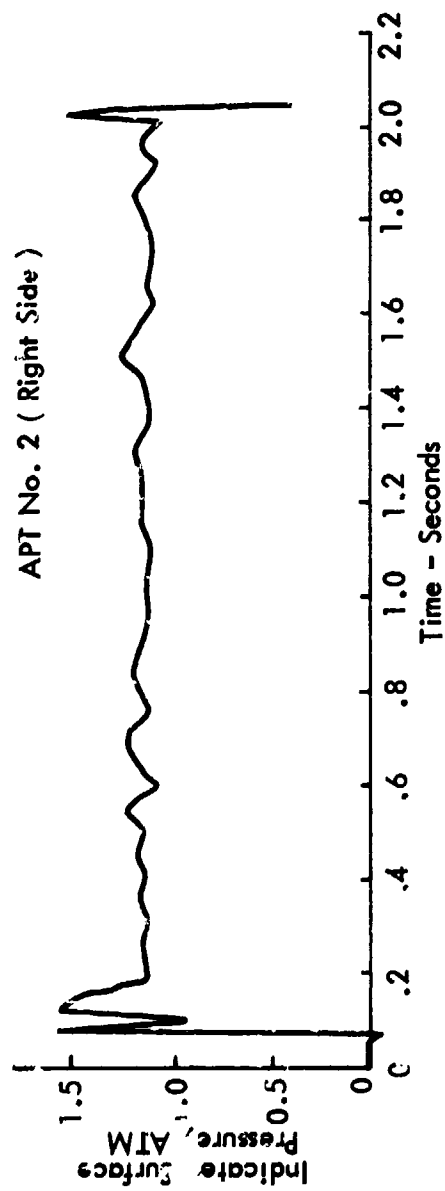


FIGURE 39 TEST RUN 3 APT DATA

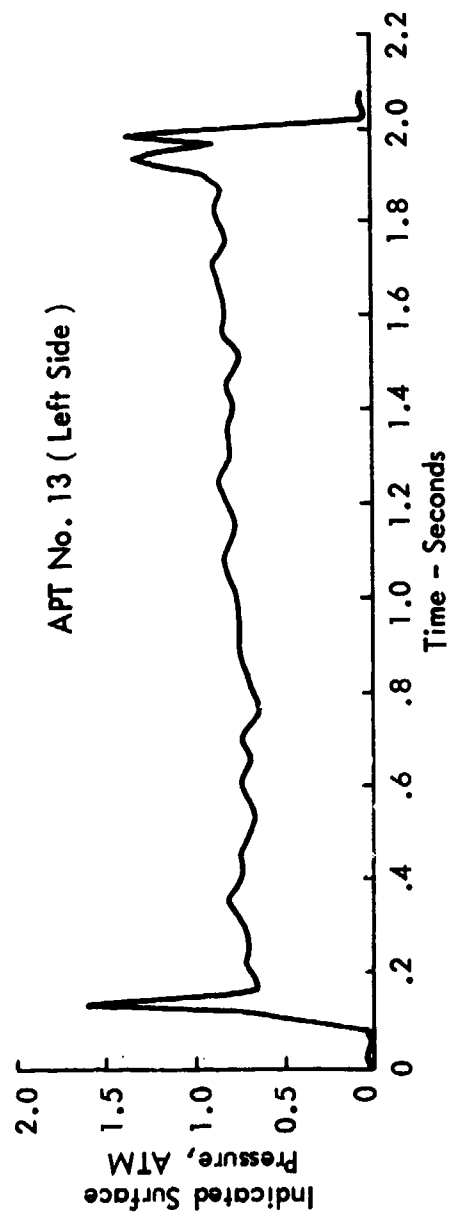
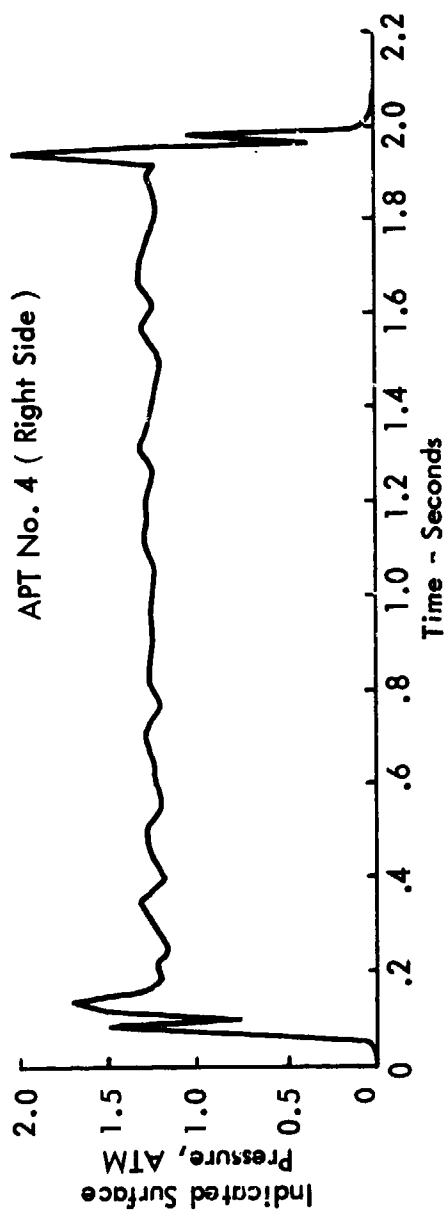


FIGURE 40 TEST RUN 3 APT DATA

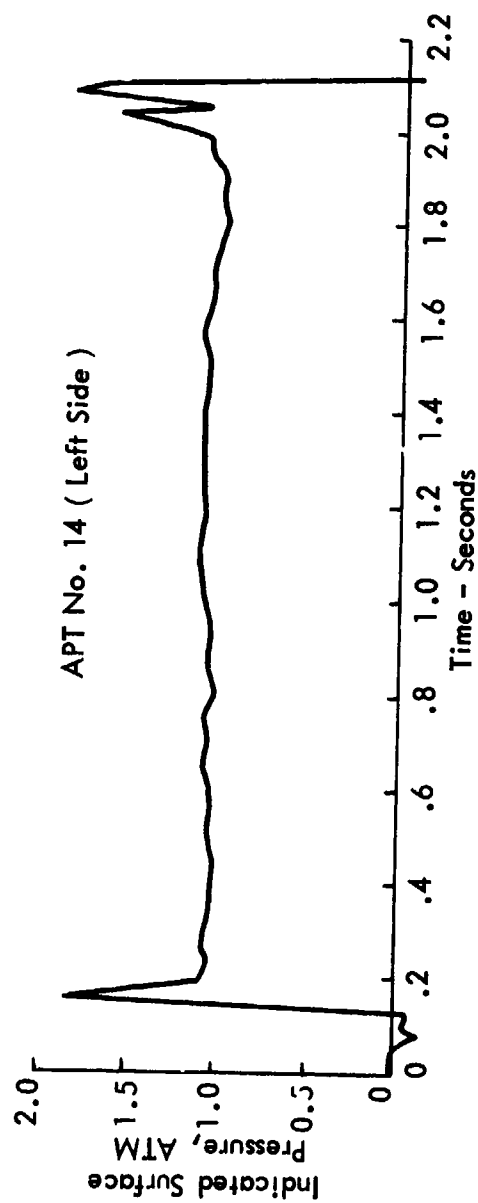
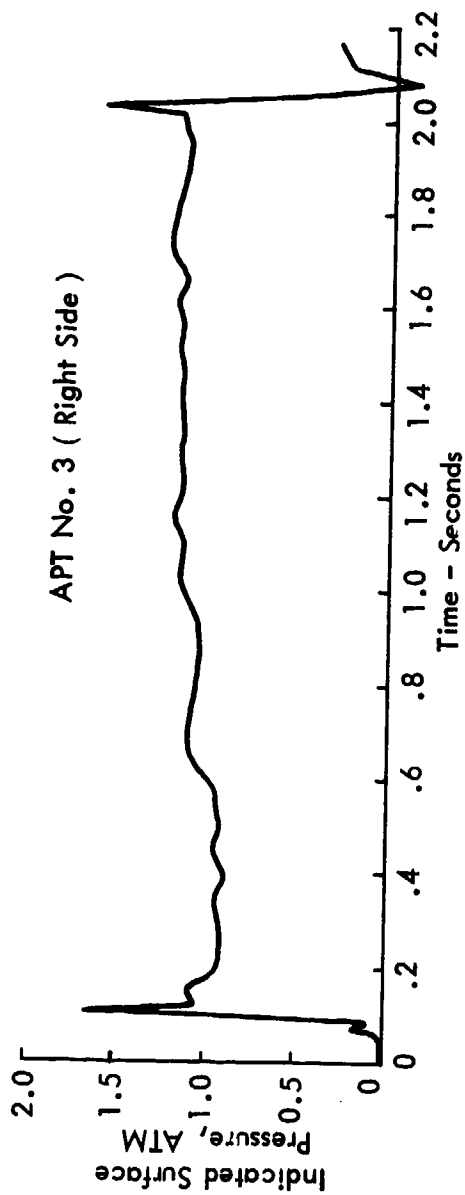


FIGURE 41 TEST RUN 3 APT DATA

<u>Figure No.</u>	<u>Transducer No.</u>	<u>Slope (atm/sec)</u>	<u>Mean (atm)</u>	<u>Position</u>
39	2	-.0023	1.14	R
39	5	N/A	0.92	L
40	4	.016	1.10	R
40	13	.097	0.77	L
41	3	.21	1.04	R
41	14	.011	1.07	L

Data from the calibration block transducers in the same position as the APT's are as follows:

37	K-1	0.27	R
37	K-2	0.31	L
38	K-4	0.14	R
38	K-5	0.27	L

With the exception of APT No. 13, there is low scatter in the measured pressure. As in test 2, transducers 13 and 3 exhibited a fairly high positive slope during the test, an explanation for which is not readily obvious. The pressures recorded by the APT's were again much higher than the comparable measurement by the Kistlers in the calibration blocks. Again, we have no ready explanation for the difference (reference Section 3.3.3 for a discussion of possible reasons).

Photographs of the test models both during and after the run are included in Appendix F.

3.4 DISCUSSION OF ARC HEATER TEST RESULTS

The arc heater experiment was designed to test the APT in an environment similar to that experienced during ICBM reentry. The data obtained, presented in the preceding sections, permit an evaluation of how closely the goals were achieved.

The transducer pressure plots from the three runs have demonstrated that the APT is capable of measurement of wall pressure with consistency, although the fluctuating dynamic conditions existing with the flow field made it virtually impossible to obtain a good calibration with which to compare the data. The principal problem in the calibration was that the ported transducer pressures were a factor of two or three lower than the APT indicated pressures, probably due to flow-field interaction with the ports causing low readings, while the area of the APT plug resulted in higher pressures. The APT plug extended into the barrel shock region a significant amount as was observed in the motion picture data showing higher surface temperature across the edge of the plugs. (See photos, Appendices E and F.)

The environment produced by the arc heater simulated that of reentry in several aspects. Heating rate and direction of flow across the transducer were approximately the same as in flight. Test durations were long enough to simulate to altitudes well below transition with respect to total heat input. Comparisons were made by using the thermal calibration data from each run and comparing with conditions on a typical reentry body as computed for four trajectories with ARROW and REKAP programs. The computed environments have been summarized in the plots in Appendix C.

Table 6 is a summary of the arc heater test conditions compared with those of the maximum conditions extracted from the calculations plotted in Appendix C. Data are shown for Test 2 and Test 3, which provided more complete data than did Test 1.

TABLE 6 ARC HEATER TEST - SIMULATION COMPARISON

	\dot{Q} JOULES/CM ² -SEC	DURATION (SEC)	\dot{Q} JOULES/CM ²	% OF ICBM TOTAL	SIMULATION ALTITUDE (KM BELOW TRANSITION)			
					1*	2*	3*	4*
Test 2	1500	1.1	1650	10-16	-4.6	-7.6	-3.0	-4.0
Test 3	1450	1.8	2610	12-26	-6.4	-10.0	-4.6	-6.11

*Trajectory Data

#	VELOCITY (MPS)	REENTRY ANGLE
1	7711	-40°
2	6401	-40°
3	7605	-20°
4	7010	-30°

The data in Table 6 show that the equivalent test altitude in all cases was below transition for all four trajectories, thus permitting the conclusion that most of the test goals were achieved.

In addition, an examination of the post-test hardware from Test 2 and Test 3 shows that gap filler was still functioning and that gap edge erosion was moderate (see photos in Appendix E and Appendix F). It is believed that the APT in the test configuration would have survived a longer test interval than was actually used in Test 3 (1.8 seconds) because the hardware condition was good where the APT was installed. It can be noted from the photos that severe gouging occurred where the arc heater flow was impinging the carbon-phenolic blocks on the aft face of the layup; this is a condition which never occurs in a flight test.

SECTION 4

SUMMARY AND CONCLUSIONS

The APT was designed, developed and tested with success in a Mach 5 ablating environment. The transducer utilizes a pressure diaphragm with a balance guard ring capacitive sensing technique (Reference Figure 6). By correct sizing of the plug and diaphragm diameter, errors due to gap differential pressures are eliminated, providing a unique measurement capability.

A circuit was developed to excite the sensor and to condition the sensor output signal for recording purposes. An amplitude stabilized dual-feedback oscillator, and an op-amp output circuit are included in the circuit. A single coaxial cable connects the sensor and circuit; both excitation and d.c. return signal are carried by the cable (Figure 7).

The APT design successfully included an acoustic monitor sensor which proved to be highly responsive to surface noise generated by the arc heater in the AEDC test.

The arc heater test was designed to test the APT in an installation similar to that which would be used on an R/V. Excellent pressure profiles were obtained in the tests after some initial hardware problems were corrected. The pressure readings from the APT's were consistently higher by a factor of two or three than ported calibration gages; this is believed to be due to the broader sensing area of the APT.

The environment heating rate simulation in the arc heater test was comparable to reentry values. Total integrated heat on the test models ranged up to 26% of a total reentry trajectory. Simulated altitudes were as much as 10 KM below heatshield

boundary layer transition altitude (reference Section 3.4).

Thus, this program demonstrated the feasibility of the APT concept to measure static pressure and monitor dynamic pressure at altitude levels below normal transition altitude.

It is believed that additional design and testing activities to minimize flow field interactions with the transducer-heatshield gap would substantially reduce the altitude of applicability of the APT.

REFERENCES

1. Nickell, J., et al, "An Evaluation of Boundary Layer Forces and Measurement Methods," DNA 4202F, October 1976.
2. Nickell, J., et al, unpublished material.
3. Kawecki, E. J., "An Analysis of Impingement Mode Ablation Testing," G.E. Company Document No. 9154-TDM-75-016, September 15, 1975.
4. Patton, J. B., Lewis, H. F., and Henson, J. R., "AFWL Carbon-Carbon Material Test," AEDC-DR-75-89, September 18, 1975.
5. "Equations, Tables, and Charts for Compressible Flow," Ames Research Staff, NACA Report 1135, 1953.
6. Henson, J. R., "Performance Test of the DNA-APT Transducer in an Ablation Environment," AEDC-DR-77-36, May 9, 1977, SEDC, Arnold AFS, TN.
7. Franklin, R. E., and Wallace, J. M., "Absolute Measurements of Static-Hole Error Using Flush Transducers," J. Fluid Mechanics, 1970, Vol. 42, Part 1, pp 33-48.

APPENDIX A
FORCE ANALYSIS ON APT PLUG/DIAPHRAGM

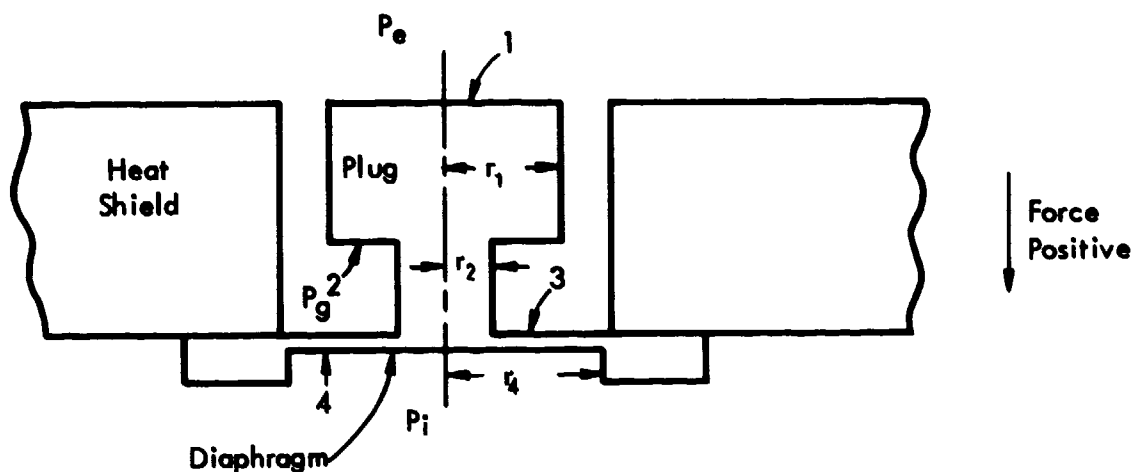


FIGURE 42 DIAPHRAGM ANALYSIS DIAGRAM

Forces which cause the diaphragm to deflect result from the external pressure, P_e , the gap pressure P_g , and the internal pressure, P_i . P_e is effective on surfaces labeled 1, 2, and 3 where 1 is the external plug surface, 2 is the undercut shoulder surface on the plug and 3 is the external diaphragm surface. These forces are opposed by the internal diaphragm pressure on surface 4. With circular geometry the summation of forces is

$$\sum F = 0 = P_e A_1 - P_g A_2 + P_g A_3 - P_i A_4 - F_k$$

where F_k is the restoring spring force of the diaphragm which opposes any net pressure force.

The respective areas are

$$\begin{aligned} A_1 &= \pi r_1^2 \\ A_2 &= \pi (r_1^2 - r_2^2) \\ A_3 &= \pi (r_4^2 - r_2^2) \\ A_4 &= \pi r_4^2 \end{aligned}$$

PREVIOUS PAGE NOT FILLED
PAGE.

Substituting the expressions for area into the force equation yields

$$0 = \pi r_1^2 P_e + \pi [r_4^2 - r_1^2] P_g - \pi r_4^2 P_i - F_k$$

For the majority of cases, $P_e = P_g$ and the external force on the diaphragm is proportional only to r_4 . If, however, a transient external pressure occurs and the gap conductance is low, a temporary condition may occur where $P_e \neq P_g$, in which case the equation applies as written.

The diaphragm response constant F_k , may be analyzed as the response of a circular flat plate with a center post. Values of deflection have been tabulated¹ for disks with varying ratios of r_4 and r_2 under different loading conditions.

Loading Condition 1: Load Transmitted to Diaphragm by Center Post

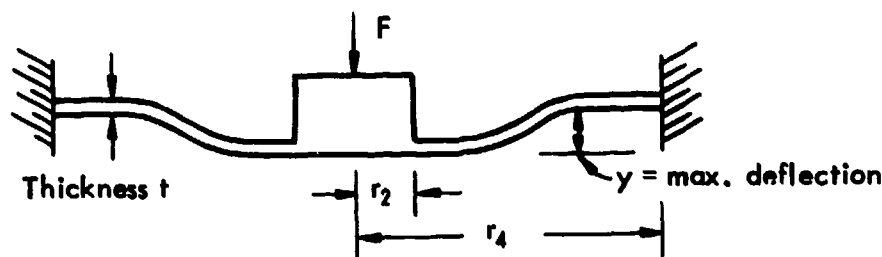


FIGURE 43 DIAPHRAGM FLEXURE

Force required for a given maximum deflection is

$$F = \pi r_1^2 P_e - \pi (r_1^2 - r_2^2) P_g = \frac{y_{mp} E t^3}{K_p r_4^2} = \frac{(y_{m1} - y_{m2}) E t^3}{K_p r_4^2}$$

¹Griffel, Wm., "Handbook of Formulas for Stress and Strain," Fredrich Ungar Publishing Co., New York, 1966.

where E = Material modulus of elasticity
 K_p = Constant depending on ratio r_4/r_2
 plotted in Figure 45
 y_{mp} = Maximum deflection due to forces on
 port
 y_{m1} = Deflection due to P_e
 y_{m2} = Deflection due to P_g

Loading Condition 2: Load is Uniformly Distributed on Diaphragm Only

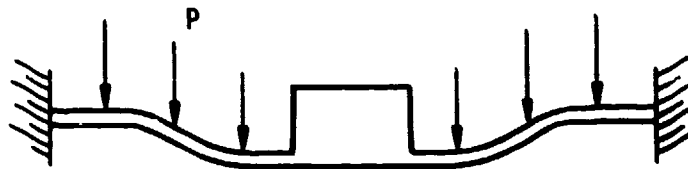


FIGURE 44 PRESSURE DISTRIBUTION

Force required for maximum deflection is

$$F = P_g (\pi) (r_4^2 - r_2^2) = \frac{y_{md} E t^3}{K_d r_4^2}$$

y_{md} = Maximum deflection due to pressure on diaphragm

K_d versus r_4/r_2 is plotted in Figure 46.

Assuming that the internal pressure $P_i = 0$ and superimposing the forces

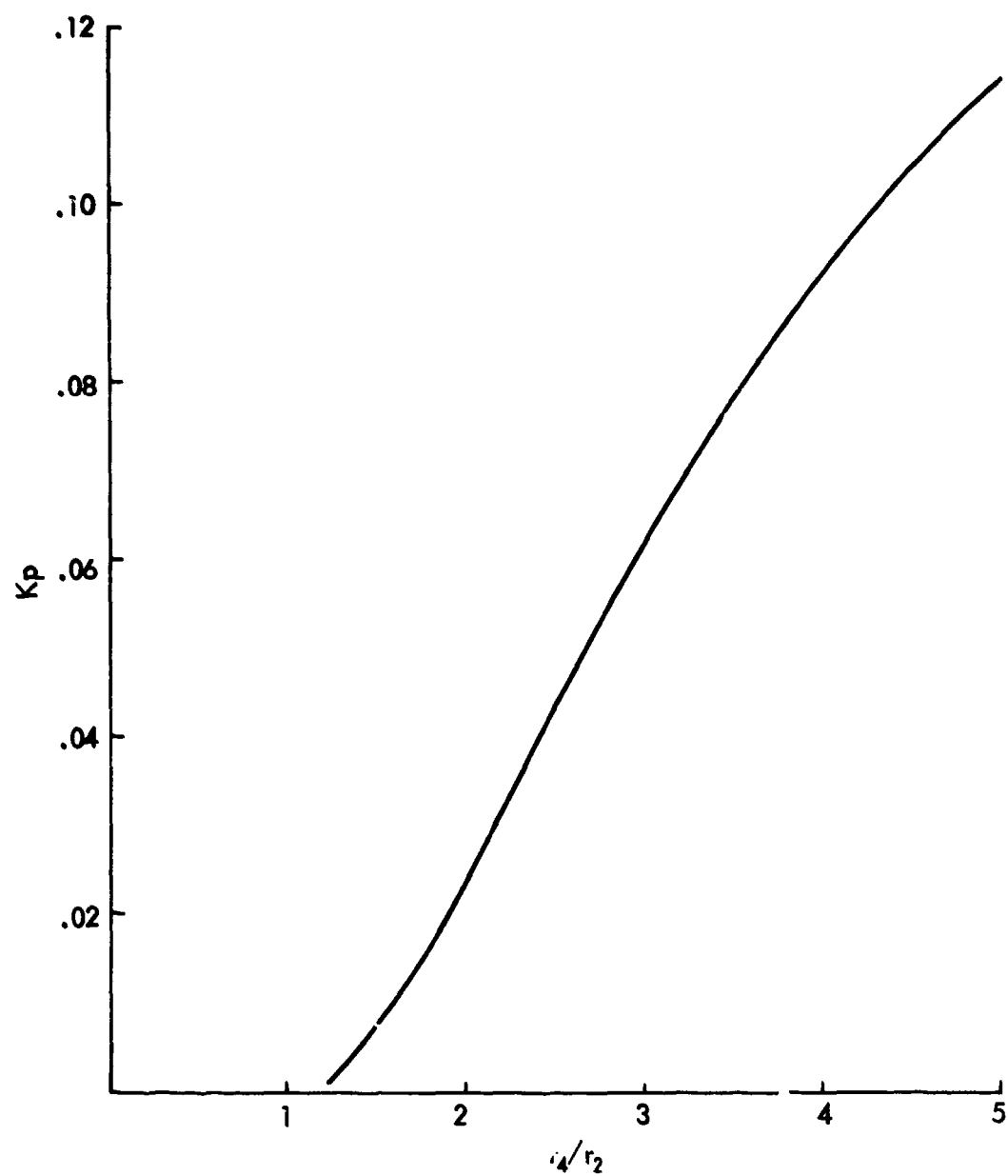


FIGURE 45 CONSTANT K_p FOR CENTER POST LOAD

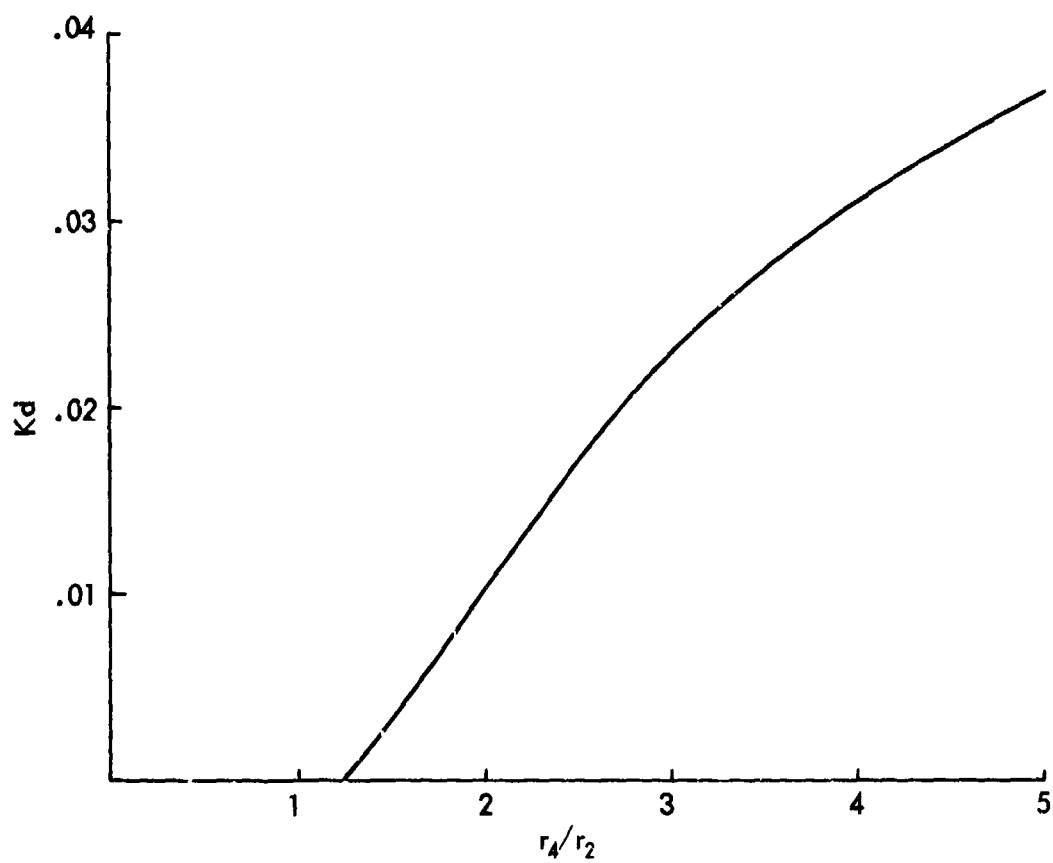


FIGURE 46 CONSTANT K_D FOR UNIFORM LOADING-CENTER POST DIAPHRAGM

$$F_k = \frac{Et^3}{r_4^2} \left[\frac{y_{md}}{K_d} + \frac{y_{m1} - y_{m2}}{K_p} \right]$$

This is the basic equation for the transducer design.

An interesting design possibility shown by the above equation is that of eliminating the effect of P_g by the proper relationship between r_1 , r_2 and r_4 . Extracting the components of force due to P_g in the above equation we have

$$\frac{Et^3}{r_4^2} \times \frac{y_{md}}{K_d} = \pi P_g (r_4^2 - r_2^2)$$

$$\frac{Et^3}{r_4^2} \times \frac{y_{m2}}{K_p} = \pi P_g (r_1^2 - r_2^2)$$

These two components of the total diaphragm force are opposed and offsetting. Taking the ratio of these two equations

$$\frac{y_{md} K_p}{y_{m2} K_d} = \frac{r_4^2 - r_2^2}{r_1^2 - r_2^2}$$

This latter relationship permits a design where the effects of P_g are cancelled which eliminates concern over a transient gap pressure differential.

APPENDIX B

ANALYSIS OF THE APT SENSOR CIRCUIT

The voltage across C_c (reference Figure 8) due to the drive across the bridge for the situation where $R_1, R_2 \gg X_{c1}, X_{c2}$

$$E_c = E_D \frac{C_1}{C_c + C_s + C_1} \quad (C_s \text{ is diode and stray capacitance})$$

An incremental change in the diaphragm capacitance C_c results in a corresponding change in E_c :

$$\frac{dE_c}{E_c} = - \frac{dC_c}{C_c + C_s + C_1}$$

Both C_1 and C_c , due to unidirectional current through the diode D_1 , charge up to a dc voltage which is approximately the negative peak of E_c less the diode drop:

$$V_c = - E_c + .6 = - E_D \frac{C_1}{C_c + C_s + C_1} + .6$$

where E_c is taken to be the peak of the sine wave drive voltage.

Similarly, the dc voltage across C_o is approximately

$$V_o = + E_o - .6 = + E_D \frac{C_2}{C_c + C_s + C_2} - .6$$

There is current flowing through R_1 and R_2 due to the capacitor charges

$$I = \frac{V_o - V_c}{R_1 + R_2}$$

The dc voltage at summing junction of R_1 and R_2 is

$$V_s = IR_1 + V_c = \frac{V_o - V_c}{R_1 + R_2} R_1 + V_c$$

Since $R_1 = R_2$

$$V_s = \frac{V_o}{2} + \frac{V_c}{2} = \frac{1}{2} \left[E_D \frac{C_2}{C_o + C_s + C_2} - .6 \right] + \frac{1}{2} \left[-E_D \frac{C_1}{C_c + C_s + C_1} + .6 \right]$$

$$V_s = \frac{E_D}{2} \left[\frac{C_2}{C_o + C_s + C_2} - \frac{C_1}{C_c + C_s + C_1} \right]$$

This voltage, V_s , is the bridge output which appears as the input to the opamp IC1 in the circuit in Figure 7.

It can readily be seen from the expression for V_s that if the circuit components are balanced, the output voltage is zero.

The incremental output due to a small change in C_c is

$$dv_s = \frac{E_D}{2} \frac{C_1 dC_c}{(C_c + C_s + C_1)^2} .$$

APPENDIX C
FLIGHT REENTRY HEATING AND ABLATION

To assist in the evaluation of APT Arc Heater Test data, a series of calculations were completed on the ablation and heat parameters encountered during typical RV reentries. The RV model was that similar to an actual weapon, heatshield material was 20° bias tape-wound carbon phenolic. The following trajectories were used:

<u>Trajectory No.</u>	<u>Velocity mps</u>	<u>Reentry Angle</u>
1	7711	-40°
2	6401	-40°
3	7605	-20°
4	7010	-30°

Conditions at five points along the heatshield were calculated: 31.8, 47.6, 63.5, 95.3 and 127 cm. Transition was forced at 25.9 km altitude. Figures 47 and 48 show ablation and char depths versus altitude while peak heating rate and total heat are shown in Figures 49 and 50. Computer programs used for these calculations were ARROW and REKAP.

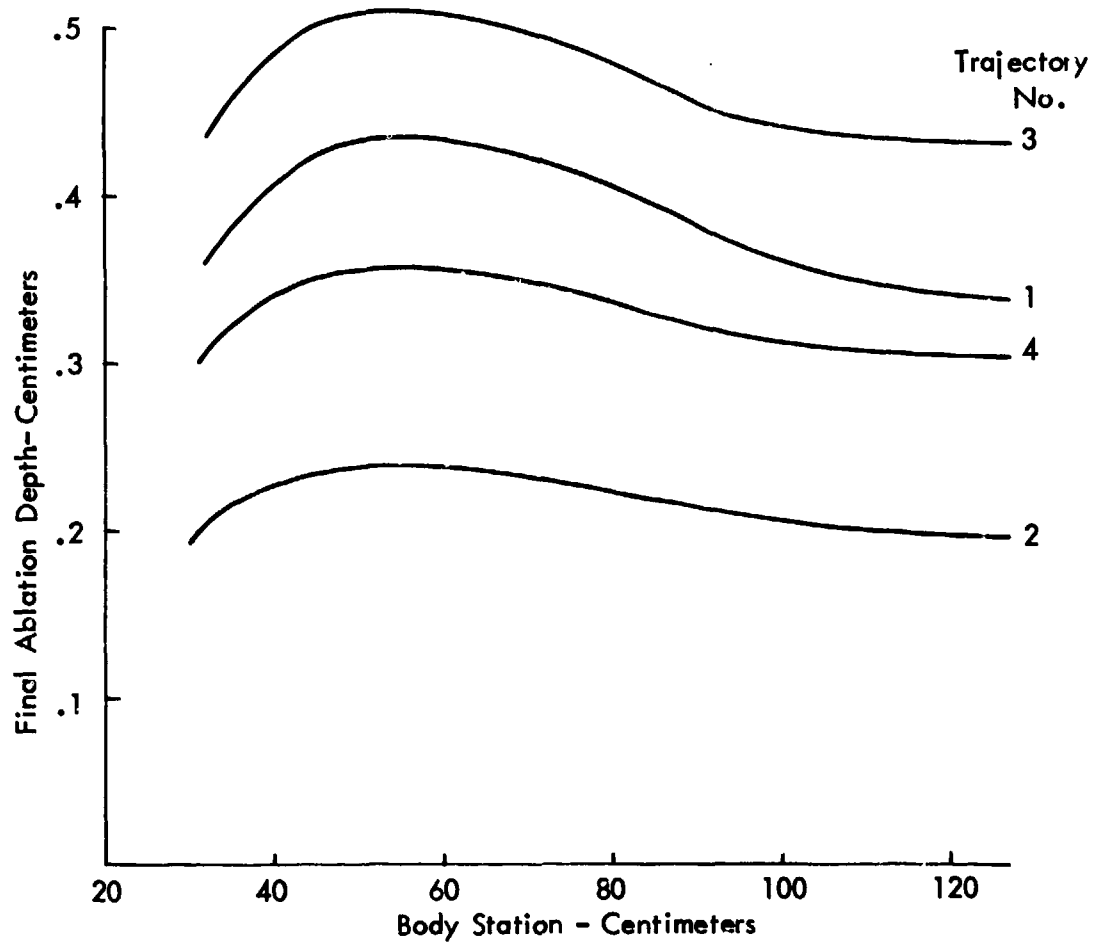


FIGURE 47 TOTAL ABLATION -4 TRAJECTORIES

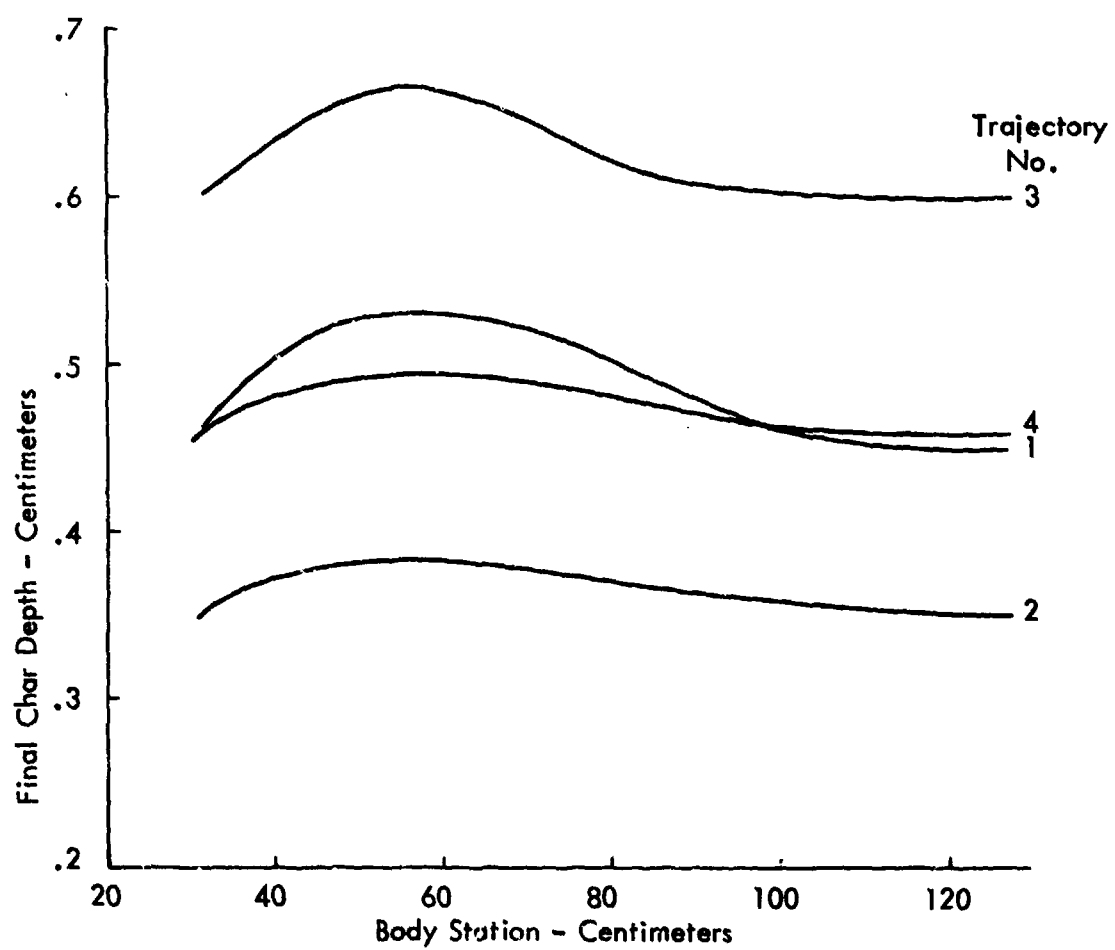


FIGURE 48 CHAR DEPTH

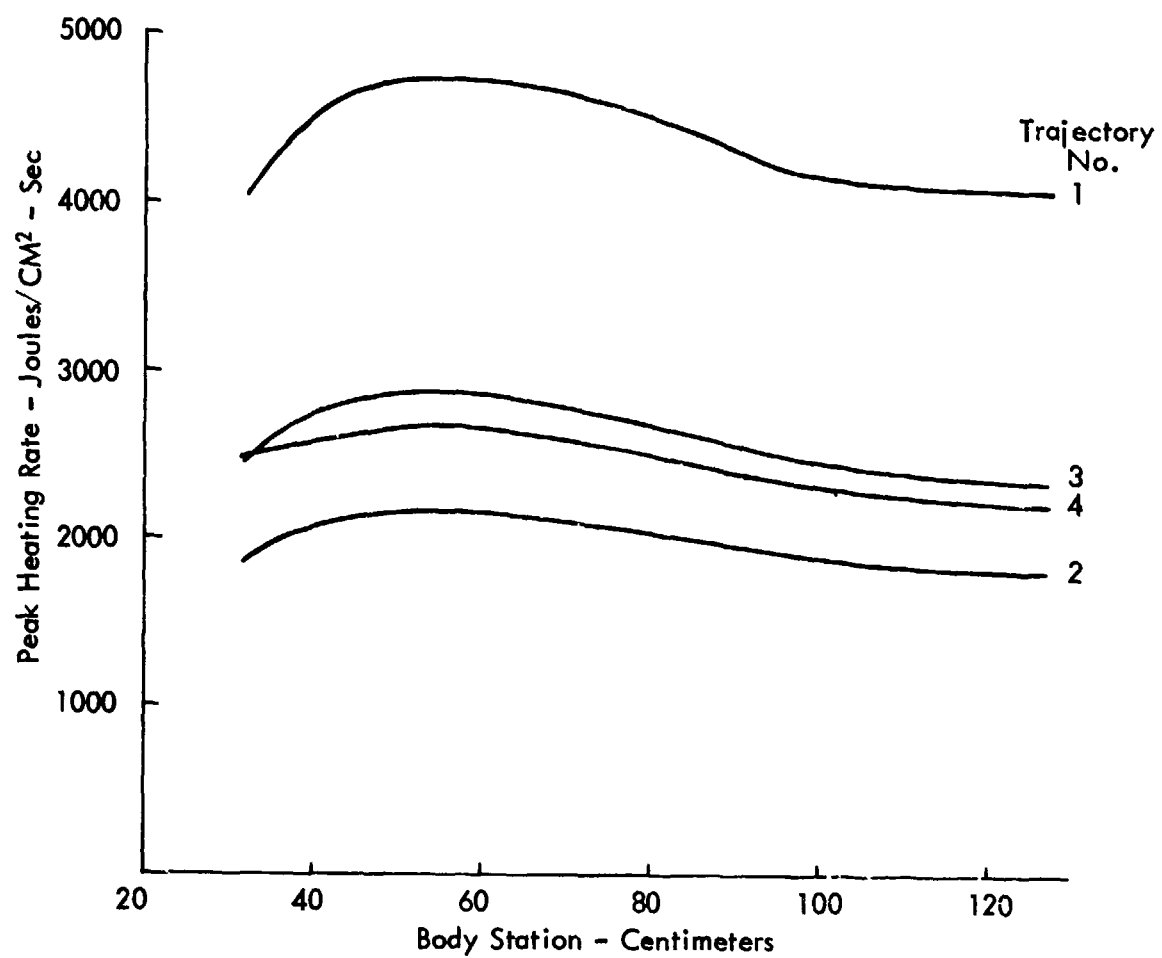


FIGURE 49 PEAK HEATING RATE

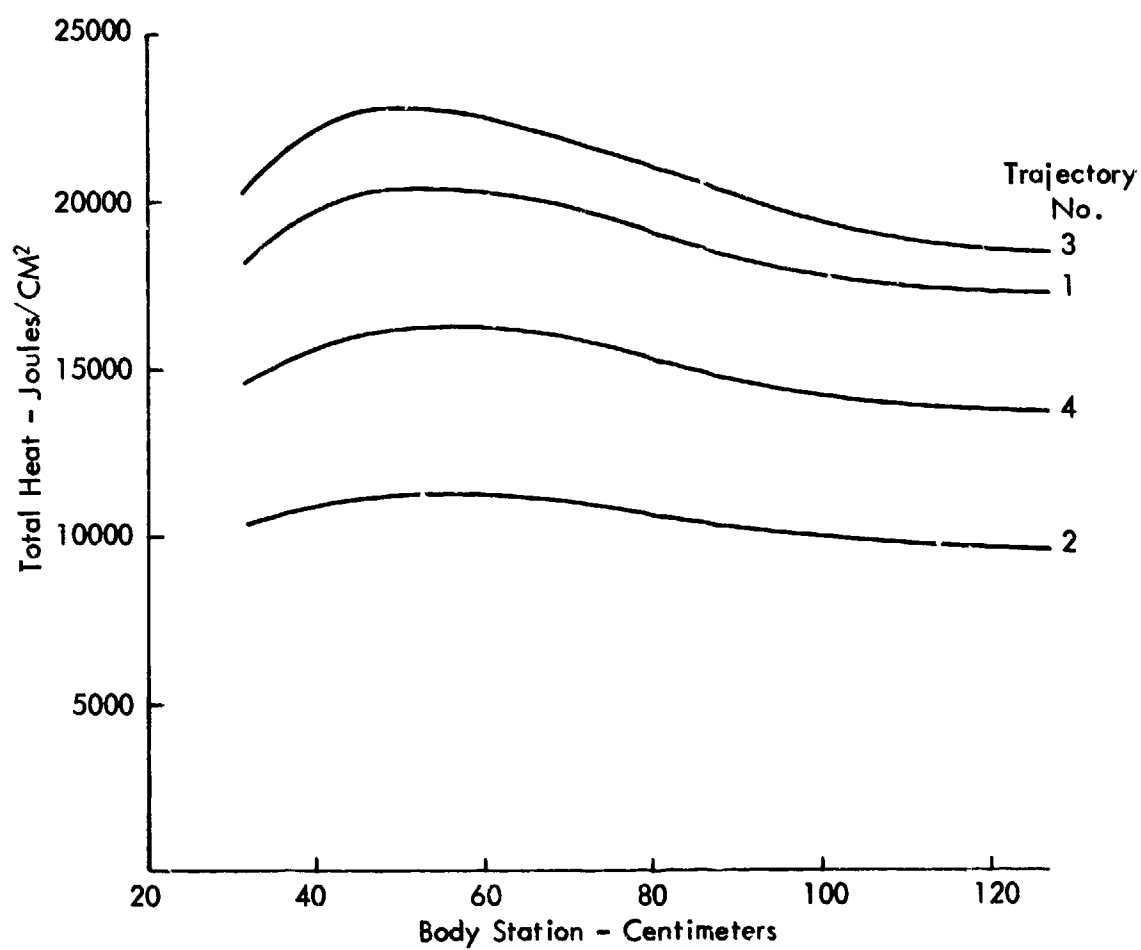


FIGURE 50 TOTAL HEAT

APPENDIX D
TEST RUN 1 PHOTOGRAPHS

PRECEDING PAGE NOT FILMED
BLANK

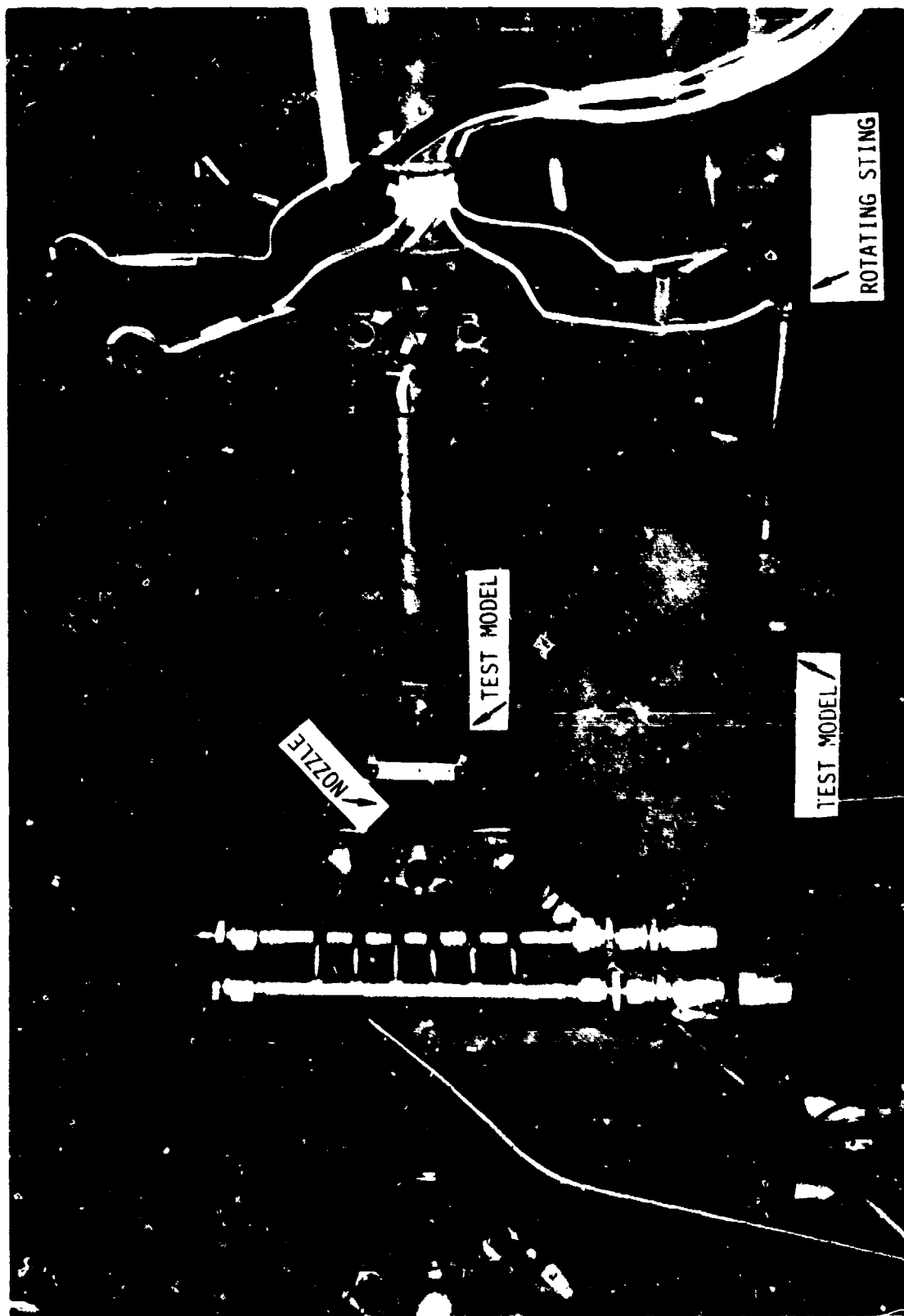


FIGURE 51 TEST RUN 1, PRE-TEST INSTALLATION

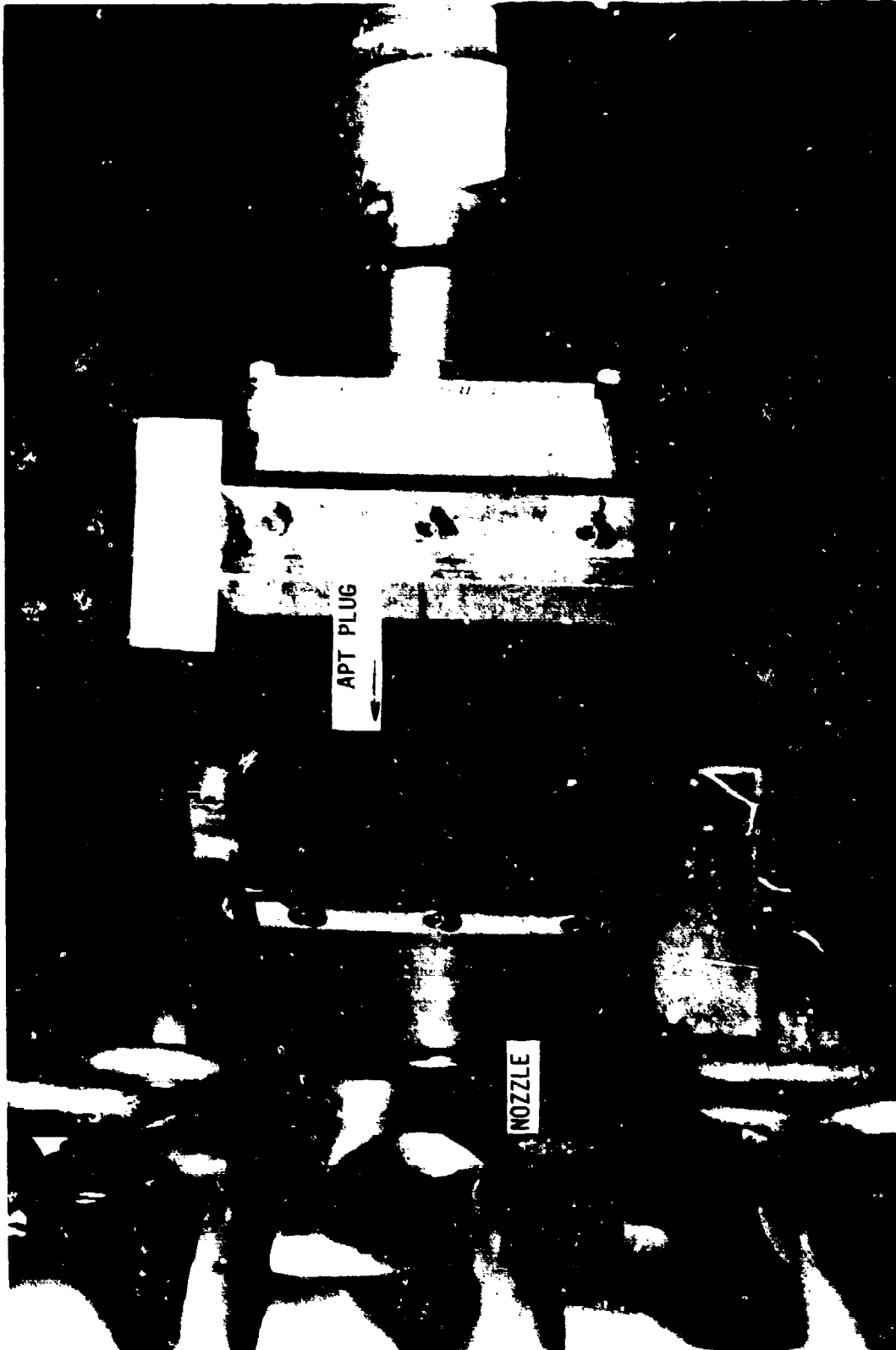


FIGURE 52 TEST RUN 1, PRE-TEST STING 2

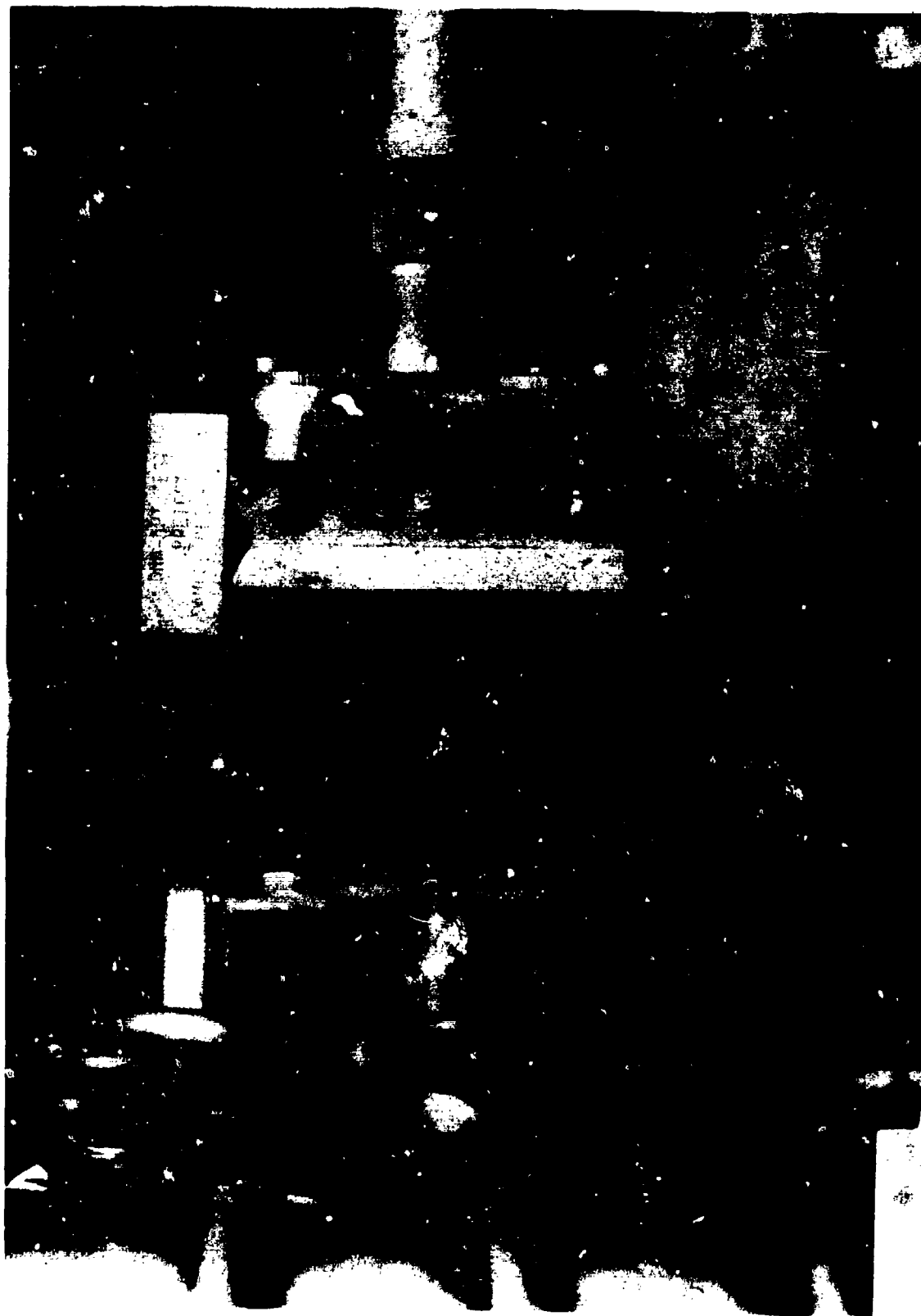


FIGURE 53 TEST RUN 1, PRE-TEST STING 3

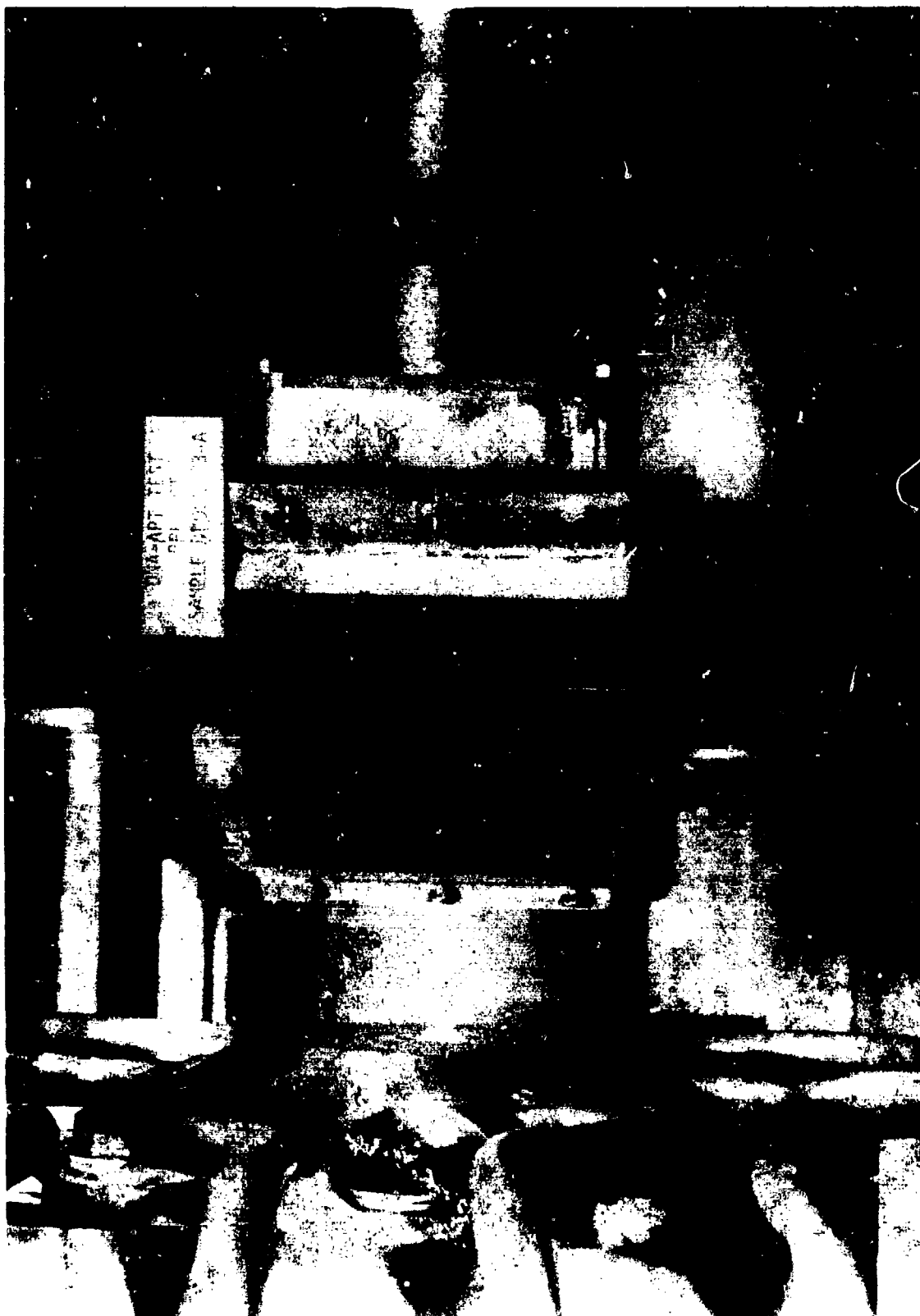


FIGURE 54 TEST RUN 1, PRE-TEST STING 4

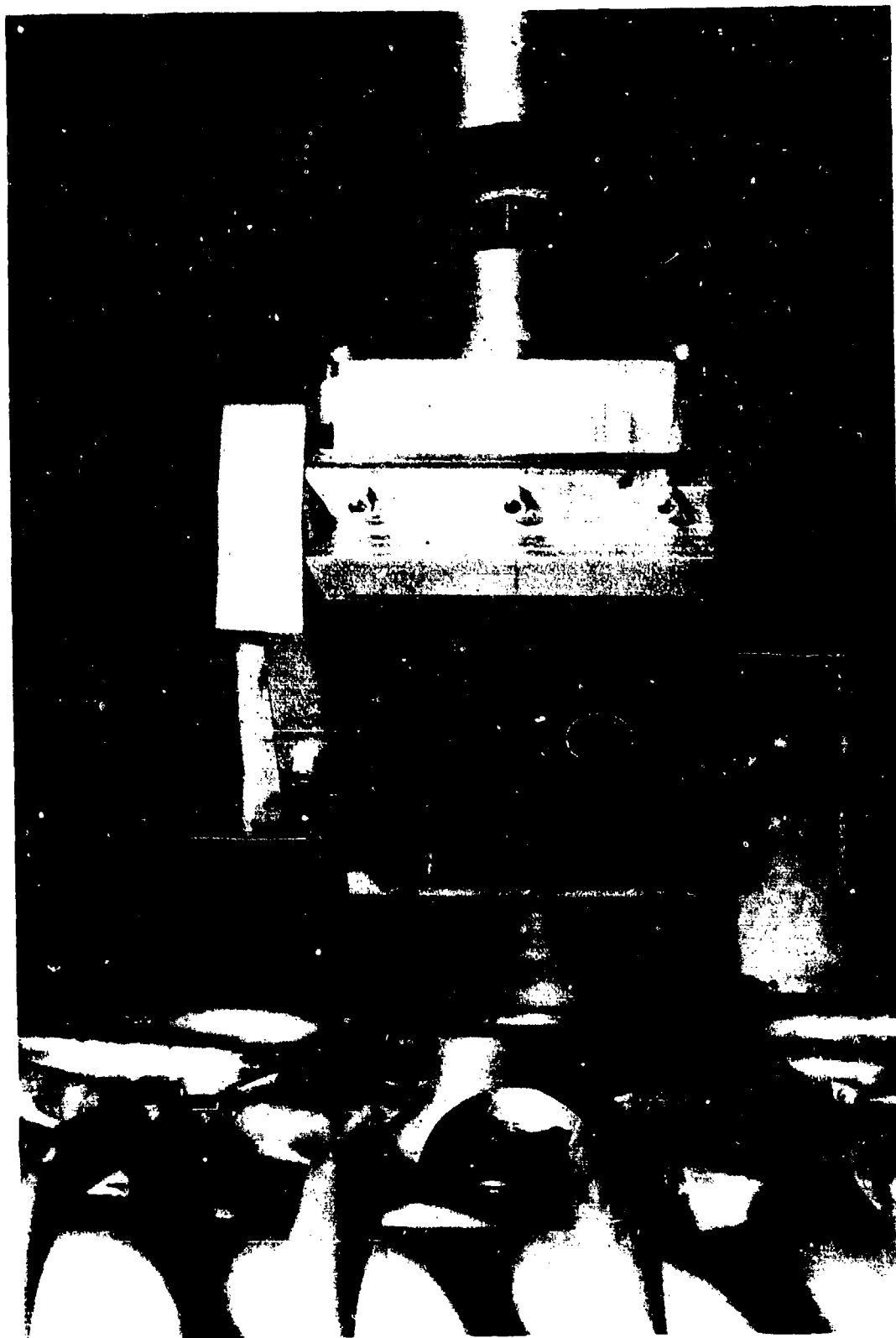


FIGURE 55 TEST RUN 1, PRE-TEST STING 5

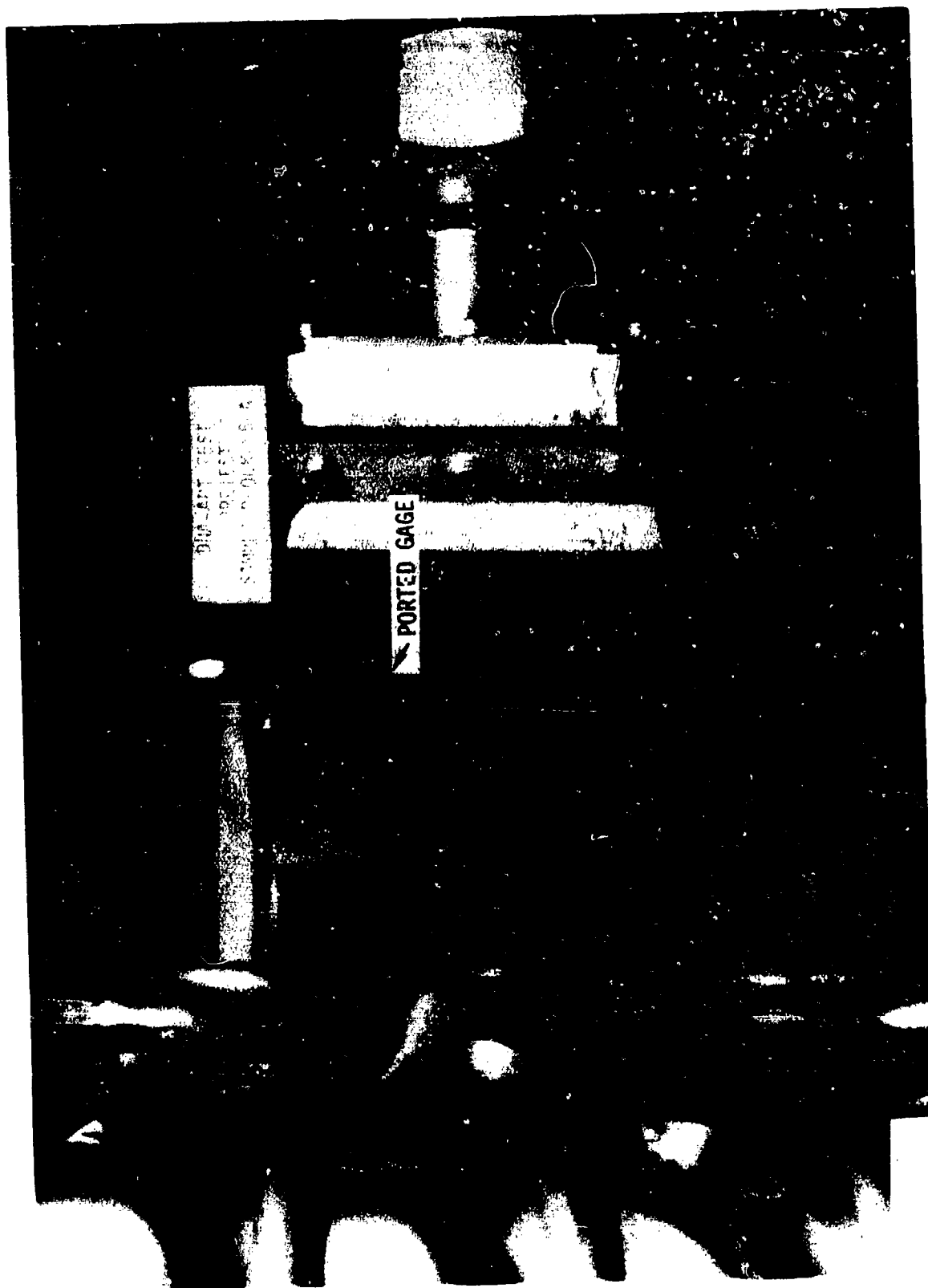


FIGURE 56 TEST RUN 1, PRE-TEST STING 6

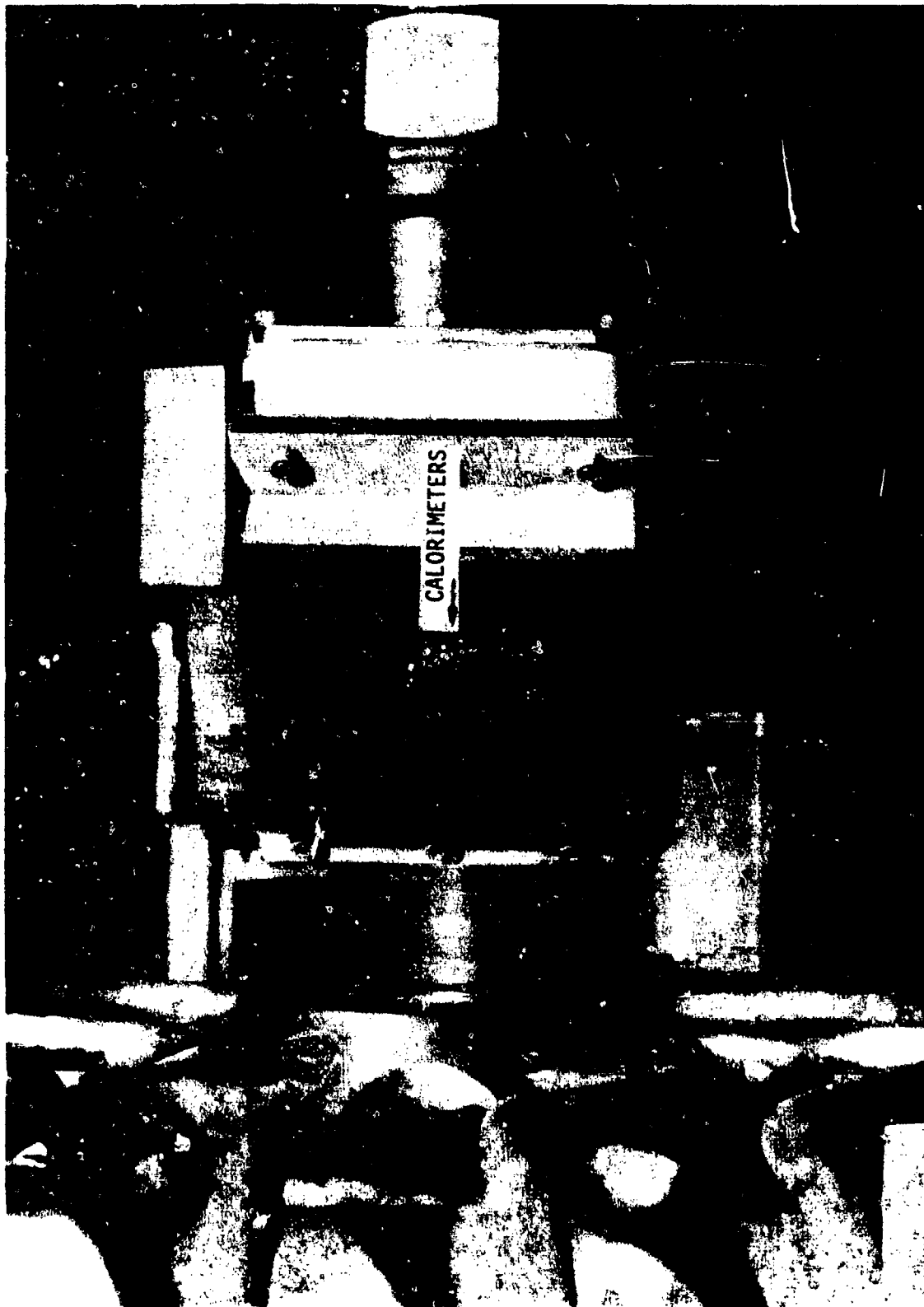


FIGURE 57 TEST RUN 1, PRE-TEST STING 7

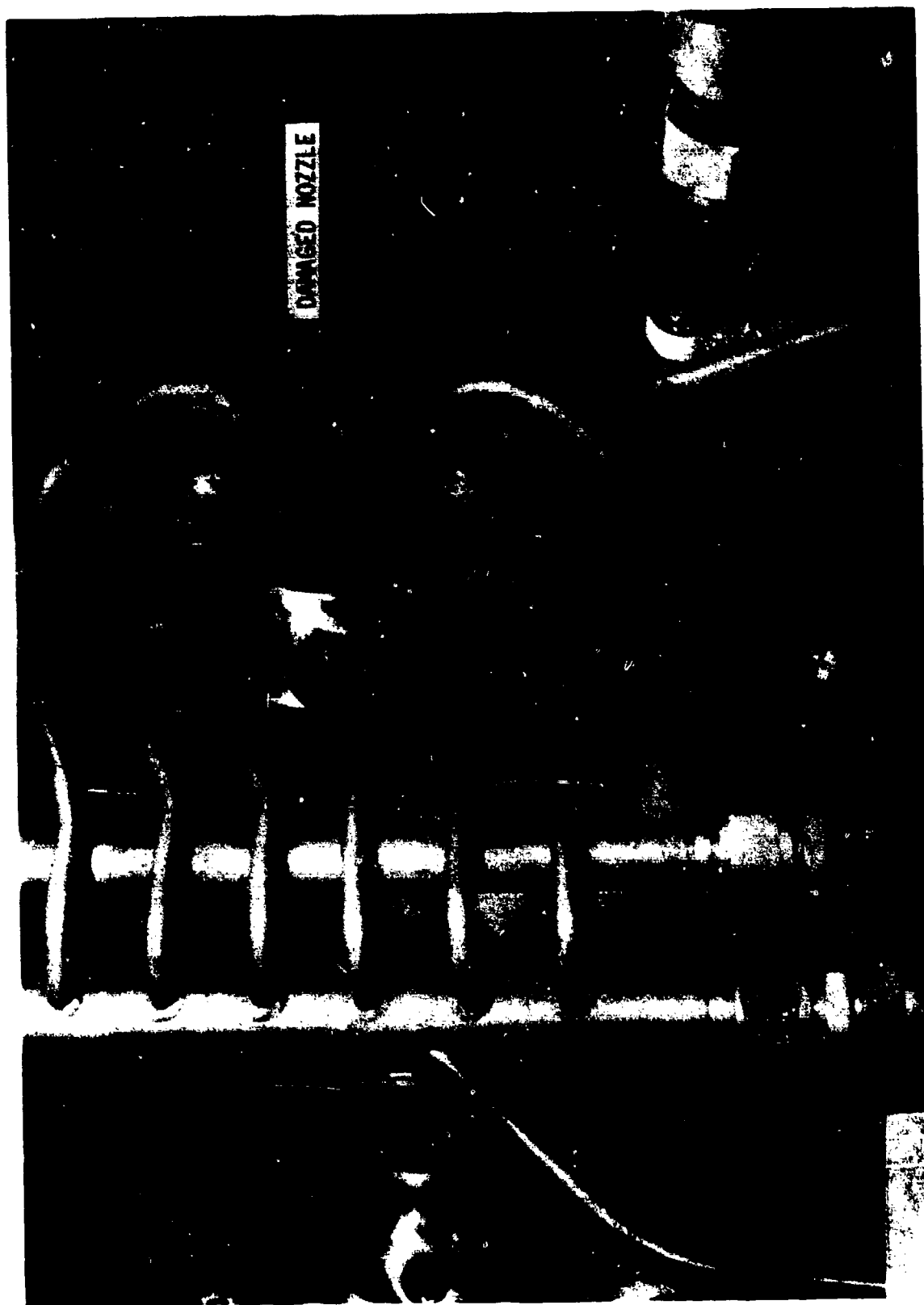


FIGURE 58 TEST RUN 1, POST-TEST NOZZLE

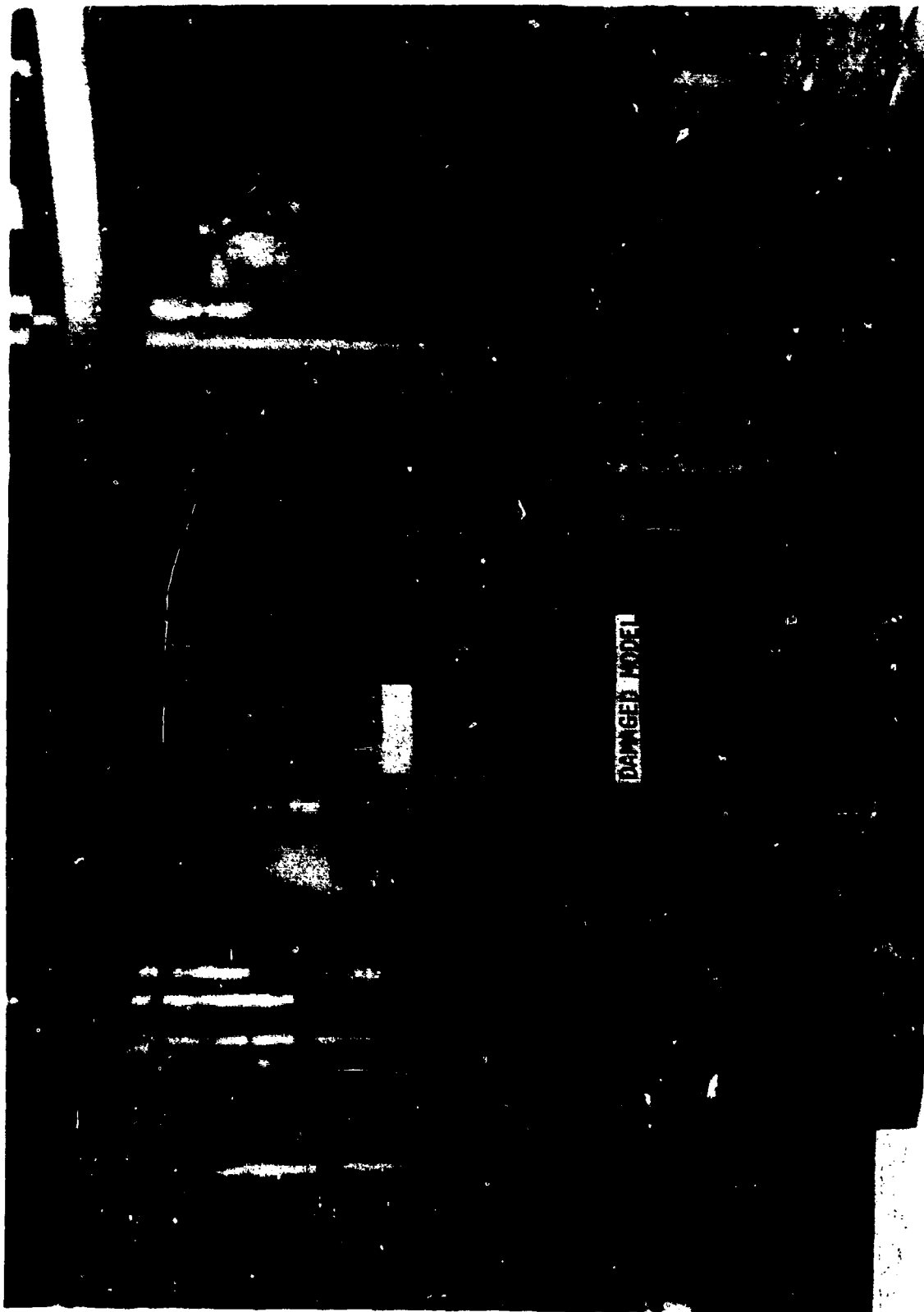


FIGURE 59 TEST RUN 1, POST-TEST MODEL DAMAGE

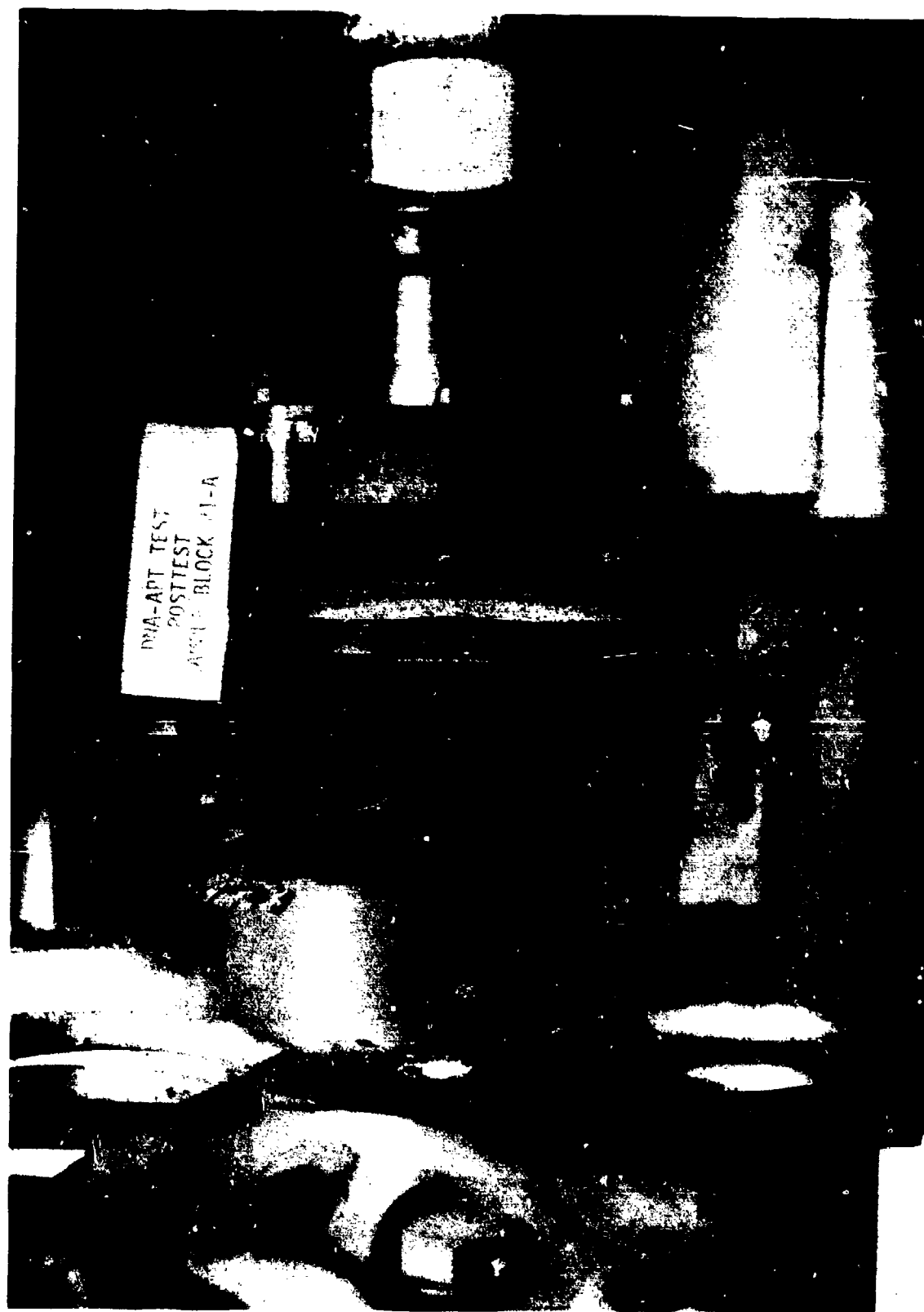


FIGURE 60 TEST RUN 1, POST-TEST STING 2

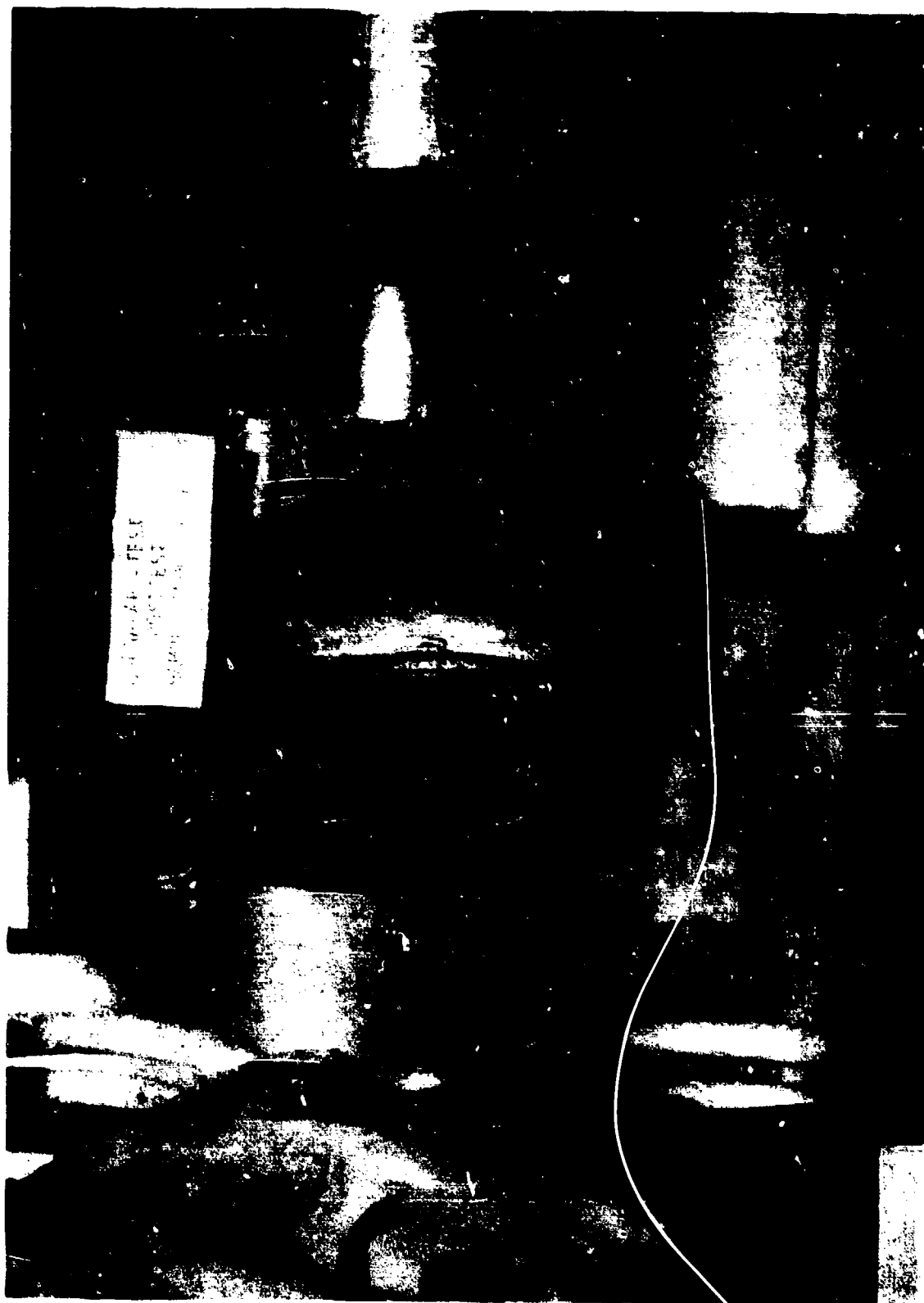


FIGURE 61 TEST RUN 1, POST-TEST STING 3



FIGURE 62 TEST RUN 1, POST-TEST STING 4

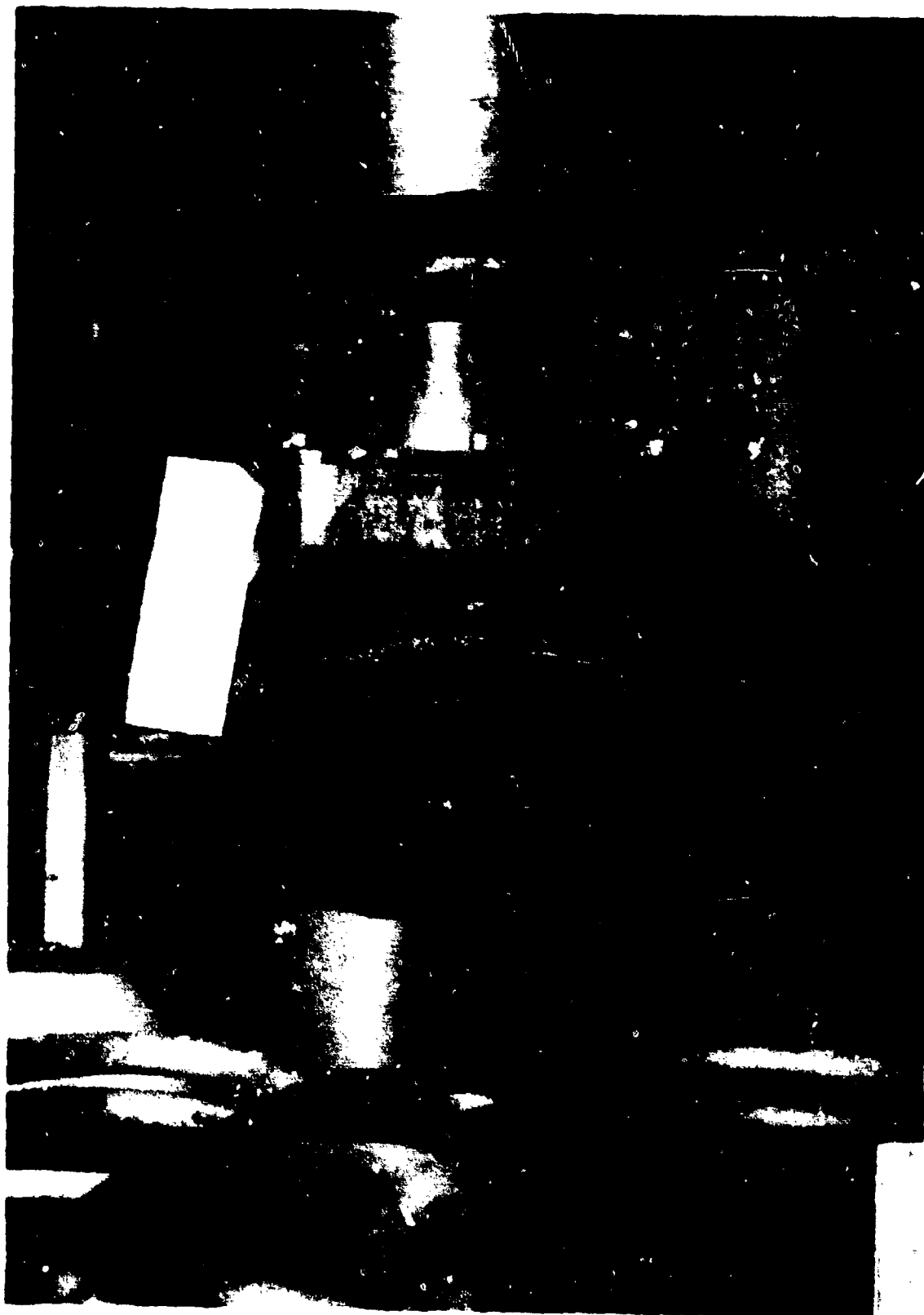


FIGURE 63 TEST RUN 1, POST-TEST STING 5

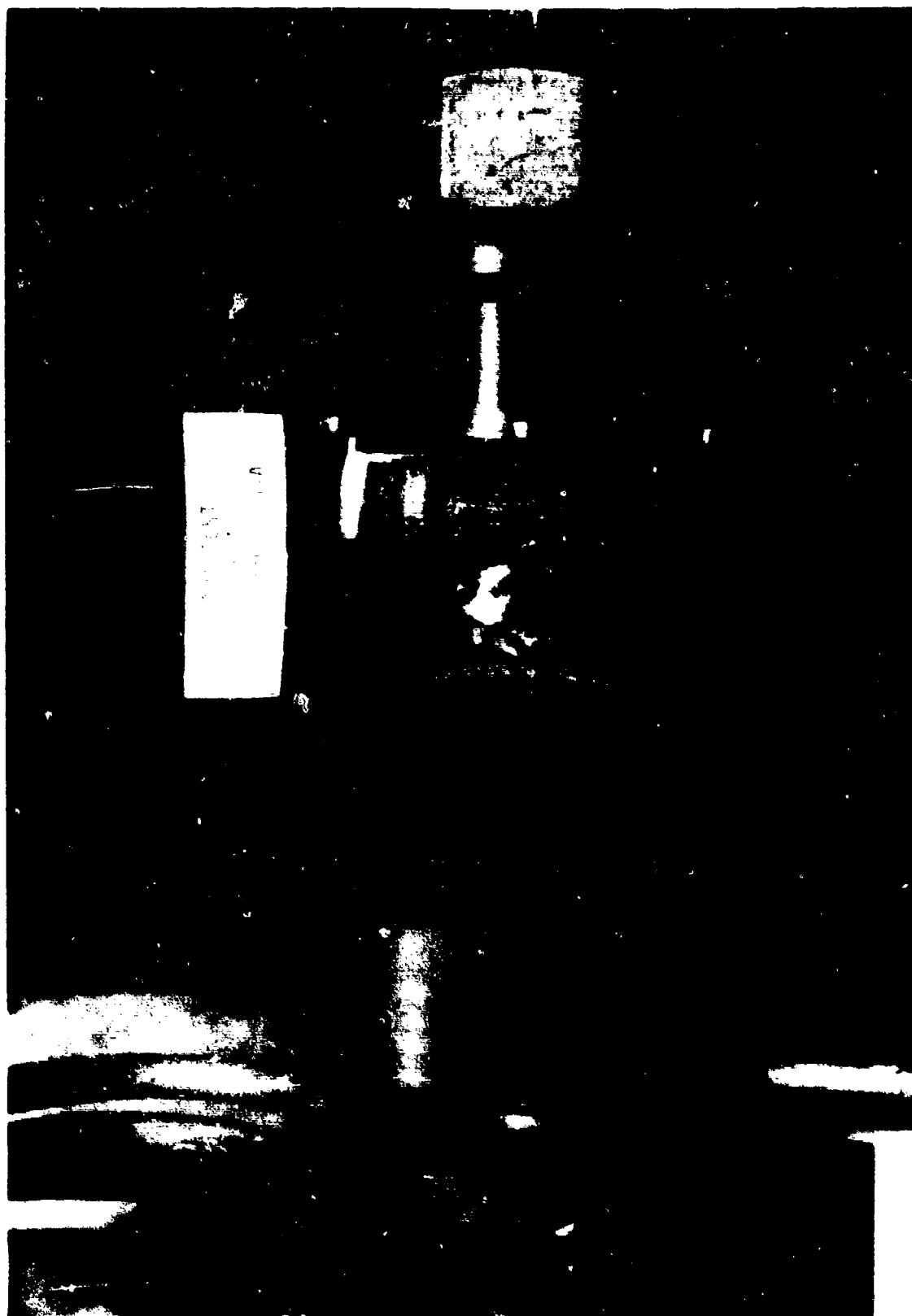


FIGURE 64 TEST RUN 1, POST-TEST STING 6

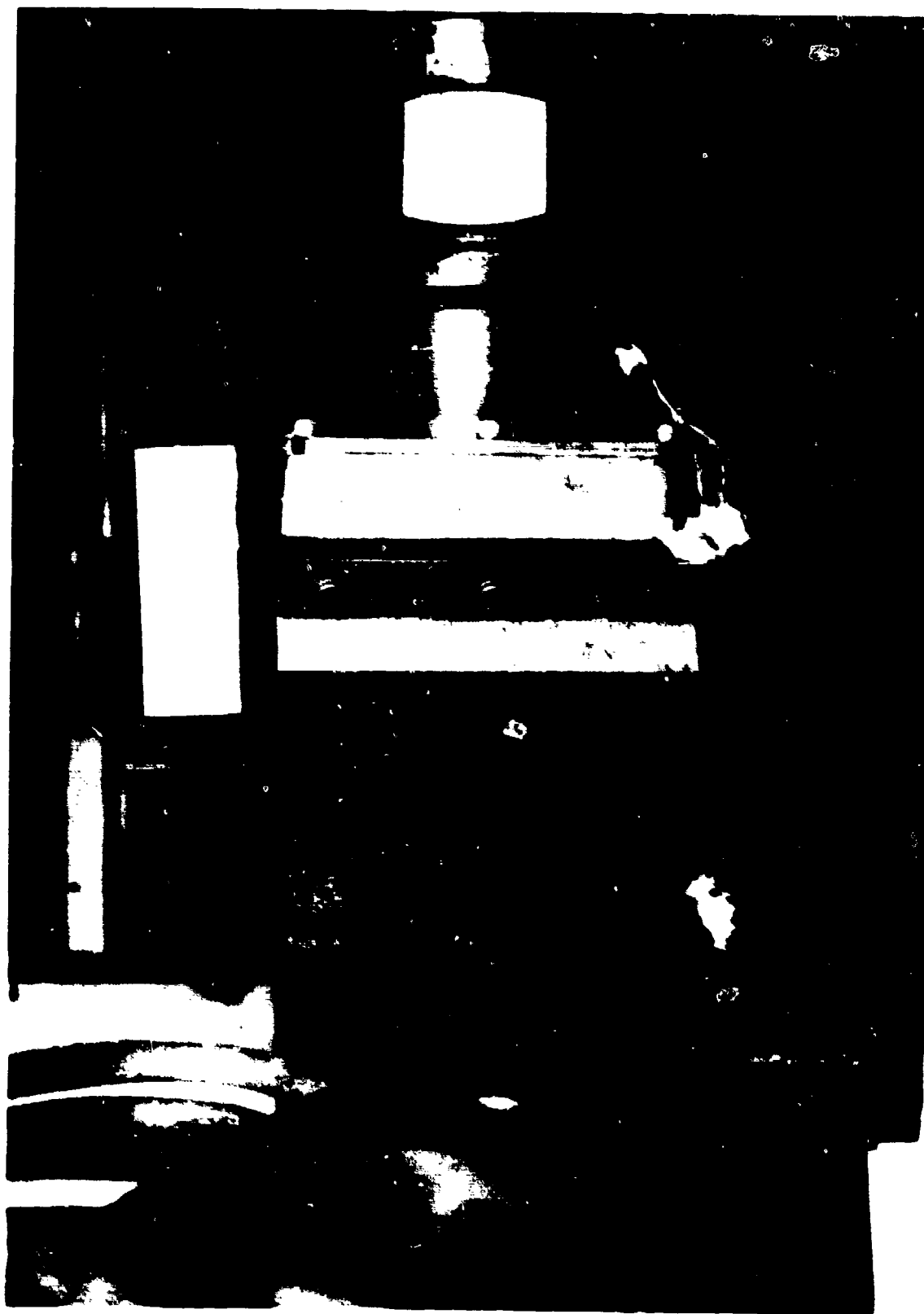


FIGURE 65 TEST RUN 1, POST-TEST STING 7

APPENDIX E
TEST RUN 2 PHOTOGRAPHS



DARK AREAS ARE HOTTER



FIGURE 66 TEST RUN 2, STING 1 NEGATIVE PHOTO

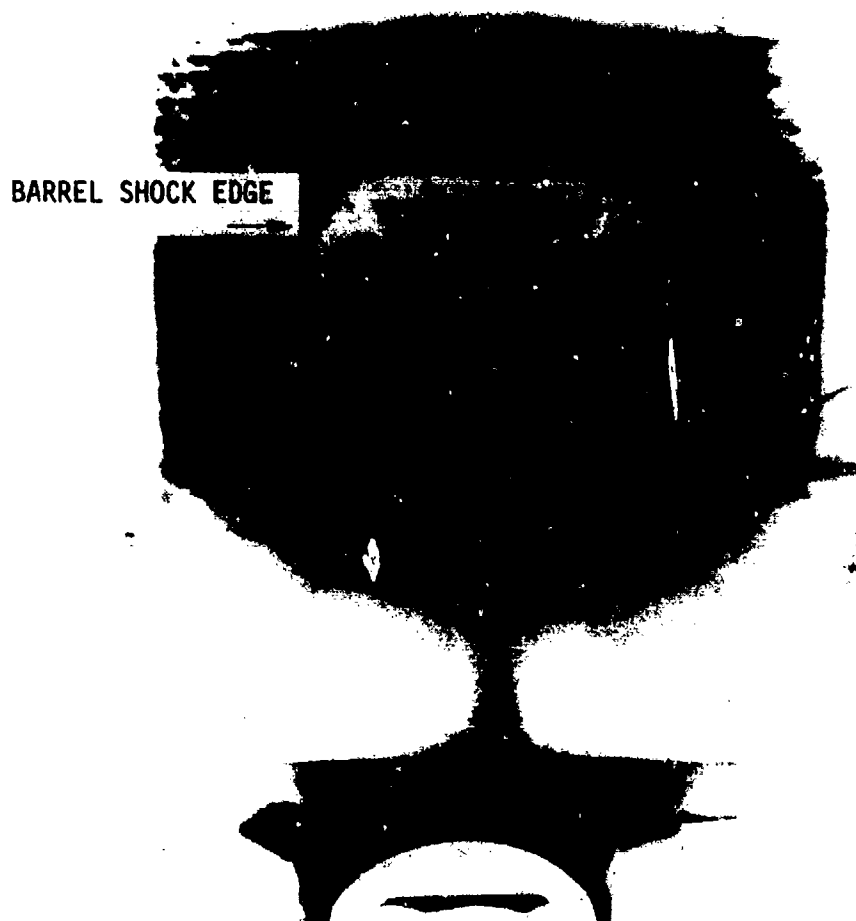
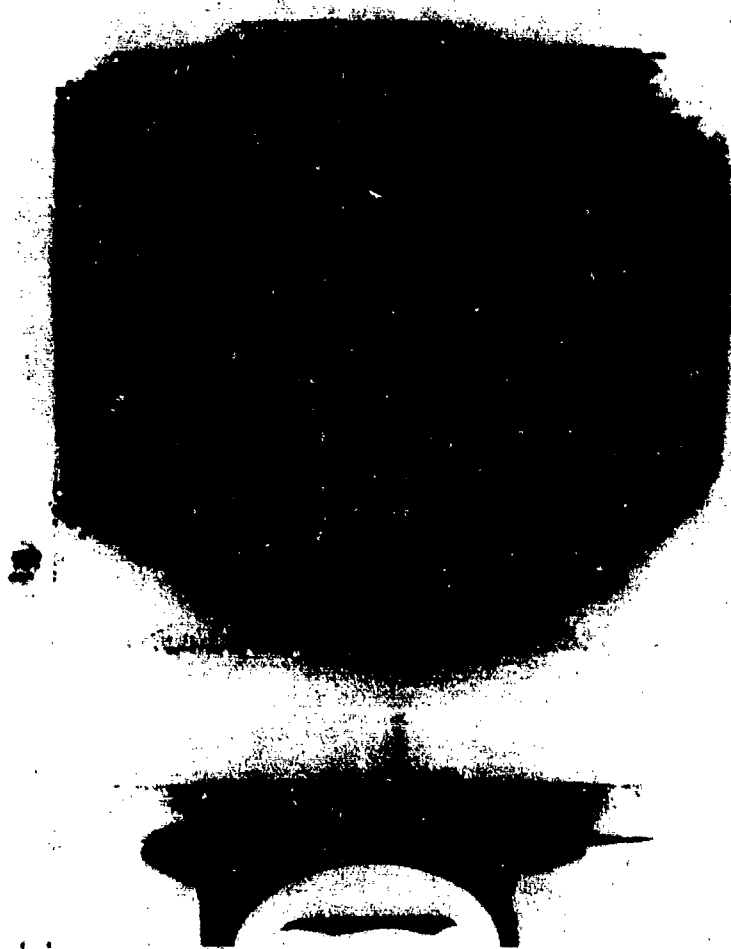


FIGURE 67 TEST RUN 2, STING 2 NEGATIVE PHOTO



FIGURF 68 TEST RUN 2, STING 3 NEGATIVE PHOTO



FIGURE 69 TEST RUN 2, STING 4 NEGATIVE PHOTO



FIGURE 70 TEST RUN 2, STING 5 NEGATIVE PHOTO

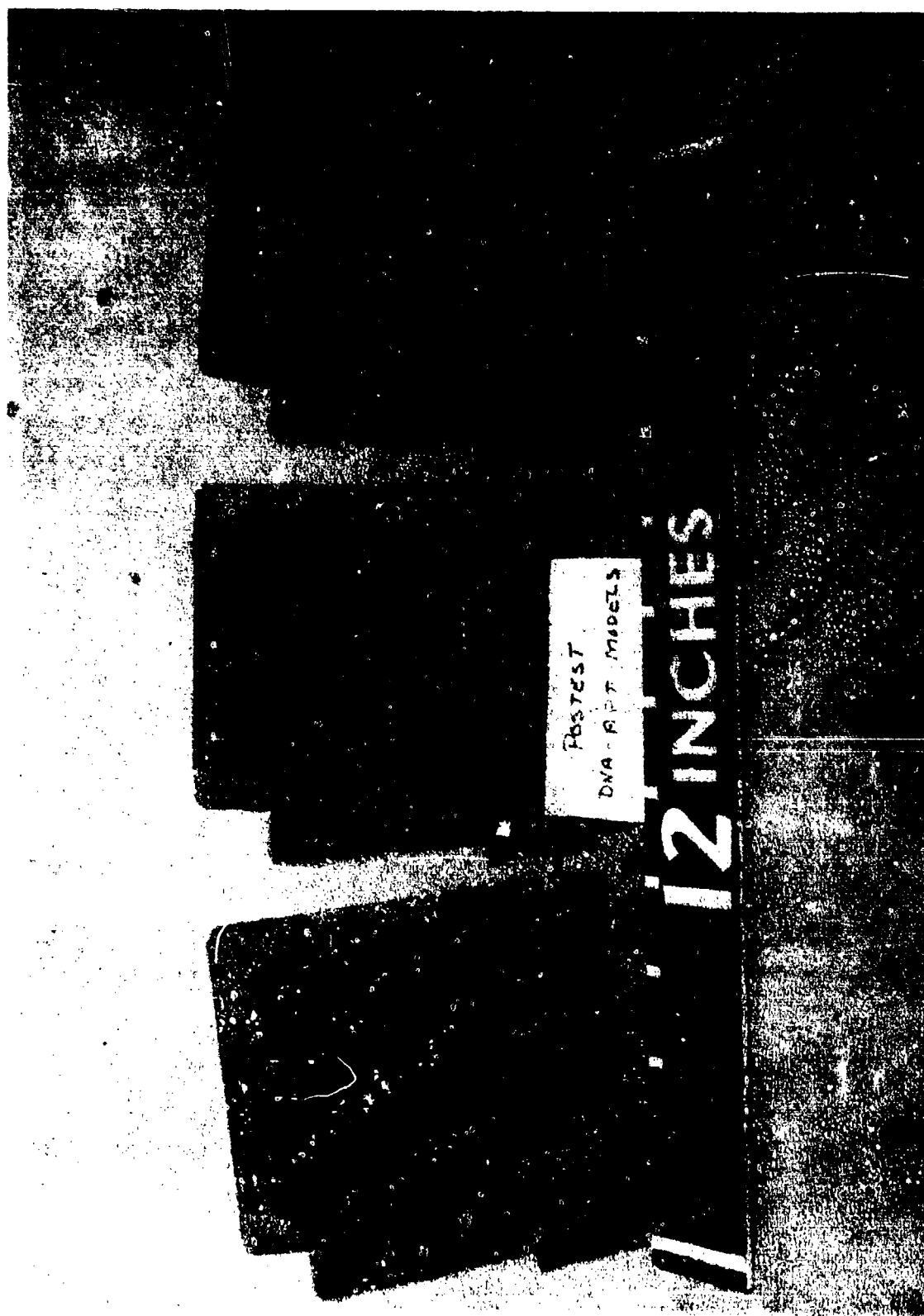


FIGURE 71 TEST RUN 2, POST-TEST MODELS

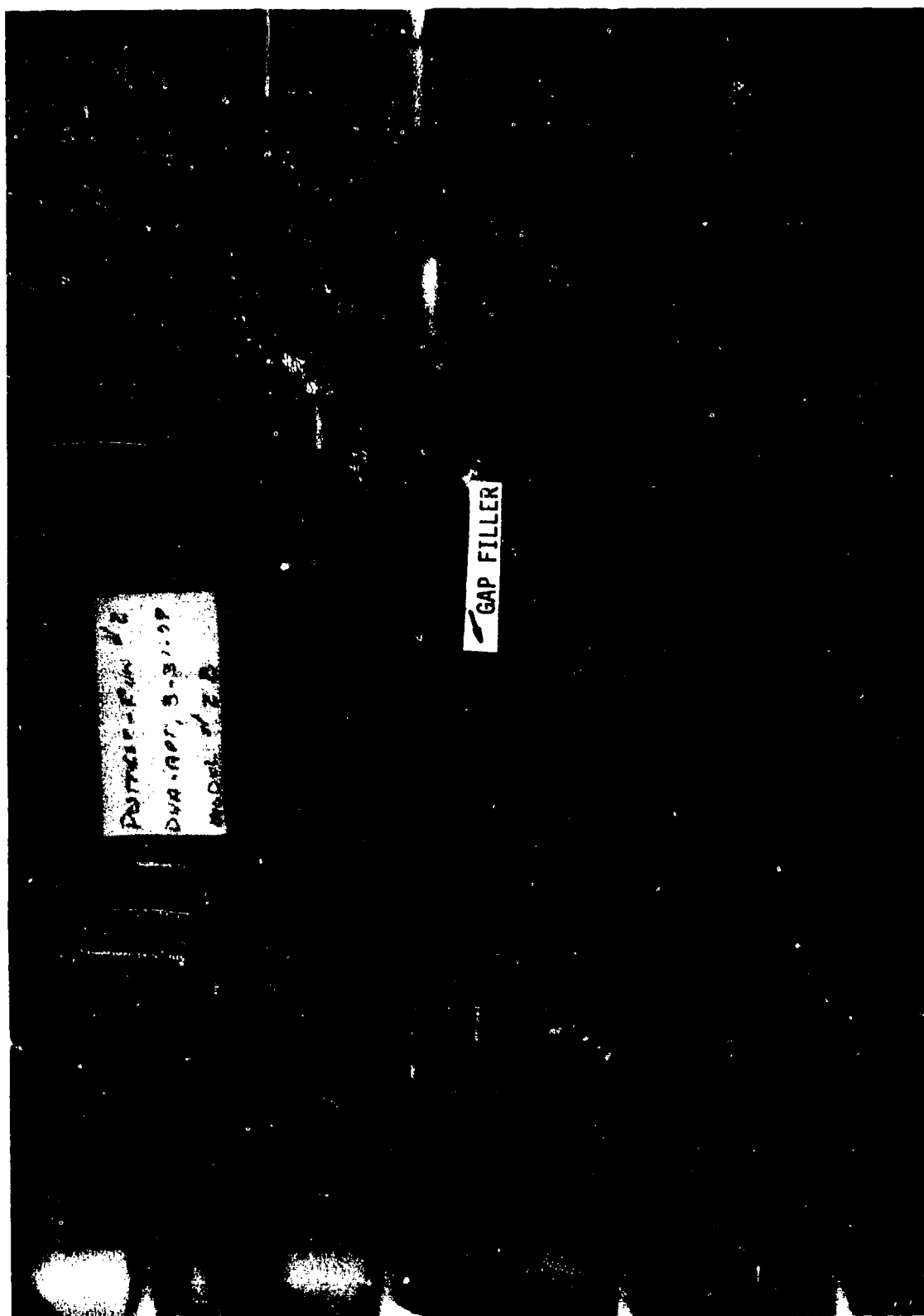


FIGURE 72 TEST RUN 2, POST-TEST MODEL

APPENDIX F
TEST RUN 3 PHOTOGRAPHS

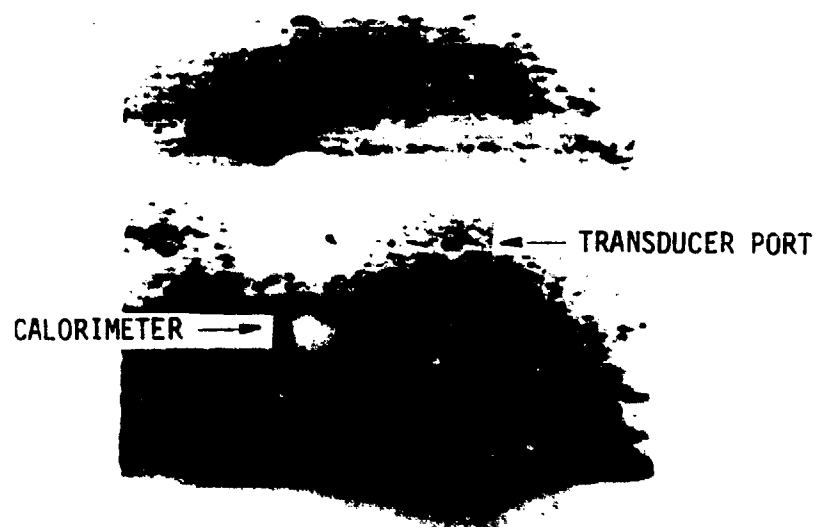


FIGURE 73 TEST RUN 3, STING 1 NEGATIVE PHOTO

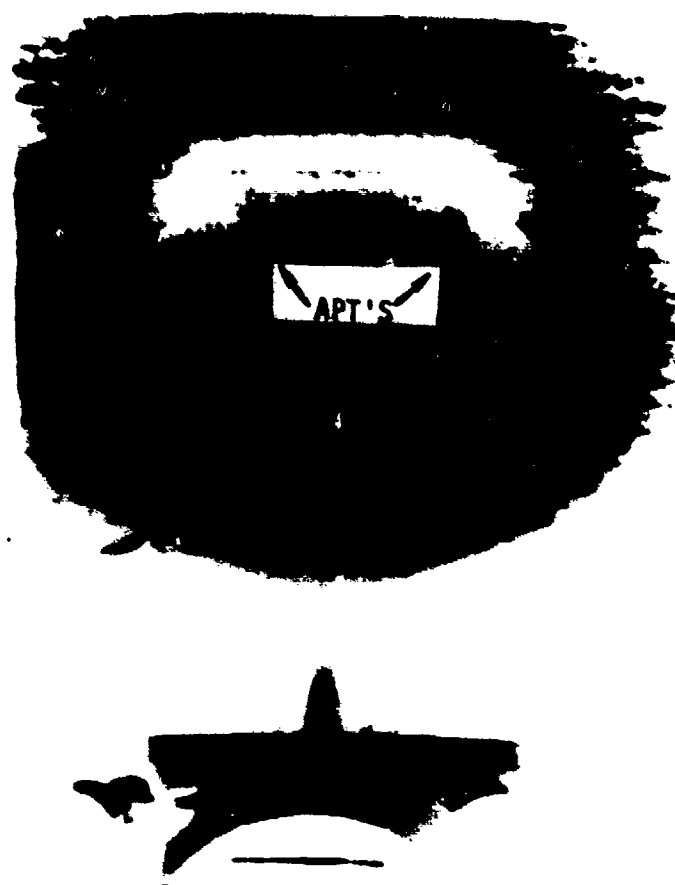


FIGURE 74 TEST RUN 3, STING 2 NEGATIVE PHOTO

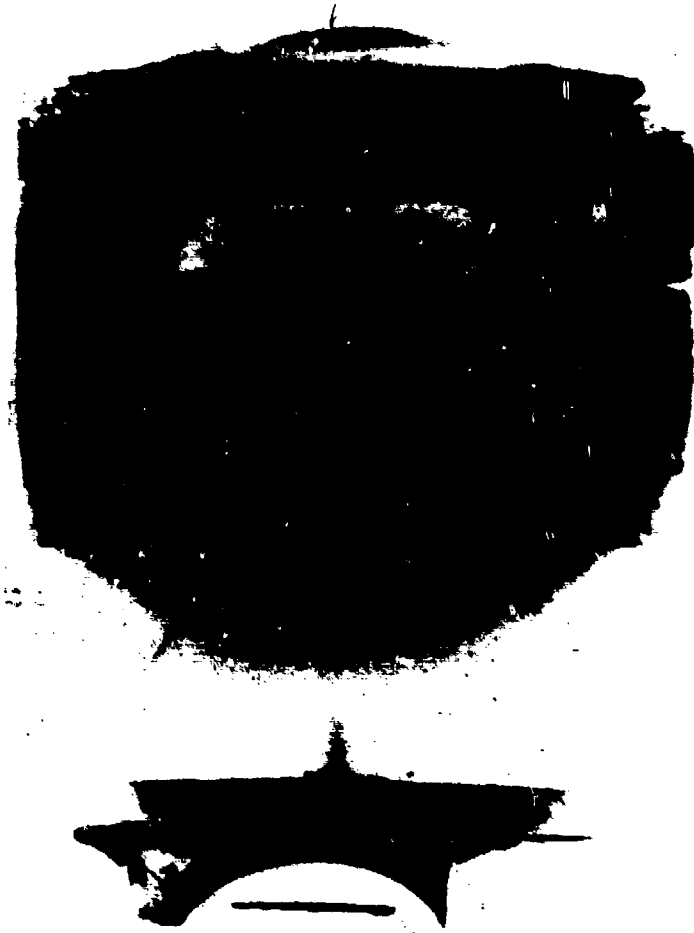


FIGURE 75 TEST RUN 3, STING 3 NEGATIVE PHOTO

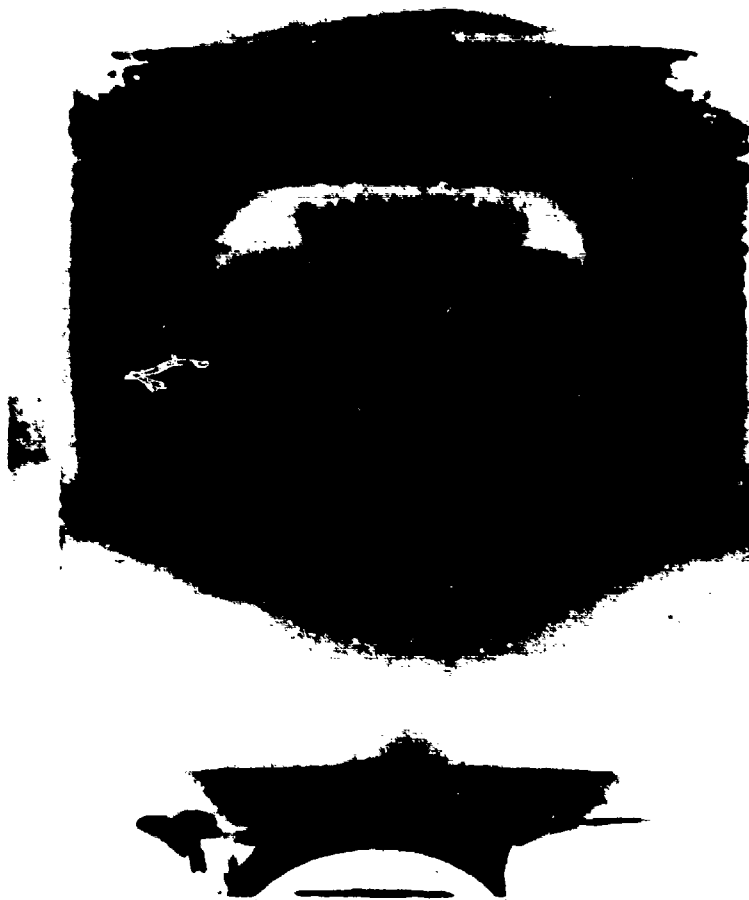


FIGURE 76 TEST RUN 3, STING 4 NEGATIVE PHOTO



FIGURE 77 TEST RUN 3, STING 5 NEGATIVE PHOTO



FIGURE 78 TEST RUN 3, POST-TEST MODEL 1



FIGURE 79 TEST RUN 3, POST-TEST MODEL 2

DISTRIBUTION LIST

DEPARTMENT OF DEFENSE

Assistant to the Secretary of Defense
Atomic Energy
ATTN: Executive Assistant

Defense Advanced Rsch. Proj. Agency
ATTN: TIO

Defense Documentation Center
12 cy ATTN: DD

Defense Intelligence Agency
ATTN: DT-1B
ATTN: DT-2

Defense Nuclear Agency
ATTN: DDST
ATTN: SPAS
ATTN: STSP
4 cy ATTN: TITL

Field Command
Defense Nuclear Agency
ATTN: FCPR

Field Command
Defense Nuclear Agency
Livermore Division
ATTN: FCPRL

Joint Chiefs of Staff
ATTN: J-5, Nuclear Division

Joint Strat. Tgt. Planning Staff
ATTN: JPTM
ATTN: JLTW-2

NATO School (SHAPE)
ATTN: U.S. Documents Officer

Undersecretary of Defense for Rsch. & Engrg.
ATTN: Strategic & Space Systems (OS)

DEPARTMENT OF THE ARMY

BMD Advanced Technology Center
Department of the Army
ATTN: ATC-M

Deputy Chief of Staff for Ops. & Plans
Department of the Army
ATTN: DAMG-NCZ

Deputy Chief of Staff for Rsch., Dev., & Acq.
Department of the Army
ATTN: DAMA-CSS-N

Harry Diamond Laboratories
Department of the Army
ATTN: DELHD-N-RBH
ATTN: DELHD-RC

BMD Program Office
Department of the Army
ATTN: Technology Division

DEPARTMENT OF THE ARMY (Continued)

U.S. Army Ballistic Research Labs
ATTN: DRDAR-BL, R. Eichelberger

U.S. Army Material & Mechanics Rsch. Ctr.
ATTN: DRXMR-HH

U.S. Army Materiel Dev. & Readiness Cmd.
ATTN: DRCDE-D

U.S. Army Missile R&D Command
ATTN: DRDMI-XS

DEPARTMENT OF THE NAVY

Naval Research Laboratory
ATTN: Code 2627

Naval Sea Systems Command
ATTN: SEA-0351

Naval Surface Weapons Center
ATTN: Code K06
2 cy ATTN: Code K82

Office of the Chief of Naval Operations
ATTN: OP 604C

Strategic Systems Project Office
Department of the Navy
ATTN: NSP-272

DEPARTMENT OF THE AIR FORCE

Air Force Flight Dynamics Laboratory
ATTN: FBC
ATTN: FXG

Air Force Geophysics Laboratory
ATTN: LY, C. Touart

Air Force Materials Laboratory
ATTN: MBE
ATTN: LTM
ATTN: MXE
ATTN: MBC
ATTN: MXS

Air Force Rocket Propulsion Laboratory
ATTN: LKCP

Air Force Systems Command
ATTN: DLW

Air Force Weapons Laboratory
Air Force Systems Command
ATTN: SUL
ATTN: DYV

Arnold Engineering Development Center
Air Force Systems Command
ATTN: Library Documents

Foreign Technology Division
Air Force Systems Command
ATTN: SDBG

DEPARTMENT OF THE AIR FORCE (Continued)

Research, Development, & Acq.
Department of the Air Force
ATTN: AFRDQSM
ATTN: AFRDQ

Space & Missile Systems Organization
Air Force Systems Command
ATTN: DYS
ATTN: DYSE
ATTN: DYTE
ATTN: DYSR

Space & Missile Systems Organization
Air Force Systems Command
ATTN: MNNR
ATTN: MNNH

Strategic Air Command
Department of the Air Force
ATTN: XPFS
ATTN: XOBM

DEPARTMENT OF ENERGY CONTRACTORS

Lawrence Livermore Laboratory
ATTN: Document Control for L-10, H. Kruger
ATTN: Document Control for L-92, C. Taylor

Los Alamos Scientific Laboratory
ATTN: Document Control for J. Taylor

Sandia Laboratories
ATTN: Document Control for R. Clem
ATTN: Document Control for A. Chabai
ATTN: Document Control for D. Rigali

Sandia Laboratories
Livermore Laboratory
ATTN: Document Control for T. Gold

DEPARTMENT OF DEFENSE CONTRACTORS

Acurex Corp.
ATTN: J. Saperstein
ATTN: J. Huntington
ATTN: C. Powars
ATTN: C. Nardo
ATTN: J. Crenshaw

Aerojet Liquid Rocket Co.
ATTN: R. Jenkins

Aeronautical Rsch. Assoc. of Princeton, Inc.
ATTN: C. Donaldson

Aerospace Corp.
ATTN: P. Legendre
ATTN: R. Palmer
ATTN: W. Portenier
ATTN: M. Gyetvay
ATTN: H. Dyer
ATTN: D. Platus
ATTN: W. Grabowsky
ATTN: R. Mortensen
ATTN: D. Nowlan

ARO, Inc.
ATTN: G. Norfleet
ATTN: J. Adams

DEPARTMENT OF DEFENSE CONTRACTORS (Continued)

AVCO Research & Systems Group
ATTN: W. Broding

Boeing Co.
ATTN: B. Lempriere

Calspan Corp.
ATTN: M. Holden

Effects Technology, Inc.
ATTN: R. Wengler

Fiber Materials, Inc.
ATTN: M. Subilia

Ford Aerospace & Communications Corp.
ATTN: A. Denetriades

General Electric Co.
Re-Entry & Environmental Systems Div.
ATTN: P. Cline

General Electric Company—TEMPO
ATTN: DASIAC

General Research Corp.
ATTN: R. Rosenthal

Institute for Defense Analyses
ATTN: J. Bengston
ATTN: Classified Library

ION Physics Corp.
ATTN: R. Evans

Kaman Sciences Corp.
ATTN: F. Shelton
ATTN: J. Nickel
ATTN: V. Peckham

Lockheed Missiles & Space Co., Inc.
ATTN: C. Lee
ATTN: D. Price
ATTN: R. Au
ATTN: P. Schneider
ATTN: G. Chrusciel

Lockheed Missiles and Space Co., Inc.
2 cy ATTN: Y. Fortune

Martin Marietta Corp.
ATTN: R. Cramer

McDonnell Douglas Corp.
ATTN: G. Fitzgerald

National Academy of Sciences
National Materials Advisory Board
ATTN: D. Groves

Pacific-Sierra Research Corp.
ATTN: G. Lang

Physical Sciences, Inc.
ATTN: M. Finson

Prototype Development Associates, Inc.
ATTN: J. Dunn
3 cy ATTN: C. Thacker

DEPARTMENT OF DEFENSE CONTRACTORS (Continued)

R&D Associates

ATTN: F. Field
ATTN: R. Ross
ATTN: P. Rausch
ATTN: C. MacDonald

Science Applications, Inc.
ATTN: J. Warner

Science Applications, Inc.
ATTN: K. Kratsch
ATTN: L. Dunbar

Science Applications, Inc.
ATTN: A. Martellucci

Southern Research Institute
ATTN: C. Pears

DEPARTMENT OF DEFENSE CONTRACTORS (Continued)

Spectron Development Labs, Inc.
ATTN: T. Lee

SRI International
ATTN: D. Curran
ATTN: G. Abrahamson

TRW Defense & Space Sys. Group
ATTN: R. Myer
ATTN: D. Baer
ATTN: T. Alber
ATTN: T. Williams
ATTN: W. Wood

TRW Defense & Space Sys. Group
ATTN: E. Allen
ATTN: W. Polich
ATTN: E. Wong
ATTN: L. Berger
ATTN: V. Blankenship